Ab initio characterisation of spectroscopic properties of defects in silicon

Chloé Simha

Doctorat de l'Université de Toulouse

préparé à l'Université Toulouse III - Paul Sabatier

Ab initio characterisation of spectroscopic properties of defects in silicon

---

Thèse présentée et soutenue, le 27 mars 2024 par

Chloé SIMHA

École doctorale
GEETS - Génie Electrique Electronique,Télécommunications et Santé : du système au nanosystème

Spécialité
MicroNano Systèmes

Unité de recherche
LAAS - Laboratoire d'Analyse et d'Architecture des Systèmes

Thèse dirigée par
Anne HEMERYCK et Nicolas RICHARD

Composition du jury
M. Vincent GOIFFON, Président, ISAE-SUPAERO
M. Marco FANCIULLI, Rapporteur, Università degli Studi di Milano
M. Davide CERESOLI, Rapporteur, National Research Council of Italy
Mme Anaïs DREAU, Examinatrice, Université de Montpellier
M. Stefano DE GIRONCOLI, Examinateur, SISSA - Scuola Internazionale Superiore di Studi Avanzati
Mme Gabriela HERRERO-SABOYA, Examinatrice, SISSA - Scuola Internazionale Superiore di Studi Avanzati
Mme Anne HEMERYCK, Directrice de thèse, CNRS Occitanie Ouest
M. Nicolas RICHARD, Co-directeur de thèse, CEA DAM-île de France

Membres invités
M. Luigi GIACOMAZZI, Co-encadrant, CNR-IOM, SISSA - Scuola Internazionale Superiore di Studi Avanzati

Acknowledgements

The last 3.5 years have surely been the most enriching I have ever gone through, on a scientific and professional level but also for my social and personal growth. Between supercomputer issues, doubts and long nights there have been captivating discoveries, enriching trips leading to encounters with fascinating people. I would therefore like to acknowledge some of those who were essential in the achievement of this work.

First, I would like to thank the jury of my defence, Pr Vincent Goiffon, Pr Marco Fanciulli, Dr Davide Ceresoli, Dr Anaïs Dréau and Pr Stefano De Gironcoli, for taking the time to read this manuscript, and for attending the defence and asking stimulating questions.

I certainly didn't say it enough during my thesis, but I could not have asked for a better team of supervisors and collaborators who, despite the never-ending amount of tasks of a researcher, always made themselves available to guide, advise and/or help when asked.

To my supervisors, Anne and Nicolas, thank you for being supportive and kind, for always knowing how to deal properly with the administrative parts of a thesis so that I could fully focus on research, and for ensuring that breakthroughs are celebrated and issues dealt with.

To my co-supervisors Layla and Luigi, you have taught me so much, about physics of course and about being a researcher, I am grateful to you both for reminding me how to be curious.

I want to give a special mention to Gabriela. Thank you for undertaking the (unofficial) roles of co-supervisor and mentor, even though freshly out of your own thesis. Thank you for your energy, patience and guidance at every step of the way.

I also thank all colleagues from CEA, LAAS and SISSA with whom I had the pleasure of sharing breaks (and crosswords), outings as well as fruitful conversations about science, (a lot of) soccer and rugby, baking, spelunking, and life in general which made me look forward to every day and every visit. I especially want to acknowledge those who made me feel among friends rather than co-workers. From CEA, Jeoffray, Julien Lomonaco, Julien Parize, Lucie, Nicolas Richard, Thomas, Damien, Margot, Jean-Luc, Claude, Dudu. From LAAS, Anne, An-

toine, Pierre-Louis, Cesar, Juan. And from SISSA, Gabriela, Layla, Luigi, Matic, Nicolas Salles.

I certainly couldn't have achieved this work without the support and encouragements from family and friends. In particular to my parents, sister and grand-parents, thank you for sincerely trying to understand the subject of this thesis. To my friends, Soa, Aymeric, Sarah, Fabiola, Melha, Onésia and Maryam, thank you for not giving up on me even though I was not very present lately.

Finally (dare I say most importantly?), it could be doubted that I wrote this manuscript if it didn't contain a mention of my dog, Lully, who reminds daily to also enjoy the simple things in life.

Abstract

Silicon has been a cornerstone of modern semiconductor technology for the last seven decades. However, the optimisation of silicon-based devices hinges on a deep understanding of the defects that can be introduced into its structure, which can significantly influence device performance and reliability. Although extensive research has been conducted on point defects in silicon, certain aspects are still not fully understood or have not yet been resolved. Therefore, characterising defects in silicon is a critical imperative for advancing semiconductor physics, ensuring device reliability, and driving innovation in electronic applications. Multiple characterisation techniques have been developed to unravel defect specific properties. In particular, Deep Level Transient Spectroscopy which allows obtaining information on the electrical behaviour of defects and more specifically the number and nature of deep levels within the gap of the sample containing them, and Electron Paramagnetic Resonance spectroscopy (EPR) which provides information on the atomic and electronic structures of the defect and its environment are invaluable in identifying defects and evaluating their impact on the properties of the material. Yet, identifying specific defect structures through spectroscopic means is often non-trivial and requires to combine several techniques to obtain a complete picture of the system. In the last two decades, the identification effort has been more and more supported by theoretical methods, such as *ab initio* calculations based on Density Functional Theory (DFT), that play a complementary and crucial role in improving the understanding of the physics of the defect.

This thesis presents models of ground state structures for several defects in silicon. Unlike many prior atomistic simulations that determine the ground state from numerical results, this study defines the structure through symmetry considerations, *i.e.* grounded in molecular orbital approaches and group theory. This approach enhances the reliability of the model and is not limited by the numerical accuracy of DFT calculations. The fundamental physical properties of the defect, such as its energy landscape or electronic structure, are established by DFT calculations. Moreover, by including more refined approaches, based on perturbation theory and many-body corrections, EPR parameters and thermodynamic charge transition levels are calculated in order to provide direct comparison with spectroscopy experiments. The reliability and accuracy of this methodology is first validated on a well-known system, the phosphorus-vacancy complex, the so-called silicon E-center and very good agreement is obtained with experiments and previous theoretical methods for EPR parameters. This method is then applied to various nitrogen-related defects in silicon, which are not as well understood. The computed spectroscopic parameters thus allow obtaining an unequivocal correspondence between available experimental signals and defect structures, as well as providing reference values to guide experimenters in cases when data are not available.

Résumé

Le silicium a joué un rôle fondamental dans la technologie moderne des semi-conducteurs au cours des sept dernières décennies. Cependant, l'optimisation des dispositifs basés sur le silicium dépend d'une compréhension approfondie des défauts qui peuvent être introduits dans sa structure, ce qui a un impact significatif sur les performances et la fiabilité de ces dispositifs. Bien que des recherches approfondies aient été menées sur les défauts ponctuels du silicium, certains aspects demeurent encore incompris ou non résolus. Ainsi, la caractérisation des défauts dans le silicium est cruciale pour faire progresser la physique des semi-conducteurs, garantir la fiabilité des dispositifs et stimuler l'innovation dans les applications électroniques. Plusieurs techniques de caractérisation ont été développées pour élucider les propriétés spécifiques des défauts. Notamment, la spectroscopie des niveaux profonds, qui fournit des informations sur le comportement électrique des défauts, comme le nombre et la nature des niveaux profonds au sein de l'échantillon, et la spectroscopie de Résonance Paramagnétique Électronique (RPE), qui offre des informations sur les structures atomiques et électroniques du défaut et de son environnement, sont des outils précieux pour identifier les défauts et évaluer leur impact sur les propriétés du matériau. Cependant, l'identification de structures de défaut spécifiques par des moyens spectroscopiques est souvent complexe et nécessite la combinaison de plusieurs techniques pour obtenir une image complète du défaut. Ces vingt dernières années, les efforts d'identification ont été de plus en plus soutenus par des méthodes théoriques, telles que les calculs *ab initio* basés sur la Théorie de la Fonctionnelle de la Densité (DFT), qui jouent un rôle complémentaire et crucial pour améliorer la compréhension de la physique du défaut.

Cette thèse présente des modèles de structures à l'état fondamental pour plusieurs défauts dans le silicium. Contrairement à de nombreuses simulations atomistiques antérieures qui déterminent l'état fondamental à partir de résultats numériques, cette étude définit la structure à travers des considérations de symétrie, en s'appuyant sur des approches d'orbitales moléculaires et de théorie des groupes. Cette approche renforce la fiabilité du modèle et n'est pas limitée par la précision numérique des calculs DFT. Les propriétés physiques fondamentales du défaut, telles que son paysage énergétique ou sa structure électronique, sont alors établies par des calculs DFT. De plus, en incluant des approches plus raffinées basées sur la théorie des perturbations et les corrections à plusieurs corps, les paramètres RPE et les niveaux de transition de charge thermodynamiques sont calculés pour permettre une comparaison directe avec les données expérimentales. La fiabilité et la précision de cette méthodologie sont d'abord validées sur un système bien connu, le complexe phosphore-vacance, aussi connu sous le nom de centre E du silicium, montrant une excellente concordance avec les expériences et les méthodes théoriques précédentes pour les paramètres RPE. Ensuite, cette méthode est appliquée à divers défauts liés à l'azote dans le silicium, qui sont moins bien compris. Les paramètres spectroscopiques calculés permettent ainsi d'établir une correspondance sans équivoque entre les signaux expérimentaux disponibles et les structures de défaut, tout en fournissant des valeurs de référence pour guider les expérimentateurs dans les cas où les données ne sont pas disponibles.

Contents

List of Abbreviations

BFGS Broyden–Fletcher–Goldfarb–Shanno.

BZ Brillouin Zone.

CB Conduction Band.

CBM Conduction Band Minimum.

CTLs Charge Transition Levels.

CW Continuous Wave.

DFT Density Functional Theory.

DLTS Deep Level Transient Spectroscopy.

DOS Density Of States.

EA Electronic Affinity.

ENDOR Electron Nuclear Double Resonance.

EPR Electron Paramagnetic Resonance.

GGA Generalized Gradient Approximation.

GIPAW Gauge–Including Projector Augmented Wave.

HF Hartree–Fock.

hfi Hyperfine.

HK Hohenberg–Kohn.

HOMO Highest Occupied Molecular Orbital.

HSE Heyd-–Scuseria—Ernzerhof.

IP Ionisation Potential.

JT Jahn–Teller.

KS Kohn–Sham.

LDA Local-Density Approximation.

LUMO Lowest Unoccupied Molecular Orbital.

MEP Minimum Energy Path.

MP Monkhorst–Pack.

MW MicroWave.

NEB Nudged Elastic Band.

PAW Projector Augmented Wave.

PBC Periodic Boundary Conditions.

PBE Perdew–Burke–Ernzehorf.

PES Potential Energy Surface.

pJT pseudo Jahn–Teller.

PP PseudoPotential.

pw Plane Waves.

QE Quantum Espresso.

QP Quasi–Particle.

SB Symmetry–Breaking.

SC SuperCell.

SCF Self Consistent Field.

SCR Space Charge Region.

SD Slater Determinant.

SI Self–Interaction.

tw This Work.

VB Valence Band.

VBM Valence Band Maximum.

XC eXchange–Correlation.

Introduction

In today's technological landscape, semiconductors are fundamental components that drive an extensive array of devices, from essential everyday-life tools to advanced specific systems and beyond. Among the variety of semiconductors in the industry, silicon holds a central position, powering the electronic devices that have become indispensable in our modern society. As the demand for more efficient and reliable devices grows, attention turns to the defects within the silicon lattice. Defects have a deep influence on material properties, and thus device performance and reliability.

These defects can be introduced within the material through various mechanisms (Fig. 1a). They may arise unintentionally, *e.g.* in space environments where the microelectronic components within satellite embedded systems are exposed to energetic particles. In such case, the radiation may impact devices and induce defects that compromise their performance. On the other hand, defects can also be introduced during semiconductor manufacturing processes, *e.g.* either by the intentional doping of the material or by the accidental introduction of impurities from the environment. Incorporating impurities into the lattice allows to tune material properties to specific needs and applications and therefore to enhance its efficiency. The characterisation and understanding of these defects are therefore a critical imperative for advancing semiconductor technology and ensuring the development of more robust and efficient electronic devices. By delving deeper into the fundamental properties (*i.e.* nature, behaviour, and impacts) of these defects, it becomes possible to devise strategies to mitigate their detrimental effects or harness their potential benefits.

Multiple experimental characterisation techniques have been developed in order to identify defects, unravel specific properties and evaluate their impact on the properties of the material. The first notable method, Deep Level Transient Spectroscopy (DLTS), offers insights into the electrical behaviour of defects. More specifically, from a DLTS spectrum, the position and nature (e.g., donor or acceptor) of deep levels in the gap can be inferred. Another significant technique is Electron Paramagnetic Resonance spectroscopy (EPR) which provides information on the specific structures of the defect. In particular, the immediate environment of paramagnetic (or unpaired) electrons can be determined, allowing for a comprehensive characterisation of the defect's precise atomic structure and its corresponding electronic configuration. How-

ever, identifying specific defect structures through spectroscopic means is often non-trivial and requires to combine several techniques, which each have their own drawbacks and limitations. In particular, EPR does not provide information on non-paramagnetic defects (*i.e.* neutral precursors) nor provides a direct access to the position of defect levels within the band gap. On the other hand, DLTS provides information on defect levels, but is unable to provide information on the electronic structure of defects. In other words, it is possible to infer that the levels relate to an impurity such as nitrogen for example, but knowing which structure precisely is responsible for the levels is unfeasible.

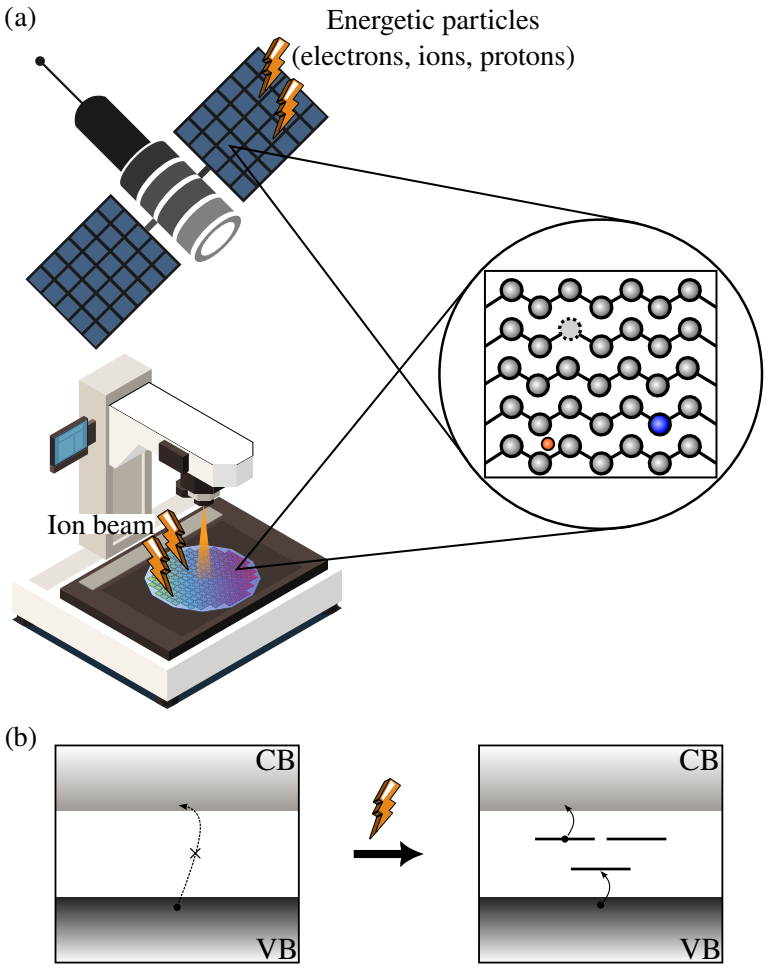

Fig. 1: (a) Various illustrations of cases of "defects" within the material caused by irradiation or implantation processes. Defects include vacancies (dotted circle), substitutional impurities (or dopants) (blue circle), interstitial impurities (orange circle), and complexes combining these elements. (b) In a pristine semiconducting material, electrons (black dot) cannot cross the band gap without a strong excitation source. Defects introduce traps within the band gap of the material, enabling the transition of electrons from the valence band (VB) to the conduction band (CB), even at RT.

Furthermore, theoretical approaches, such as *ab initio* calculations based on Density Func-

tional Theory (DFT), play a complementary and crucial role in improving the understanding of the physics of defects. DFT is a powerful method that has become essential in characterising defects as it provides insight ranging from atomic and electronic configurations to defect formation mechanics and relative stability. Nonetheless, estimations based on DFT computations have typically focused on individual properties associated with specific families of defects, rather than providing a comprehensive overview of the overall behaviour of the system. Until the last decade, due to limitations in computational resources, theoretical results also relied on indirect evidence of defect features only, *e.g.* the defect electronic structure, necessitating some extrapolation to align with experimental observations.

It is only recently that advanced theories have been developed, enabling accurate computation of spectroscopic properties. These methods therefore allow direct comparison with experiments such as EPR spectroscopy and DLTS. The adequation between computational results and experimental observations validates the established defect model, which in turn allows to gain insight into properties that are not easily obtained by experimental methods alone.

Given this perspective, this thesis aims to provide models of ground state structures for several defects in silicon. Unlike many prior atomistic simulations that determine the ground state from numerical results, this study defines the structure through symmetry considerations, *i.e.* grounded in molecular orbital approaches and group theory. This approach enhances the reliability of the model and is not limited by the numerical accuracy of DFT calculations. The defect fundamental physical properties, such as its energy landscape or electronic structure, are established by DFT calculations. Moreover, by including more refined approaches, based on many-body perturbation theory, EPR parameters and thermodynamic Charge Transition Levels (CTLs) are calculated in order to provide direct comparison with spectral fingerprints. The reliability and accuracy of this methodology are first validated on a well-known system, the phosphorus-vacancy complex, the so-called silicon E-center, achieving excellent agreement with experiments and previous theoretical methods for EPR parameters. This method is subsequently applied to examine nitrogen-related defects in silicon, for which several signals have yet to be attributed to specific defects. In particular, the focus is directed towards two systems, the substitutional impurity N_{Si} and the impurity-vacancy pair NV, whose spectral fingerprints are not fully identified. The computed spectroscopic parameters thus allow to obtain an unequivocal correspondence between available experimental signals and defect structures, as well as provide reference values to guide experimenters in cases of lack of experimental data.

The first chapter of this thesis delves into fundamental concepts related to defects in semiconductors, with a particular emphasis on silicon. The chapter provides details on conventional techniques for introducing defects into the material lattice via crystal doping, with particular focus on doping processes that result in nitrogen-related defects. The physical principle of characterisation methods commonly employed to identify these defects are also described, specifically highlighting EPR spectroscopy and DLTS. Parameters derived from measurements, such as the g-tensor and hyperfine coupling tensor for EPR, and deep levels for DLTS, are discussed. These techniques allow the identification of peculiar symmetries of defect systems, phenomena that can be rationalized by thinking in terms of Jahn-Teller effects, which explain the spontaneous symmetry breaking in defect ground states. The main characteristics of these

effects, *i.e.* the Jahn-Teller and pseudo-Jahn-Teller effects, are also detailed.

Chapter 2 provides a brief review of the methodological approaches used in this thesis to perform *ab initio* calculations based on DFT. The specific methods employed to compute spectroscopic properties, such as EPR parameters through the Gauge-Including Projector Augmented Waves (GIPAW) method and CTLs through simple DFT calculations and the GW approximation, are detailed as well.

Chapter 3 presents a validation of the accuracy of the different methods discussed on a well-known system, the silicon *E*-center. The optimal combination of computational parameters is determined in order to obtain the most accurate results.

Comprehensive models for the ground state properties for N_{Si} and NV are provided in chapters 4 and 5 respectively, based on simple symmetry considerations and *ab initio* calculations. In particular, through an understanding of the symmetry-breaking mechanisms in these systems, their fundamental physical properties (*e.g.* electronic structure, energy landscape) are elucidated. Moreover, more refined methods are employed to compute EPR parameters and thermodynamic CTLs in order to establish direct comparison with experimental data. For both systems studied rather little information is actually known. EPR spectroscopy investigations, with the pioneering works by K.L. Brower dating back to the early 1980s, assigned the so-called SL5 signal to the presence of N_{Si}. On the other hand, little to no experimental evidence of NV is available. Therefore, an unequivocal correspondence between EPR recorded spectrum and computed parameters is established for N_{Si}. Furthermore, for both systems, reference values of deep levels within the band gap are presented, to guide experimenters in the identification of the systems in future works.

Finally, conclusions on the findings of this thesis regarding the characterisation of N-related defects in silicon and perspectives on the limitations of this method, as well as the possible pursuit of this work are presented.

Chapter 1

Introduction to defects in silicon

This PhD thesis presents a theoretical investigation of point defects encountered in nitrogen-doped silicon. This chapter provides an introduction to the formation, fundamental properties and identification of defects in semiconductors. Following a brief definition of crystal point defects, a discussion on defect formation in silicon, and in particular impurity doping techniques is provided in Section 1.1. Experimental techniques usually performed to identify and characterise defect structures and properties are then described in Section 1.2. The description focuses on Electron Paramagnetic Resonance (EPR) and Deep Level Transient Spectroscopy (DLTS), both valuable as direct comparisons can be carried out with properties derived from numerical methods. Finally, Section 1.3 focuses on the Jahn-Teller (JT) and pseudo-Jahn-Teller (pJT) effects as frameworks to understand and simplify the identification of structural and fundamental physical properties of defects.

1.1 Point defects in crystalline silicon

This section deals with the most fundamental aspect addressed in this thesis, *i.e.* the formation of point defects within a crystalline material such as silicon. The preliminary ideas on this subject are defined, as well as specific notions regarding the designation of defects systems through their symmetry. Usual methods employed to dope silicon are described, and particularly cases leading to nitrogen-related defects.

1.1.1 Preliminary definitions

1.1.1.1 Point defects

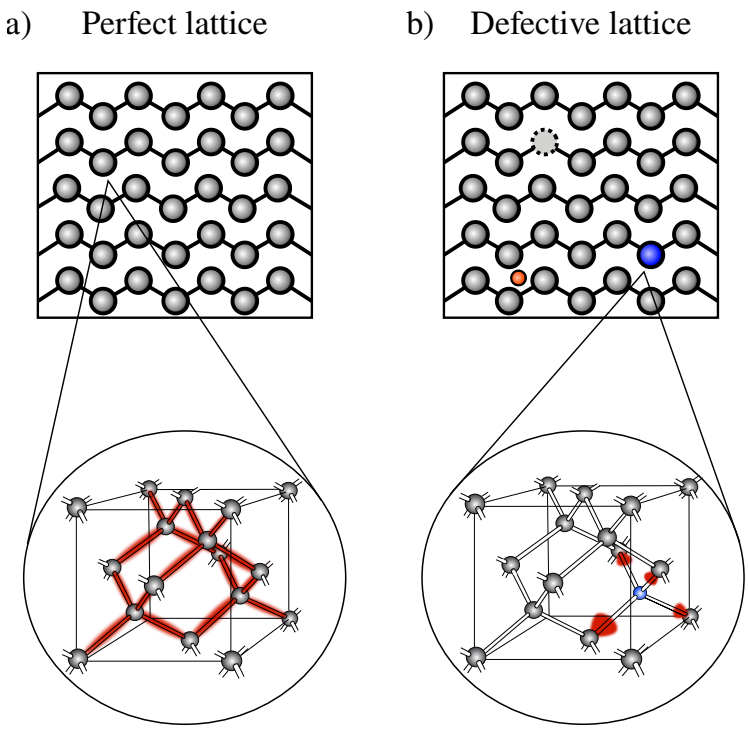

Fig. 1.1: Schematic representation of the atomic (top) and electronic (bottom) structures for a (a) Pristine and (b) Defective crystal lattice. Defects include vacancies (dotted circle), substitutional impurities (blue circle), interstitial impurities (orange circle), and complexes combining these elements. The electronic density corresponding to the bulk wavefunction and the defect-induced states is represented in red.

A crystal, such as silicon, is a solid material characterised by a periodic arrangement of its constituents, *e.g.* atoms, in a three-dimensional lattice structure [1]. In a perfect crystal the atomic arrangement is highly ordered and exhibits translational symmetry in all directions, giving rise to uniform physical and chemical properties across the material. Therefore, a point defect in a crystalline material can be defined as a local irregularity within the material lattice,

which disrupts its periodicity [2]. These defects may involve missing (vacancy) or additional (interstitial) atoms, atomic substitutions (substitutionals), or complexes combining these elements (*e.g.* di-interstitials, impurity-vacancy complexes...), as illustrated in Fig. 1.1b. They are called *point* defects due to the local nature of the disturbance within the lattice periodicity, that is the impact on the structure is only on the closest neighbours of the defect site, as opposed to larger defect structures, including dislocations or voids.

Nevertheless, their effect on the properties of the material is not necessarily as limited. In particular, the resulting perturbation of the electronic structure can be rather delocalised. In that respect, defects can introduce electronic energy states within the semiconductor bandgap, which can be classified in two categories, shallow and deep levels (Fig. 1.2). A shallow level is caused by a small perturbation of the lattice, *e.g.* an impurity, which can either capture an electron from the valence band or release an electron to the conduction band. This system is then referred to as a shallow acceptor or donor respectively, and the electron is not very strongly bound to the defect state. This type of system is therefore characterised by a rather extended electronic density. On the other hand, a deep level or trap, generally generated from a more complex defect structure, can both bind and emit an electron. The disturbance to the pristine material is therefore larger as the wavefunction of the trapped electron is much more localised on the defect center and immediate neighbouring atoms. Therefore, deep defects induce the rearrangement of atoms surrounding the defect center to attain thermodynamic stability. This atomic displacement can be a simple *relaxation* when the overall symmetry of the lattice is preserved, or a *distortion* when its symmetry is modified. Even so, more often than not, for isolated defects the induced electronic states are easily distinguishable from the material bulk states as the former are spread only over a few atoms surrounding the defect (Fig. 1.1b), whereas the latter are, by definition, evenly delocalised over the entire material (Fig. 1.1a).

It is interesting to note that shallow defects levels are usually assigned to being close to the relevant bands, and deep levels near the middle of the gap, as depicted in Fig. 1.2. However, this definition is considered too simplistic and vague as defects introducing highly localised states can be found somewhat close to band edges, particularly considering small gap semiconductors like silicon (1.1 eV at room temperature [3]) where even a level near mid-gap is still not so far from valence and conduction bands.

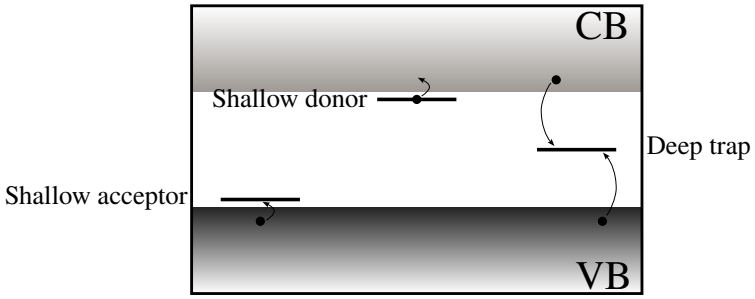

Fig. 1.2: One-electron energy scheme for semiconductors, depicting the position of shallow donor and acceptor levels as well as deep levels within the band gap.

1.1.1.2 Defect symmetry

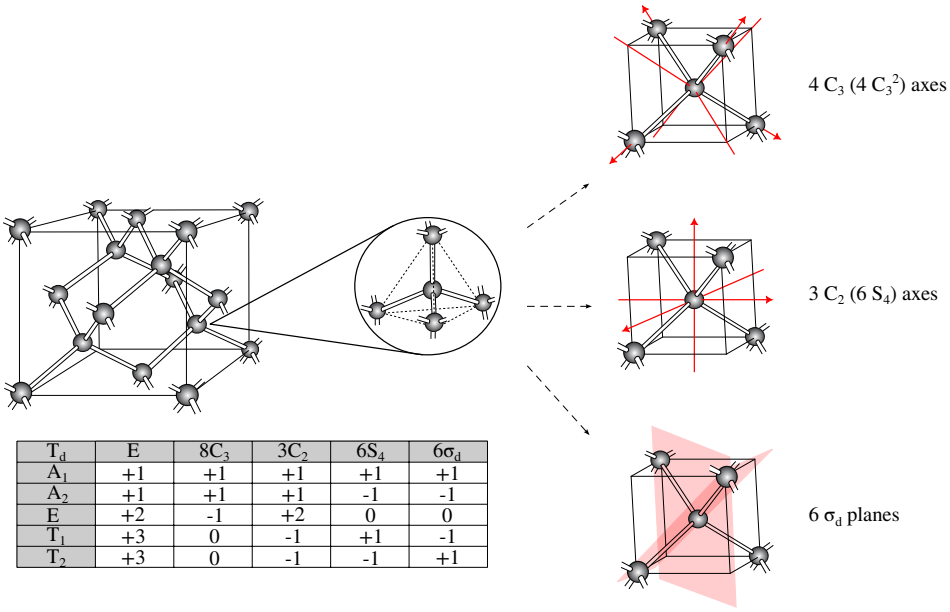

T_d	E	$8C_3$	$3C_2$	$6S_4$	$6\sigma_d$
A_1	+1	+1	+1	+1	+1
A_2	+1	+1	+1	-1	-1
E	+2	-1	+2	0	0
T_1	+3	0	-1	+1	-1
T_2	+3	0	-1	-1	+1

Fig. 1.3: Different symmetry operations for the T_d point group are represented (in red) on a schematic configuration typical in the diamond crystal structure. Each column of the corresponding character table records these symmetry elements (C_3, C_2, S_4 axes, σd planes, as well as identity E). Each row of the table is an irreducible representation and the entries, or characters, in the table identify the behaviour of the structure with respect to the symmetry operation. In particular, a character +1 signifies that the system remains unchanged with the operation, whereas a character –1 indicates that it becomes reversed. Similarly, the denomination of the irreducible representation specifies the symmetry, *i.e.* A representations are symmetric with respect to the principal rotation axis, and E and T are doubly and triply degenerate respectively.

As seen above, the lattice symmetry of the material is broken by the introduction of defects. Nevertheless, the structure of the defect itself generally exhibits specific geometry, which arises from the balance between electronic effects, *i.e.* electron-electron repulsions, and steric effects, *i.e.* nuclear-nuclear repulsions among atoms attached to the defect center [4]. The description of the corresponding symmetry properties, through group theory, therefore allows to build a model of the defect structure in order to understand and predict its physical and chemical characteristics.

These symmetry properties are identified as specific operations that can be applied to the defect structure without altering its appearance or properties, *i.e.* after a symmetry operation, each atom within the system is substituted with a corresponding equivalent atom. There exist five types of operations to be applied on any given structure. The identity (E) corresponds to no change performed on the system, thus all systems have at least this operation. The proper rotation (C_n) refers to a rotation of the system around a symmetry axis by $\frac{2\pi}{n}$ rad resulting in an indistinguishable structure, where n denotes the number of equivalent rotations. The reflection (σ) occurs with respect to a symmetry or mirror plane. The inversion (i) corresponds

to a reflection with respect to a point of symmetry, rather than a plane. Finally, the improper rotation (S_n) combines a proper rotation around an axis C_n and a reflection with respect to a plane perpendicular to the rotation axis.

A set of operations describing a given system form a *point group* which defines the symmetry operations within the system resulting in configurations identical to the initial one (Fig. 1.3). The character table serves as a tabular representation that systematically organises the symmetry operations belonging to a specific point group. It describes how a given system behaves under these operations, providing essential information about the transformation properties of the various components of the system, such as atomic orbitals. The entries in the character table, referred to as characters, convey how each irreducible representation of the point group transforms under the symmetry operations. Each irreducible representation corresponds to a *unique* behaviour under the symmetry operations and are labelled to indicate the specific symmetry of the representation.

1.1.2 Introducing defects within the silicon lattice

Understanding not only the defect structure and symmetry, but also how they are introduced in the crystal lattice is required to recognise which combinations of defects are likely present within a given sample and thus likely to affect device properties. In the case of silicon which is the focus of this work, there are two main ways for defects to be added to the material lattice (as mentioned in the introduction). In the first one, defects can be introduced unintentionally by energetic particles irradiation. However the second mechanism, more relevant to the defects studied in the following chapters of this thesis, is that of the intentional impurity doping of the material during manufacturing processes. Knowing the methods to implant various impurities within the silicon lattice therefore allows to obtain a general idea of the defects that can be formed, which may either hinder or enhance material characteristics. The standard doping of silicon, resulting in n- or p-type semiconductors is first detailed, including which impurities are commonly employed. Furthermore, a particular focus on the case of nitrogen-doping in silicon is highlighted for its relevance in introducing N-related defects. The methods commonly employed to effectively form the defects impacting device properties, *i.e.* ion implantation and diffusion, are then described.

1.1.2.1 Impurity doping: n-/p-type silicon

The doping process is a key aspect of semiconductor technology and is used to modify the electrical properties of silicon, making it more suitable for various electronic applications. The intentional introduction of specific types of dopant atoms into the silicon crystal lattice results in n-type and p-type materials [5]. In n-type silicon, the semiconductor is doped with species that have more electrons in their valence shell than silicon. Common donor dopants typically include group-V atoms. The excessive electron requires much less energy to jump from the valence band (VB) to the conduction band (CB) than the electrons which cause the intrinsic conductivity of silicon (case of the shallow donor in Fig. 1.2). The free electron thus becomes a mobile charge carrier, contributing to the semiconductor's conductivity. The presence of

additional electrons makes n-type silicon an electron-dominated material, *i.e.* the majority charge carriers are electrons, and the minority carriers are holes. On the other hand, p-type silicon is doped with trivalent atoms (belonging in group-III). The acceptor dopants can capture an additional outer electron, as the energy necessary to lift the electron from the VB to the dopant generated defect level is much lower than to the CB (case of the shallow acceptor in Fig. 1.2). This exchange thus leaves a hole in the VB and the remaining electrons within the band become mobile. In a manner analogous to n-doped semiconductors, here, the holes are the majority charge carriers and free electrons are the minority charge carriers. The choice of dopant depends on the specific application and the desired properties of the doped silicon. Furthermore, some elements are favoured because their atomic sizes closely match that of silicon, and they exhibit high solubility within the material. In particular, n-type dopants include phosphorus and arsenic, whereas boron and gallium are commonly used for p-type doping. Nitrogen doping in silicon, on the other hand, is employed to enhance the mechanical strength [6,7], augment the precipitation of oxygen [8], suppress the diffusion of self-interstitials [8], anchor dislocations [9] and restrain the formation of voids [10].

Combining both n-type and p-type semiconductors creates a p-n junction, the fundamental elementary unit necessary to the fabrication of various electronic components such as diodes, transistors and integrated circuits. This device exhibits striking and essential electronic behaviour, and allow for the controlled flow of electrical current, which is critical to components function.

1.1.2.2 Ion implantation and diffusion

In many semiconductor fabrication processes, a combination of methods is commonly employed for doping [11]. The first technique, ion implantation, consists in introducing ionised and accelerated dopant ions directly into the the material substrate. The high-energy atoms penetrate the crystal lattice, causing structural damage by displacing silicon atoms from their original equilibrium positions, through physical (and not chemical) interactions. Finally, when the impurity ions loose their energy through collisions with atoms and electrons in the lattice, they stop at an equilibrium position at a given distance from the surface of the sample. The implanted species typically reach depths of 10 nm – 10 μm within the material depending on the acceleration energy of the ion beam, ranging from 1 keV to 1 MeV. The ion dose (*i.e.* the density of implanted ions per square centimeter of the semiconductor surface area) is also an important parameter in determining the length of the path followed by the dopants and their concentration in the lattice, and usually ranges from 10^{11} to 10^{18} ion/cm^2. The main advantages of this method are that it enables precise doping in specific regions of the semiconductor substrate, with mostly vertical (and little lateral) diffusion of the dopants. It also allows for highly accurate control over dopant concentration and penetration depth. Finally, this technique provides good reproducibility and perform under lower temperatures than other doping mechanisms.

On the other hand, the implantation process introduces structural damage to the semiconductor lattice as the high-energy ions collide with host atoms. Subsequent annealing steps are therefore often performed to repair the lattice damage. This process also corresponds to the second possible method to dope semiconductors, *i.e.* thermal diffusion. The annealing of the

implanted sample occurs at high temperatures, allowing the healing of the damaged silicon lattice and also to further spread the impurities within the lattice. In this case, the atoms move both vertically and laterally, as a result of concentration gradients (*i.e.* dopants migrate from regions of higher concentration to regions of lower concentration). The driving force for this mechanism is the interaction of the impurity with intrinsic defects in the crystal lattice (vacancies, interstitials) which may recombine with the dopant and allow for its movement.

Understanding the intricacies of dopant diffusion in silicon is paramount for understanding the complex interplay between dopants and intrinsic defects and impurities within the semiconductor material. The comprehension of dopant diffusion provides insights into the potential interactions and recombination processes involving intrinsic defects and impurities. This information is invaluable for defect engineering, enabling intentional modification of defect properties to optimize semiconductor performance. The diffusion process plays a pivotal role in shaping the concentration and distribution of dopants and defects, directly impacting electrical conductivity, carrier mobility, and overall semiconductor properties. Moreover, this understanding is instrumental in ensuring the reliability, stability, and long-term performance of semiconductor devices. By correlating dopant diffusion with changes in semiconductor properties, it becomes possible to identify and characterise specific defects, allowing to improve semiconductor manufacturing processes and enhance device performance across diverse applications.

1.2 Experimental characterisation of defects in silicon

Intrinsic defects (*e.g.* vacancies), formed during crystal growth or processing, interact easily with common residual impurities (*e.g.* oxygen, carbon) and dopants. These complexes are sometimes electrically active with deep states within the bandgap and need to be characterised in order to assess their effect on device performance. These complexes are therefore characterised using various analytical techniques which provide valuable information about the nature and concentration of defects in the material. Such methods include Deep Level Transient Spectroscopy (DLTS) and Electron Paramagnetic Resonance (EPR) that allow to unravel specific defect properties. The general principle of each technique as well as the relevant parameters that allow to characterise semiconductor samples are detailed below.

1.2.1 Deep levels within the bandgap: Deep Level Transient Spectroscopy

1.2.1.1 General principle

Deep Level Transient Spectroscopy (DLTS) is a sophisticated technique employed in semiconductor physics to probe and characterise deep-level defects within materials [12, 13]. The fundamental principle of DLTS involves the controlled introduction of excess charge carriers, *i.e.* holes or electrons, into a sample, typically through methods such as optical excitation, electrical biasing, or temperature changes. These excess carriers become temporarily trapped

by deep-level defects present within the lattice. Subsequently, DLTS monitors the transient behaviour of these carriers as they are released from the defects back into the semiconductor band structure. Through capacitance measurements and the analysis of DLTS spectra, it is possible to gain valuable insights into the electronic activity of the defect, *i.e.* the number and nature of energy levels as well as defect concentration and capture cross-section. This information is instrumental for understanding the electronic properties of the semiconductor, identifying defects, and optimising the performance of devices. DLTS probes defects within the depletion region formed in a p-n junction, or Schottky diode. Defects within this depletion region are more easily detectable in comparison to those in bulk materials due to the rarity of free charge carriers in the depletion region. The minimal presence of free carriers enables the detection of even slight variations in carrier density within the depletion region. In contrast, monitoring the same change in carrier density in bulk materials is challenging, given the abundance of free carriers present.

A capacitance transient can be induced from a polarisation cycle, which can be decomposed in three distinct steps (Fig. 1.4a). First, a reverse bias is applied to the sample, under which the depletion region, or space-charge region (SCR) exhibits minimal free carrier concentration, causing the traps in this zone to be empty. Subsequently, under a forward bias the width of the SCR decreases, delimiting a region in which all traps are considered filled during a sufficiently long time. Finally, the initial reverse bias is restored, prompting a return to the equilibrium state of the filled traps within the SCR. This re-emission of captured carriers thus generates a capacitance transient.

DLTS encompasses various techniques for investigating deep-level defects in semiconductors. In addition to conventional DLTS, Minority-Carrier DLTS shifts the focus to minority carriers (*e.g.* electrons in a p-type material or holes in an n-type material). By specifically targeting minority carriers, this variant of DLTS offers a unique perspective on defects associated with these carriers, enhancing sensitivity to minority carrier-related defects. On the other hand, Laplace-DLTS extends the conventional DLTS methodology by employing Laplace transform techniques for enhanced signal analysis. This technique proves advantageous in resolving closely spaced defect levels and extracting additional details about defect dynamics. This allows to explore the temporal aspects of defects and gain insights into how their behaviour evolves over time.

1.2.1.2 Deep levels characteristics

In DLTS, the capacitance transient as a function of temperature (typically between 80 and 400 K), exhibits distinct peaks, each of which is associated with a trap level (Fig. 1.4b) [14]. The appearance of these peaks is distinctly determined by the thermal emission properties of specific defects and is proportional to the defect density. Consequently, these peaks serve as distinctive signatures that facilitate the identification of defects.

The parameters essential for characterising defects through DLTS are extracted from spectra by analyzing key features. Notably, the determination of peak energies is crucial for identifying the activation energy associated with the capture (or release) of the charge carriers by the trap, and each peak corresponds to a defect level. The analysis of the amplitude of the peaks then provides information about the concentration and capture cross-section of deep-level defects.

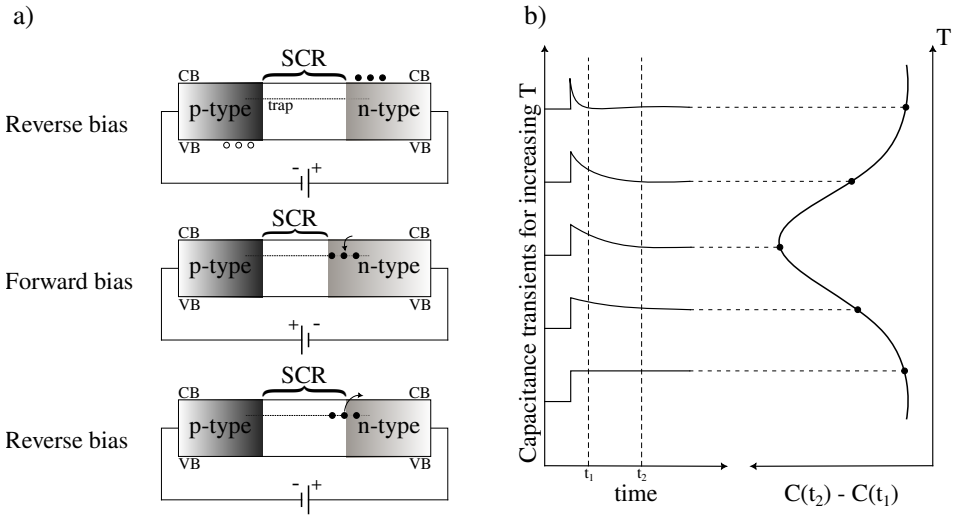

Fig. 1.4: (a) Schematic representation of the generation of a capacitance transient. (b) Typical DLTS peak which corresponds to the average difference of the current transients C(t) sampled at times t_1 and t_2 for various temperatures.

Examining the amplitudes associated with different energy levels allows to characterise the efficiency with which defects capture (or release) carriers and to quantify the density of defects within the semiconductor material. The width of the peaks yields information about the thermal emission rate of carriers from deep-level defects, reflecting the dynamics of carrier emission. Finally, the nature of the level (*e.g.* donor or acceptor) is obtained through the examination of the direction of the signal. A donor-like defect is reflected in a positive peak (assigned to majority carriers), indicating an increase in capacitance and an association with an excess of electrons. On the other hand, an acceptor-like defect results in a negative peak (assigned to minority carriers), signifying a decrease in capacitance and an association with an excess of holes.

More specifically, in the case of n-doped silicon, electrically active defects are characterised by their emission rate e_n, energy level E_t, and concentration N_t. These parameters form the electrical signature of defects within the framework of the Shockley-Read-Hall theory [15] which involves determining the electron emission rate as

$$e_n = \gamma_n \sigma_n T^2 e^{-\frac{(E_c - E_t)}{k_B T}} \tag{1.1}$$

where γ_n is a set of constants, σ_n the capture cross section of the trap, T the temperature, E_c the effective density of state in the conduction band and k_B the Boltzmann constant. In this regard, $E_c - E_t$ thus corresponds to the depth of the trap level within the bandgap with respect to the conduction band edge, *i.e.* the activation energy E_A. Thus the emission rate is directly proportional to $e^{(-\frac{1}{T})}$ and the DLTS signal can be represented as an Arrhenius plot resulting in a straight line with slope $-\frac{E_A}{k_B T}$ and intercept σ_n.

1.2.2 Defect structure: Electron Paramagnetic Resonance spectroscopy

1.2.2.1 General principle

Electron Paramagnetic Resonance (EPR) spectroscopy is a fundamental characterisation technique for systems with one or more unpaired electrons, and has thus become essential to resolve defect structures in crystals since the 1960s. allows to obtain information on the chemical composition and microscopic structure of the local environment of the paramagnetic centers, as well as their concentration and it can also be used as a tool to monitor defect dynamics [16,17].

EPR measurements consist in recording the interaction of magnetic moments of paramagnetic spins with an external magnetic field, as well as with magnetic moments of surrounding species, under the influence of this field. Fig. 1.5 shows a schematic representation of a standard EPR spectrometer, where a sample is placed between electromagnets which generate a strong magnetic field. A microwave beam is produced (at constant frequency) and the generated spectrum corresponds to the resonance absorption of microwave radiation by unpaired electrons in an external (variable) magnetic field.

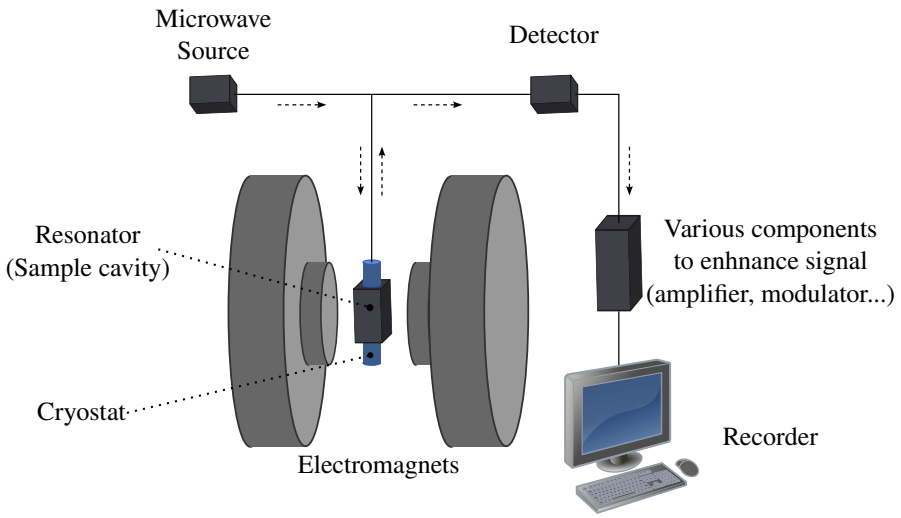

Fig. 1.5: Schematic representation of the main components composing a standard Electron Paramagnetic Resonance spectrometer. The sample is placed within a resonator which concentrates the radiation from the microwave source and allows to tune its frequency to the resonance frequency of the cavity. The cryostat allows to modulate the temperature of the sample during experiments, typically in the 4 – 300 K range although temperatures as low as 1.2 K and as high as 1300 K are also possible [18]. The microwave source emits waves, typically in the X-band (9 – 10 GHz) (or Q-band (34 GHz), sometimes W-band (94 GHz) or higher [18]) frequency, that are guided to the sample cavity which is subjected to a magnetic field generated by the electromagnets. The radiation reflected out from the cavity is then transferred to the microwave detector. Various components can also be included depending on the type of EPR measurement, *i.e.* continuous wave (CW), pulsed EPR or Electron Nuclear Double Resonance (ENDOR) in order to enhance the output signal. The signal is then recorded as absorption lines detected when the separation between energy levels is equal to the photon frequency.

The phenomenon responsible for the EPR signal is the Zeeman effect which describes the splitting of spectral lines in the presence of an external magnetic field [19]. The simplest example for this effect, that of a free electron with spin $S = \frac{1}{2}$ in vacuum, is represented in Fig. 1.6a. When an external magnetic field B_0 is applied to this electron, its magnetic moment μ_e can be oriented either parallel or antiparallel to the field, corresponding to the two possible spin states $M_S = \pm\frac{1}{2}$ of the electron

$$\mu_e = -g_e \mu_B M_S \tag{1.2}$$

where g_e is the free electron g-factor, a very well-known physical constant $g_e = 2.0023193$ [20], and μ_B the Bohr magneton. This leads to a splitting of the energy states of the electron into two sublevels with different energies:

$$E = -\mu_e B_0 = \pm g_e \mu_B M_S B_0 \tag{1.3}$$

The energy difference between these two orientations ΔE is therefore

$$\Delta E = g_e \mu_B B_0 \tag{1.4}$$

The observed EPR spectrum thus corresponds to the transition of the electron between the two states, by photon absorption. This transition only occurs when the microwave frequency is equal to the resonance frequency, as the corresponding energy $h\nu_{MW}$ is then equal to ΔE. In a typical EPR setup, the frequency is held constant while the strength of the magnetic field is varied. Therefore this transition is observed when the intensity of the magnetic field, on which the energy splitting is directly dependent (eq. 1.4), is strong enough so that the equality $\Delta E = h\nu_{MW}$ is valid [18].

A more advanced technique used to characterise systems with unpaired electrons is Electron-Nuclear Double Resonance spectroscopy (ENDOR) [21]. This method is particularly useful in cases where the standard EPR spectrum is too complex and not resolved enough due to peak broadening to properly identify a local structure. It allows to further elucidate the nuclear environment of unpaired electrons by probing the interaction between the nuclear spins of nearby nuclei and the unpaired electron spins. In an ENDOR experiment, the sample is placed in a constant magnetic field, like any EPR setup, and is also subjected to both a microwave and a radiofrequency field, enabling to detect both an EPR and an Nuclear Magnetic Resonance (NMR) spectrum. The resonance condition of the microwave field to obtain the electronic spin states splitting is fulfilled. The radiofrequency field is then applied at a frequency corresponding to the energy difference between nuclear spin states, in order to produce a transition, following the same principle detailed above for EPR signals. The resulting radiofrequency absorption provides information about the nuclear environment around the paramagnetic center, and thus about the interaction between the unpaired electron and nearby nuclei, allowing for the precise identification of specific nuclei and determination of their electronic environment.

1.2.2.2 Magnetic interactions: Electron-Zeeman and hyperfine interactions

In an actual system, the unpaired electron is surrounded by atoms and thus some interactions between the unpaired electron and its local environment modify the shape of the measured signal

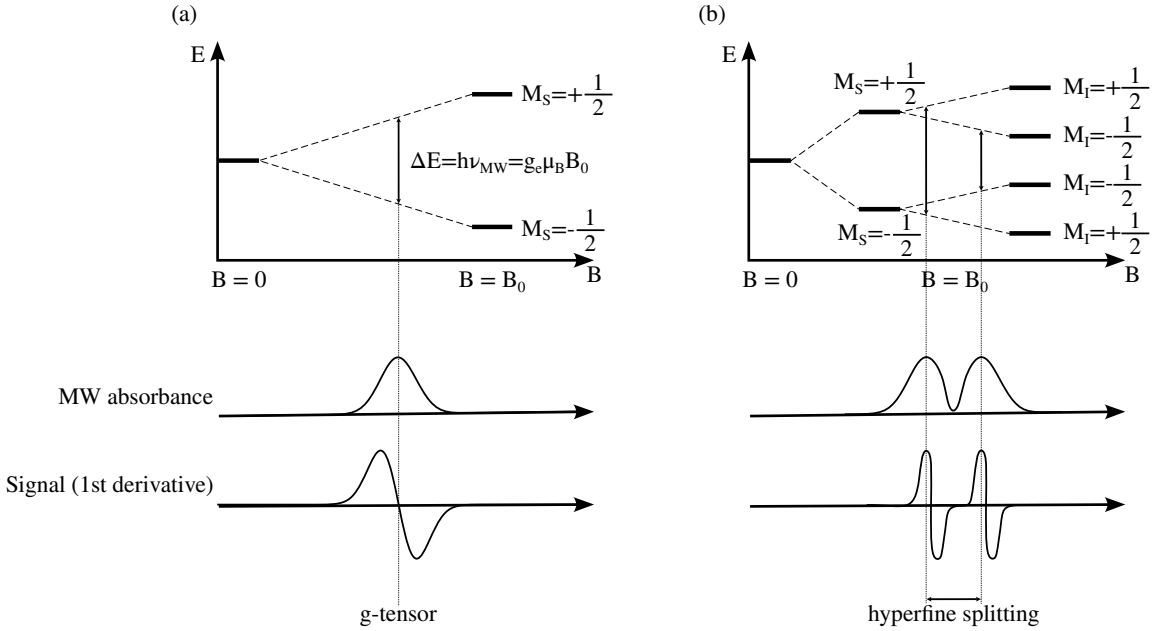

Fig. 1.6: (a) Energy levels for an electron in an applied magnetic field B. The transition between the split states leads to the EPR signal, which corresponds to the first derivative of the absorbance of the microwave (MW) radiation. The center of the peak corresponds to the g-tensor value. (b) Energy levels for a hydrogen atom in an applied magnetic field B. The levels originating from the electron ($M_S = \pm\frac{1}{2}$) are further split due to the induced magnetic field generated by the nucleus characterised by $M_I = \pm\frac{1}{2}$. Only some of the transitions between these levels are allowed, identified by quantum selection rules $\Delta M_S = \pm 1$ and $\Delta M_I = 0$. In the case of the H atom, two transitions are allowed and lead to a doublet signal. The spacing between peaks within a signal correspond to the hyperfine coupling constant.

shown in Fig. 1.6a. These interactions can be quantified by the spin hamiltonian $\hat{H}_{EPR}$ [22]

$$\hat{H}_{EPR} = \hat{H}_{EZ} + \hat{H}_{NZ} + \hat{H}_{HF} + \hat{H}_{NQ} + \hat{H}_{NN} + \hat{H}_{ZFS} \tag{1.5}$$

where each term corresponds to the electron-Zeeman, nuclear-Zeeman, hyperfine, nuclear quadrupole, nuclear-nuclear and zero-field splitting interactions respectively. Regarding the nuclear-Zeeman and nuclear-nuclear terms, they are generally considered negligible in standard continuous-wave EPR in which the magnetic and electric fields are not in the correct bands to produce nuclear spin transitions. Similarly, the systems relevant to this study, *i.e.* light impurity-related defects in silicon, do not commonly have spin $S > \frac{1}{2}$ nor more than one unpaired electrons around a nucleus, thus the nuclear quadrupole and zero-field splitting terms are also neglected. Therefore, the most relevant interactions to the spin hamiltonian consist in the electron-Zeeman $\hat{H}_{EZ}$ and hyperfine $\hat{H}_{HF}$ interactions.

The electron-Zeeman term describes the interaction between the unpaired electron and the magnetic field,

$$\hat{H}_{EZ} = \mu_B \mathbf{B_{eff}} \cdot \overleftrightarrow{g} \cdot \mathbf{S} \tag{1.6}$$

with the applied magnetic field B_0 is replaced by an effective magnetic field $\mathbf{B_{eff}}$ composed

by B_0 and other locally induced magnetic fields, $\mathbf{S}$ the electron spin, and $\overleftrightarrow{g}$ the electron g-tensor of the system which derives from the electron g-factor. This value is a unique identifier for an unpaired electron in a given local environment and corresponds to the center of the EPR absorption peak, as shown in Fig. 1.6a. The g-tensor consists of a 3x3 matrix which is dependent on the system orientation with respect to the magnetic field. Principal values, g_1, g_2, g_3, are extracted and describe the *anisotropy* of the defect structure, thus allowing to obtain information on its local symmetry and electronic distribution. From spectra, a signal can be identified as either isotropic, $g_1 = g_2 = g_3$, axial, $g_1 \neq g_2 = g_3$, or rhombic, $g_1 \neq g_2 \neq g_3$. In the axial case, the components are then referred to as $g_{\parallel} = g_1$ and $g_{\perp} = g_{2,3}$. Furthermore, g_{iso}, can be derived as the average of the g-tensor main values.

The hyperfine term describes the interaction between the magnetic dipoles of the unpaired electron and the nuclei in its environment,

$$\hat{H}_{HF} = \mathbf{S} \cdot \overleftrightarrow{A} \cdot \mathbf{I} \tag{1.7}$$

where $\mathbf{I}$ is the nuclear spin and $\overleftrightarrow{A}$ the hyperfine tensor. This interaction, illustrated in Fig. 1.6b for the simple example of a hydrogen atom, further splits the EPR signal by the interaction of the magnetic moments of the electron with surrounding nuclei. The corresponding possible transitions are restricted by quantum selection rules $\Delta M_S = \pm 1$ and $\Delta M_I = 0$. For the H atom, this leads to two transitions, resulting in an observed doublet in the spectrum where the distance between the peaks corresponds to the hyperfine splitting. Information on the chemical local environment of the unpaired electron can therefore be derived. The term comprises two contributions,

$$\overleftrightarrow{A} = A_{iso} \overleftrightarrow{1} + \overleftrightarrow{A}_{aniso} \tag{1.8}$$

with A_{iso} is the isotropic or Fermi contact term, and $\overleftrightarrow{A}_{aniso}$ the anisotropic or dipolar term. The first component provides information on the nature and the extent to which the paramagnetic electron resides on the nucleus. The value is proportional to the spin density at the nuclei, originating from s orbitals. The second constituent introduces direction-dependent effects due to the interaction between the magnetic dipole moments of the unpaired electron and the nuclear spins. Similarly to the g-tensor, the dipolar term is composed of three diagonal values A_1, A_2, A_3, and A_{iso} is thus equal to a third of the trace of the hyperfine tensor.

1.3 Equilibrium defect structure: the role of spontaneous symmetry breaking

One of the main challenges of defect characterisation lies in the complexity of correlating a specific defect structure with a given spectroscopic signal or property. Each spectroscopy technique provides a distinct information about a sample, and the instrument resolution may limit the differentiation between multiple signals in a spectrum. Furthermore, measured data are more often than not dependent on sample preparation factors, *e.g.* semiconductor growth, doping variations and annealing conditions, leading to varying characteristics across different samples. Consequently, it becomes necessary to couple multiple characterisation techniques in order to

obtain a complete picture of the properties of a defect center. Analysing these properties therefore allows experimenters to propose a defect structure that aligns with the observed signals. However, finding the proper equilibrium defect configuration fitting all experimental evidence for a given sample is undoubtedly non-trivial. Early models were thus developed to elucidate complex behaviours in some systems.

This section focuses on such models which describe intricate phenomena that significantly impact the electronic and geometric properties of materials, *i.e.* the Jahn-Teller (JT) and pseudo Jahn-Teller (pJT) effects. For each effect, the fundamental principles, distinctive features, and their implications on defect structures and electronic properties are explored.

1.3.1 Jahn-Teller effect

The JT effect is a well established phenomenon that describes the spontaneous symmetry breaking (SB) observed in molecules or crystals [23]. This effect, illustrated in Fig. 1.7a, occurs in any non-linear system with a partially filled degenerate ground state. The unequal occupation of orbitals in the electronic structure is unstable and therefore, the system undergoes a geometrical distortion to break the degeneracy, resulting in a lower symmetry and lower overall energy of the system.

In the case of a defect complex with C_{3v} symmetry within a cubic lattice, one of the atoms (*e.g.* on the top left of the lattice in Fig. 1.7a) is shifted from the ideal vertex position, and the three remaining atoms form an equilateral triangle (identified by the three blue segments). The associated electronic structure exhibits a doublet state e. The energy profile of the defect orbitals at the bottom of Fig. 1.7a reveals an instability when a single electronic occupation of the state is considered, as there is no discernible minimum in the configuration (blue dot) [24]. Furthermore, there is a crossing of the two states at this point, meaning that internal forces are driving the distortion. The spontaneous SB mechanism allows to stabilise the system by altering both electronic and atomic structures, *i.e.* the doublet state is split into two singlets a_1 and a_2, and one of the three distances in the previously identified triangle is deformed (either elongated or shortened). This distortion results in a reduction of the symmetry of the system to a C_s structure.

This effect is observed in several key defects in silicon, in particular in the phosphorus-vacancy complex, also referred to as the silicon *E*-center which is rather well known both experimentally and computationally [25–30]. Accordingly, this system will be detailed in a later chapter as a reference to validate the methods applied in this thesis to compute spectroscopic properties.

1.3.2 Pseudo Jahn-Teller effect

The pJT effect is a fundamental extension of the JT effect in that it describes spontaneous SB similar to the JT effect, although in **non**degenerate ground state systems [31]. Fig. 1.7b highlights the differences between the two effects. In the pJT effect, the populated ground state is nondegenerate, yet it is still destabilised with respect to distortion by the presence of

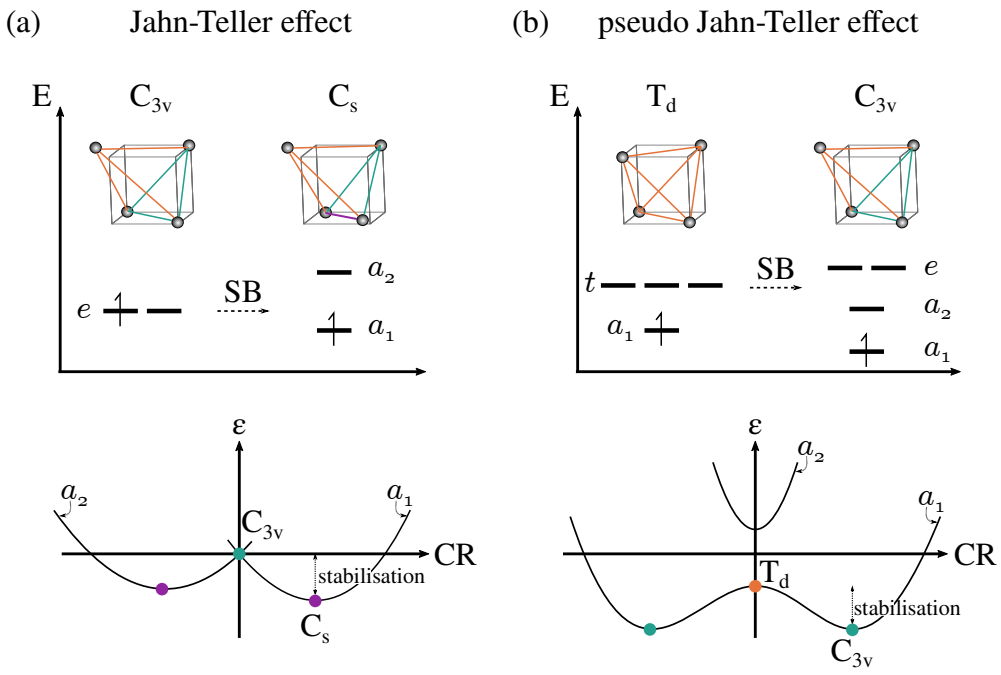

Fig. 1.7: Schematic representation of the (a) Jahn-Teller and (b) pseudo Jahn-Teller effects in crystals. At the top, energy diagrams illustrate the symmetry breaking (SB) mechanisms for the (a) $C_{3v} \rightarrow C_s$ and (b) $T_d \rightarrow C_{3v}$ crystal distortions, along with the corresponding level splittings. Lattices show the atomic structure for each symmetry and coloured segments have been added to emphasize characteristic interatomic distances (segments of the same colour indicate equal distances). At the bottom, the energy profiles of the relevant states along the distortion highlight the distinctive features of each effect. (a) At the high symmetry C_{3v} configuration (blue dot), the states are degenerate and no minimum is observed on the potential energy surface at this point. The resulting distortion stabilises the system in a lower symmetry C_s structure (purple dot). (b) In the case where the degenerate state is close in energy to the non-degenerate filled state, the high symmetry T_d structure is also stabilised in a lower symmetry C_{3v} configuration.

a degenerate excited state of adequate symmetry and sufficiently close in energy. The mixing between the ground and excited states, referred to as pseudodegenerate states due to their proximity, produces an instability analogous to the one caused by the JT effect. It is interesting to note that the pseudodegeneracy condition, *i.e.* that the ground and excited states are close in energy, has no *a priori* limitation in the sense that the pJT effect can occur even for large energy gaps [32]. Although the result of the SB mechanism is similar in both JT and pJT effects, Fig. 1.7b shows a significant difference in the energy profile of the pJT effect. In this case, there is no crossing of the two states at the point of the high symmetry configuration (orange dot) since there is no actual degeneracy. The energy gain resulting from the stabilisation of the system is therefore not due to any force driving the SB. It has been shown that the mechanism is driven by the energy gained from the added covalent bonds formed between atoms in the system by the distortion [33].

Bibliography

[1] N. W. Ashcroft and N. D. Mermin. *Solid State Physics*. Saunders College Publishing, 1976.

[2] M. Lannoo and J. Bourgoin. Atomic configuration of point defects. In *Point Defects in Semiconductors I: Theoretical Aspects*, pages 1–35. Springer Berlin Heidelberg, Berlin, Heidelberg, 1981.

[3] C. Kittel. *Introduction to solid state physics*. John Wiley & Sons, Ltd, 2005.

[4] B. W. Pfennig. *Principles of inorganic chemistry*. John Wiley & Sons, Ltd, 2015.

[5] T. Kita, Y. Harada, and S. Asahi. Fundamentals of semiconductors. In *Energy Conversion Efficiency of Solar Cells*, pages 157–202. Springer Singapore, Singapore, 2019.

[6] V. Orlov, H. Richter, A. Fischer, J. Reif, T. Müller, and R. Wahlich. Mechanical properties of nitrogen-doped CZ silicon crystals. *Materials Science in Semiconductor Processing*, 5(4):403–407, 2002.

[7] V. V. Voronkov and R. J. Falster. Multiplicity of nitrogen species in silicon: The impact on vacancy trapping. In *Gettering and Defect Engineering in Semiconductor Technology XII*, volume 131 of *Solid State Phenomena*, pages 219–224. Trans Tech Publications Ltd, 1 2008.

[8] S. Yuan and D. Yang. Nitrogen impurity in crystalline silicon. *Handbook of Photovoltaic Silicon*, pages 463–494, 2019.

[9] C. R. Alpass, J. D. Murphy, R. J. Falster, and P. R. Wilshaw. Nitrogen diffusion and interaction with dislocations in single-crystal silicon. *Journal of Applied Physics*, 105(1):013519, 2009.

[10] W. V. Ammon, P. Dreier, W. Hensel, U. Lambert, and L. Köster. Influence of oxygen and nitrogen on point defect aggregation in silicon single crystals. *Materials Science and Engineering: B*, 36(1-3):33–41, 1996.

[11] G. S. May and C. J. Spanos. Technology overview. In *Fundamentals of Semiconductor Manufacturing and Process Control*, chapter 2, pages 25–81. John Wiley & Sons, Ltd, 2006.

[12] D. V. Lang. Deep-level transient spectroscopy: A new method to characterize traps in semiconductors. *Journal of Applied Physics*, 45(7):3023–3032, 1974.

[13] S. Kasap and P. Capper. *Springer handbook of electronic and photonic materials*. Springer, 2017.

[14] P. McLarty. Deep level transient spectroscopy (dlts). In H. Haddara, editor, *Characterization Methods for Submicron MOSFETs*, pages 109–126. Springer US, Boston, MA, 1995.

[15] W. Shockley and W. T. Read. Statistics of the recombinations of holes and electrons. *Physical Review*, 87(5):835, 1952.

[16] J. A. Weil and J. R. Bolton. *Electron Paramagnetic Resonance: Elementary Theory and Practical Applications*. John Wiley & Sons, Ltd, 2006.

[17] A. Alessi and F. Gelardi. Electron paramagnetic resonance spectroscopy (EPR). In *Spectroscopy for Materials Characterization*, chapter 9, pages 253–280. John Wiley & Sons, Ltd, 2021.

[18] E. Reijerse and A. Savitsky. Electron paramagnetic resonance instrumentation. In *eMagRes*, pages 187–206. John Wiley & Sons, Ltd, 2017.

[19] P. Zeeman. XXXII. On the influence of magnetism on the nature of the light emitted by a substance. *The London, Edinburgh, and Dublin Philosophical Magazine and Journal of Science*, 43(262):226–239, 1897.

[20] E. Tiesinga, P. J. Mohr, D. B. Newell, and B. N. Taylor. Codata recommended values of the fundamental physical constants: 2018. *Reviews of Modern Physics*, 93:025010, 2021.

[21] J. R. Harmer. Hyperfine spectroscopy – ENDOR. In *eMagRes*, pages 1493–1514. John Wiley & Sons, Ltd, 2016.

[22] M. M. Roessler and E. Salvadori. Principles and applications of EPR spectroscopy in the chemical sciences. *Chemical Society Reviews*, 47(8):2534–2553, 2018.

[23] H. A. Jahn and E. Teller. Stability of polyatomic molecules in degenerate electronic states-I—orbital degeneracy. *Proceedings of the Royal Society of London. Series A-Mathematical and Physical Sciences*, 161(905):220–235, 1937.

[24] I. B. Bersuker. The Jahn–Teller and pseudo-Jahn–Teller effects: a unique and only source of spontaneous symmetry breaking in atomic matter. *Symmetry*, 13(9):1577, 2021.

[25] G. D. Watkins and J. W. Corbett. Defects in irradiated silicon: Electron paramagnetic resonance and electron-nuclear double resonance of the Si-E center. *Physical Review*, 134(5A):A1359, 1964.

[26] G. D. Watkins. Optical properties of group-V atom-vacancy pairs in silicon. *Radiation Effects and Defects in Solids*, 111(1-2):487–500, 1989.

[27] G. D. Watkins. Understanding the Jahn–Teller distortions for the divacancy and the vacancy–group-V-atom pair in silicon. *Physica B: Condensed Matter*, 376:50–53, 2006.

[28] G. Pfanner, C. Freysoldt, J. Neugebauer, and U. Gerstmann. Ab initio EPR parameters for dangling-bond defect complexes in silicon: Effect of Jahn-Teller distortion. *Physical Review B*, 85:195202, May 2012.

[29] K. Szász, T. Hornos, M. Marsman, and A. Gali. Hyperfine coupling of point defects in semiconductors by hybrid density functional calculations: The role of core spin polarization. *Physical Review B*, 88(7):075202, 2013.

[30] G. Herrero-Saboya, L. Martin-Samos, A. Jay, A. Hémeryck, and N. Richard. A comprehensive theoretical picture of E centers in silicon: From optical properties to vacancy-mediated dopant diffusion. *Journal of Applied Physics*, 127(8), 2020.

[31] U. Öpik and M. H. L. Pryce. Studies of the Jahn-Teller effect. I. a survey of the static problem. *Proceedings of the Royal Society of London. Series A. Mathematical and Physical Sciences*, 238(1215):425–447, 1957.

[32] I. B. Bersuker, N. N. Gorinchoi, and V. Z. Polinger. On the origin of dynamic instability of molecular systems. *Theoretica Chimica Acta*, 66:161–172, 1984.

[33] I. B. Bersuker. Pseudo-Jahn–Teller effect–a two-state paradigm in formation, deformation, and transformation of molecular systems and solids. *Chemical Reviews*, 113(3):1351–1390, 2013.

Chapter 2

Computational methods

This chapter introduces the theoretical background used in this study to investigate the electronic properties of defects in semiconductors. First, the theoretical foundation allowing the determination of ground state properties of molecular and solid-state systems through Density Functional Theory (Section 2.1) is described. Next, more specific methods to compute spectroscopic properties of defects, *e.g.* the Electron Paramagnetic Resonance parameters (Section 2.2) and the Charge Transition Levels (Section 2.3) are detailed. The challenges that arise from each method presented are also described throughout the chapter.

2.1 Density Functional Theory: theory and implementation for calculation of electronic structure

Density Functional Theory (DFT) is a widely used quantum mechanical method that plays a fundamental role in understanding the electronic structure and properties for a wide range of molecules and solid materials. It provides an efficient approach to describe their electronic properties, which are fundamental to determine the characteristics of matter at the atomic level. In particular, DFT can produce a variety of microscopic properties of matter such as lattice constants or geometries, as well as macroscopic characteristics, for instance bulk moduli of materials or vibrational frequencies. In this section, the theoretical foundations of DFT and the key practical elements used to implement DFT calculations effectively are outlined.

2.1.1 Theoretical considerations

2.1.1.1 Solving the Schrödinger equation for the N-body problem

Similarly to how classical objects are described using classical mechanics by solving Newton's equations of motion, quantum objects, such as atoms and electrons, are described using quantum mechanics and involve solving the many-body Schrödinger equation. In this paradigm, any N-body system (composed of atoms and electrons) is characterised by its electronic structure which can be obtained by solving the time-independent non-relativistic Schrödinger equation [1]:

$$\hat{\mathrm{H}}\,|\Psi\rangle = \mathrm{E}\,|\Psi\rangle \tag{2.1}$$

Where $\hat{\mathrm{H}}$ is the Hamiltonian operator of the system, Ψ its wavefunction and E the corresponding energy. The Hamiltonian describes the interactions between nuclei and electrons of the system:

$$\hat{\mathrm{H}} = \sum_{\mathrm{i}} -\frac{1}{2}\nabla^2_{\mathbf{r}_\mathrm{i}} + \sum_{\mathrm{A}} -\frac{1}{2\mathrm{M}_\mathrm{A}}\nabla^2_{\mathbf{R}_\mathrm{A}} + \frac{1}{2}\sum_{\mathrm{A}\neq\mathrm{B}} \frac{\mathrm{Z}_\mathrm{A}\mathrm{Z}_\mathrm{B}}{|\mathbf{R}_\mathrm{A}-\mathbf{R}_\mathrm{B}|} + \sum_{\mathrm{i,A}} -\frac{\mathrm{Z}_\mathrm{A}}{|\mathbf{r}_\mathrm{i}-\mathbf{R}_\mathrm{A}|} + \frac{1}{2}\sum_{\mathrm{i}\neq\mathrm{j}} \frac{1}{|\mathbf{r}_\mathrm{i}-\mathbf{r}_\mathrm{j}|} \tag{2.2}$$

With $\mathbf{r}$ and $\mathbf{R}$ the positions of electrons and nuclei, and M and Z the mass and atomic number of the nuclei (in atomic units). The first two terms correspond to the kinetic energy operators for electrons and nuclei, and the following three to nuclei-nuclei, nuclei-electron and electron-electron interaction operators respectively. This Hamiltonian can then be written in a compact form as:

$$\hat{\mathrm{H}} = \hat{\mathrm{T}}_\mathrm{e} + \hat{\mathrm{T}}_\mathrm{n} + \hat{\mathrm{V}}_\mathrm{nn} + \hat{\mathrm{V}}_\mathrm{en} + \hat{\mathrm{V}}_\mathrm{ee} \tag{2.3}$$

This equation has an exact solution only for one electron systems, and becomes practically unsolvable for bulk solids where typically $\mathrm{N} \sim 10^{23}$ atoms, so some approximations are necessary to obtain approached solutions. The most important one is the Born-Oppenheimer approximation, which allows to treat separately the components of the Hamiltonian concerning the electrons and those concerning the nuclei. Since electrons have a mass that is 1800 times lighter than that of nuclei [1], they move considerably faster than nuclei. It is then considered

that electrons move in a field of fixed nuclei, and thus possible to establish a simplified electronic Schrödinger equation in which the nuclei positions become parameters of the electronic wavefunction. The corresponding electronic Hamiltonian is then written in a compact way as:

$$\hat{\mathrm{H}}_{\mathrm{elec}} = \hat{\mathrm{T}}_{\mathrm{e}} + \hat{\mathrm{V}}_{\mathrm{en}} + \hat{\mathrm{V}}_{\mathrm{ee}} \tag{2.4}$$

With this approximation, the nuclei move in a mean field of electrons, along a Potential Energy Surface (PES). The electronic coordinates are then replaced by average values over all electronic wavefunctions obtained by solving the Schrödinger equation [2].

2.1.1.2 Wavefunction method: the Hartree-Fock approximation

The main issue in solving the eigenvalue problem for the Hamiltonian in 2.4 consists in finding its solutions for many-electrons. In such systems, the correlation between electrons makes it impossible to provide an analytical solution to the Schrödinger equation since electrons cannot be treated independently from one another. In order to approximate the exact wavefunction, several approaches exist. Historically, the first method developed to solve the Schrödinger equation consisted in computing the electron wavefunction directly through the Hartree-Fock (HF) approximation [2].

It is a mono-determinental method as the wavefunction is defined as the product of independent single-electron wavefunctions $\chi_{\mathrm{j}}(\mathbf{x}_{\mathrm{i}})$, with $\mathbf{x}_{\mathrm{i}}$ the positions of the electron in spin state i. These so-called *spin-orbitals* are eigenfunctions of single-electron Hamiltonians h_{i}, with:

$$\hat{\mathrm{H}}_{\mathrm{elec}} = \sum_{\mathrm{i}} h_{\mathrm{i}} \tag{2.5}$$

In this case, electron-electron interactions are neglected and the Hamiltonian that describes the system is the product of a set of spin-orbitals.

In order to satisfy the Pauli exclusion principle, the total wavefunction has to be antisymmetric, and as such, the spin-orbital product is an antisymmetric product obtained by using a Slater determinant (SD):

$$\Psi^{\mathrm{SD}}\left(\mathbf{x}_1, \mathbf{x}_2, \ldots, \mathbf{x}_{\mathrm{i}}, \mathbf{x}_{\mathrm{j}}, \ldots, \mathbf{x}_{\mathrm{n}}\right) = \frac{1}{\sqrt{\mathrm{N!}}} \begin{vmatrix} \chi_1\left(\mathbf{x}_1\right) & \chi_2\left(\mathbf{x}_1\right) & \cdots & \chi_{\mathrm{N}}\left(\mathbf{x}_1\right) \\ \chi_1\left(\mathbf{x}_2\right) & \chi_2\left(\mathbf{x}_2\right) & \cdots & \chi_{\mathrm{N}}\left(\mathbf{x}_2\right) \\ \vdots & \vdots & & \vdots \\ \chi_1\left(\mathbf{x}_{\mathrm{N}}\right) & \chi_2\left(\mathbf{x}_{\mathrm{N}}\right) & \cdots & \chi_{\mathrm{N}}\left(\mathbf{x}_{\mathrm{N}}\right) \end{vmatrix} \tag{2.6}$$

with $\mathbf{x}$ and χ denoting electrons and spin-orbitals respectively.

The total energy corresponding to this wavefunction is then defined as the expectation value of the Hamiltonian on the corresponding Slater determinant:

$$\begin{aligned} \mathrm{E}^{\mathrm{SD}} &= \langle \Psi^{\mathrm{SD}} | \, \hat{\mathrm{H}} \, | \Psi^{\mathrm{SD}} \rangle \\ &= \sum_{\mathrm{i}} \mathrm{h}_{\mathrm{ii}} + \frac{1}{2} \sum_{\mathrm{i}} \sum_{\mathrm{i>j}} (\mathrm{J}_{\mathrm{ij}} - \mathrm{K}_{\mathrm{ij}}) \end{aligned} \tag{2.7}$$

where h_{ii} is the mono-electronic term, J_{ij} the Coulomb integral which describes the Coulomb interaction between electrons and K_{ij} the exchange integral which describes the antisymmetry property for the exchange between two electrons. This implies that the electronic interaction is treated as the interaction between a single electron and the mean field generated by all other electrons, rather than considering the interactions between individual electrons [2].

The HF method respects the variational principle in that the spin-orbitals in the SD are such that the derived energy is minimised. The corresponding coefficients are then optimized in order to obtain the minimum energy. This is achieved by a Self Consistent Field (SCF) method which consists in starting from a first guess approximation of the spin-orbitals, close to the desired ones. A first set of wavefunctions is then derived for the system and its corresponding energy determined. A new set of spin-orbitals is estimated from this energy, supposedly more accurate than the first guess. From there, the calculations are iteratively performed, adjusting the spin-orbitals until a consistent and accurate set of orbitals is obtained.

However, as previously mentioned, this method does not take into account electron correlation. Moreover, it poses another issue in that long distance interactions are not correctly described. This is due to the approximations at the foundation of the theory [2], and several approaches were developed to attempt to include electron correlation.

2.1.1.3 From wavefunction to electronic density: the Hohenberg-Kohn theorems

DFT is a less computationally expensive alternative to the HF method in that it reformulates the many-body problem in terms of the electron density of the system rather than in its wavefunction. The electronic density only depends on the 3 space variables, whereas the wavefunction is dependent on the 4N space and spin coordinates of the N-electrons system. This change drastically lowers the calculation time and cost [3].

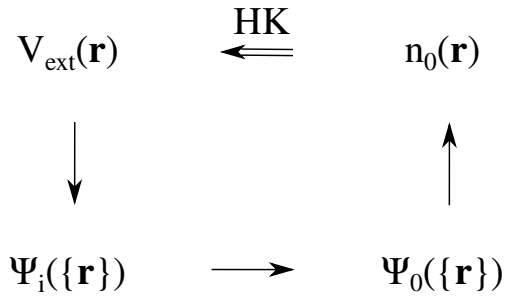

Fig. 2.1: Schematic representation of the Hohenberg-Kohn theorem (HK). The double arrow illustrates the HK theorem, and the single arrows indicate the resolution of the Schrödinger equation. From the external potential $V_{ext}(\mathbf{r})$, the states of the system $\Psi_i((\mathbf{r}))$ are derived, among which is the ground state state $\Psi_0((\mathbf{r}))$ and the corresponding density $n_0(\mathbf{r})$. Adapted from [4].

From the N-body problem, we aim to determine the ground state energy E_0. By the

variational principle, it is obtained as:

$$E_0 = \min_{\Psi} \langle \Psi | \hat{H} | \Psi \rangle \tag{2.8}$$

With Ψ the wavefunction and $\hat{H}$ the Hamiltonian. This expression can be reformulated in terms of electronic density as:

$$n(\mathbf{r}) = N \int \cdots \int |\Psi(x_1, x_2, \ldots, x_N)(\mathbf{r})|^2 d\sigma dx_2 \ldots dx_N \tag{2.9}$$

Where $n(\mathbf{r})$ is the ground state density. The first Hohenberg-Kohn (HK) theorem [5] states that the external potential $V_{ext}(\mathbf{r})$ is determined by the ground state particle density $n_0(\mathbf{r})$, uniquely up to an arbitrary constant. From the electronic density, it is then possible to determine the potential (up to a constant) that allows to obtain the Hamiltonian of the system. A universal functional for the energy $F[n]$ can then be defined in terms of the density $n_0(\mathbf{r})$:

$$F[n] = \langle \Psi[n] | | \hat{T} + \hat{V}_{ee} | \Psi[n] \rangle \tag{2.10}$$

This functional is independent from the external potential, and the functional for the electronic energy is derived as:

$$E[n] = F[n] + \int V_{ne}(\mathbf{r}) n(\mathbf{r}) d\mathbf{r} \tag{2.11}$$

for the external potential V_{ne} of the system.

It is interesting to note that the wavefunction $\Psi[n]$ is not always unique, *e.g.* for degenerate ground states. However, in such cases, these wavefunctions still yield a unique functional $F[n]$ [3]. The second HK theorem [5] states that this energy obeys the variational principle: the minimum ground state energy is obtained for the corresponding minimum electronic density.

In conclusion, as illustrated in Fig. 2.1, the ground state electronic density $n_0(\mathbf{r})$ determines the potential $V_{ext}(\mathbf{r})$, from which the Hamiltonian $\hat{H}$ is derived, and therefore all observable properties of the system.

2.1.1.4 The Kohn-Sham method

Up to this point DFT is an exact theory, however it does not provide a definition of the true universal energy functional [4]. This is due to the difficulties in expressing $\hat{T}$ as a functional of the density. The Kohn-Sham (KS) method [6] consists in mapping the interacting electron system of the N-body problem (described by the Hamiltonian Eq. 2.2) onto a fictitious non-interacting system of electrons with the same electron density. This premise results in the decomposition of Eq. 2.10 as:

$$F[n] = T_s[n] + E_{Hxc}[n] \tag{2.12}$$

where $T_s[n]$ is the kinetic energy functional of the non-interacting system, which can now be defined and calculated, and $E_{Hxc}[n]$ the Hartree-exchange-correlation functional, such that:

$$E_{Hxc}[n] = E_H[n] + E_{xc}[n] \tag{2.13}$$

with $E_H[n]$ the Hartree energy functional, which corresponds to the classical electrostatic repulsion energy for the charge distribution n(r) and can be calculated, and $E_{xc}[n]$ the exchange-correlation (XC) functional. The energy functional Eq. 2.11 can then be re-written as:

$$E[n] = T_s[n] + E_H[n] + E_{xc}[n] + \int V_{ne}(\mathbf{r})n(\mathbf{r})d\mathbf{r} \tag{2.14}$$

The XC term corresponds to the energy contribution of interacting electrons, both kinetic and potential, and its exact expression is not known. The exchange part of this term corresponds to the quantum mechanical phenomenon arising due to the indistinguishability of electrons as identical particles. According to the Pauli exclusion principle, two electrons in an atom or molecule cannot occupy the same quantum state simultaneously. As a result, the wavefunction of the system must be antisymmetric under the exchange of electron coordinates, which leads to the repulsion between electrons of same spin. The correlation part refers to the complex and non-local quantum mechanical electron-electron interactions in the system.

The KS equations allow to describe the energy functional in Eq. 2.14 using a set of single-determinant wavefunctions $\Phi[n]$ which are called KS wavefunctions. They are constructed from a set of orthonormal spin-orbitals $\varphi_i(\mathbf{r})$, and so, for each non-interacting single electron, the KS equations are:

$$\begin{gathered} \hat{H}\varphi_i(\mathbf{r}) = \varepsilon_i\varphi_i(\mathbf{r}) \\ \left[-\frac{1}{2m}\nabla^2 + V_{KS}(\mathbf{r})\right]\varphi_i(\mathbf{r}) = \varepsilon_i\varphi_i(\mathbf{r}) \end{gathered} \tag{2.15}$$

where the Hamiltonian is expressed by its two components of kinetic energy and effective KS potential $V_{KS}(\mathbf{r})$ which includes the external potential and both Hartree and XC potentials. As the KS wavefunctions are single-determinant orbitals, the numerical method to solve these equations and minimize the energy is similar to that of the HF method, with an SCF method, as described in Section 2.1.1.2.

In conclusion, if the exact form of $E_{xc}[n]$ is known, it becomes possible to solve the equation and obtain an exact electronic density and ground state energy of the system. However, it is only possible to solve it for a non-interacting system in an effective potential of the interacting system (Fig. 2.2). The approximation of this XC term is the core challenge in the development of DFT-based methods.

It is important to note that the KS orbitals, and thus KS single particle energies, hold no direct physical meaning. The KS orbitals are solutions to a set of single-particle equations obtained by treating a non-interacting system instead of the real interacting one, and these electron interactions are included only as a mean-field in the XC potential. Therefore, KS orbitals do not represent the actual N-body wavefunction of the interacting electrons in the system, rather only that of the screened single-particle system.

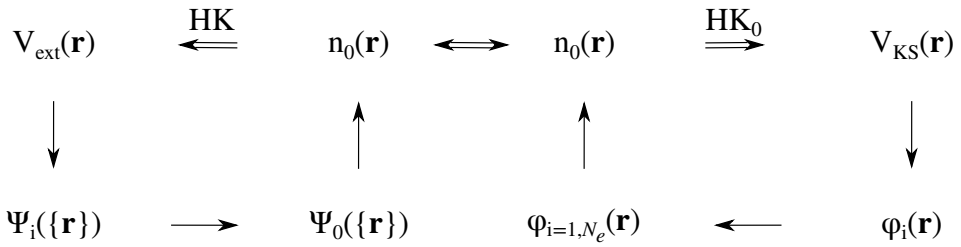

Fig. 2.2: Schematic representation of the Kohn-Sham method (KS). The interacting electron system (HK) is mapped on a non-interacting system (HK_0) by applying the KS method. With this method, it is possible to obtain all properties of the full N-body system with the non-interacting system as starting point. Adapted from [4].

2.1.1.5 Extension to spin density functional theory

It is interesting to note that for systems in an external magnetic field, the spin density is also included in the energy functional as well as the electronic density [4]. This leads to an overall density functional which includes both electronic and spin densities:

$$\begin{aligned} n(\mathbf{r}) &= n(\mathbf{r}, \sigma = \uparrow) + n(\mathbf{r}, \sigma = \downarrow) \\ s(\mathbf{r}) &= n(\mathbf{r}, \sigma = \uparrow) - n(\mathbf{r}, \sigma = \downarrow) \end{aligned} \tag{2.16}$$

This extension is useful for spin-polarized DFT calculations, where $n(\mathbf{r}, \uparrow) \neq n(\mathbf{r}, \downarrow)$, *e.g.* cases with unpaired electrons, as is relevant for modelling physical systems which are studied with EPR spectroscopy. In such cases, the energy functional in Eq. 2.14 becomes:

$$E[n_\uparrow, n_\downarrow] = T_s[n_\uparrow, n_\downarrow] + E_H[n] + E_{xc}[n_\uparrow, n_\downarrow] + \int V_{ne}(\mathbf{r}) n(\mathbf{r}) d\mathbf{r} \tag{2.17}$$

and the corresponding KS equations (Eq. 2.15):

$$\left[-\frac{1}{2m}\nabla^2 + V_{ne}(\mathbf{r}) + V_H(\mathbf{r}) + V_{xc,\sigma}(\mathbf{r}) \right] \varphi_{i\sigma}(\mathbf{r}) = \varepsilon_{i\sigma} \varphi_{i\sigma}(\mathbf{r}) \tag{2.18}$$

2.1.2 Practical aspects of ground state calculations

2.1.2.1 Exchange-correlation functionals

There are several families of approximations for the XC functional. The simplest one is the Local-Density Approximation (LDA) [6], which consists in assimilating the system, locally, to a homogeneous electron gas. In this approximation, the XC functional of the inhomogeneous system corresponds to the XC energy per particle in this electron gas. Thus the energy is dependent only on the local value of the electronic density. Despite this simplistic approach, these functionals yield surprisingly accurate results. A more sophisticated family of functionals is the Generalized-Gradient Approximations (GGA) [7]. In this semilocal approximation, is

dependent on both the density and its gradient, *i.e.* its first derivative. Many GGA functionals have been developed, such as the one used throughout this manuscript. The Perdew-Burke-Ernzerhof (PBE) functional [8] is often used to study solids as it qualitatively describes Van Der Waals interactions and non-local effects.

The XC functional is responsible for incorporating the effects of electron-electron interactions into the electronic energy calculation. However, the functionals used in standard DFT approaches suffer from self-interaction (SI) errors. This problem occurs when each electron is treated as interacting with a mean-field potential created by all other electrons which includes itself. As a result, the electron is partially treated as interacting with its own charge, leading to an artificial electron-electron repulsion. This spurious self-repulsion causes the electron to be overly delocalized and the electron density to spread out more than it should, leading to inaccuracies in the description of electronic properties.

Further developments of the XC functionals derive from the GGA family and attempt to improve the description of electronic correlation effects and mitigate problems that arise from this method. Hybrid functionals, which include a fraction of XC from the HF approximation to that from DFT [9], manage to partially correct the SI problem for example. Meta-GGA functionals, which consider higher-order derivatives of the electron density [10], aim to better describe the non-local behaviour of the electron density.

2.1.2.2 The supercell representation and periodic boundary conditions

To represent the crystal structure, a supercell (SC) representation is commonly used, in particular when studying point defects. The set of characteristic atomic positions and lattice vectors of the crystal are defined in a primitive unit cell of side length a, using three-dimensional Cartesian coordinates. This cell contains the minimal number of atoms required to define the crystal's structure, and is the smallest repeating unit used to generate the entire lattice. The primitive cell is then replicated along all crystallographic axes in order to obtain a larger cell, which contains multiple replicas of the crystal structure. The resulting unit cell is the SC (Fig. 2.3). Within this framework, each atom in a cell will interact with atoms both in its cell and with their replicas in neighbouring cells. This approach is essential in DFT calculations as it allows to study larger systems and describe more accurately the properties of the modelled structure.

To mimic the infinite crystal lattice, Periodic Boundary Conditions (PBC) are applied. This means that any particle or wavefunction that exits one side of the supercell re-enters from the opposite side, as if the SC was itself periodically repeated in space. These PBC therefore allow to effectively reproduce interactions in an infinite crystal while keeping the computational cost reasonable.

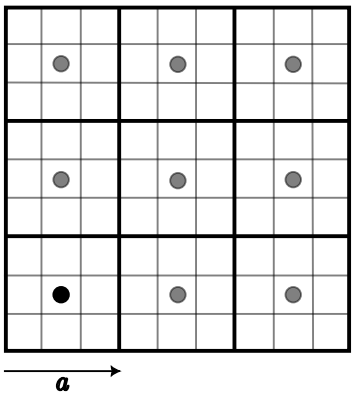

Fig. 2.3: Schematic representation of the supercell (SC) method. The original primitive cell in the bottom left corner (black dot) is replicated twice along two crystallographic axes (grey dot). The resulting SC thus contains 9 primitive cells.

2.1.2.3 Plane waves basis set and k-points

The use of plane waves (pw) basis sets is particularly appropriate for the description of periodic systems, such as crystals in a SC representation, as they naturally satisfy the PBC. In this representation, the arrangement of atoms creates a periodic potential and the eigenstates of the corresponding electronic wavefunctions satisfy Blöch's theorem [11, 12] which is expressed as:

$$\psi_{n\mathbf{k}}(\mathbf{r}) = e^{i\mathbf{k}\cdot\mathbf{r}} u_{n\mathbf{k}}(\mathbf{r}) \tag{2.19}$$

where $\psi_{n\mathbf{k}}(\mathbf{r})$ is the Bloch wavefunction for the n-th energy band and wavevector $\mathbf{k}$, $e^{i\mathbf{k}\cdot\mathbf{r}}$ the pw component of the Blöch wavefunction and $u_{n\mathbf{k}}(\mathbf{r})$ its periodic part, with identical spatial periodicity as the crystal lattice. This formulation makes it efficient to solve Schrödinger's equation as the periodic function $u_{n\mathbf{k}}(\mathbf{r})$ can be written in the form of a Fourier transform:

$$u_{n\mathbf{k}}(\mathbf{r}) = \sum_{\mathbf{G}} c_{(\mathbf{k}+\mathbf{G})} e^{i\mathbf{G}\cdot\mathbf{r}} \tag{2.20}$$

with $\mathbf{G}$ the reciprocal lattice vectors and $c_{(\mathbf{k}+\mathbf{G})}$ the Fourier coefficients. The Blöch wavefunction is expanded in the pw basis set to:

$$\psi_{nk}(\mathbf{r}) = \sum_{\mathbf{G}} c_{(n,(\mathbf{k}+\mathbf{G}))} |\mathbf{k}+\mathbf{G}\rangle \tag{2.21}$$

And the KS equation in Eq. 2.15 is modified in the Fourier space as:

$$\sum_{\mathbf{G_2}} \hat{H}_{(\mathbf{G_1},\mathbf{G_2})}(\mathbf{k}) c_{(n,\mathbf{G_2})}(\mathbf{k}) = \varepsilon_i(\mathbf{k}) c_{(n,\mathbf{G_1})}(\mathbf{k}) \tag{2.22}$$

With $\mathbf{G_1}$ and $\mathbf{G_2}$ reciprocal lattice vectors which differ by another lattice vector. The eigenvectors and eigenvalues of the Schrödinger equation defined above are independently defined for each wavevector $\mathbf{k}$ (within one cell). This implies that for each $\mathbf{k}$, a set of eigenstates ε_i is obtained, and in the infinite crystal limit this discrete set becomes a continuous energy band.

Since it is practically unfeasible to work with a basis set with an infinite number of pw, it is necessary to define a cutoff energy E_{cut} in order to truncate the sum. Only pw with kinetic energies lower than this cutoff are included. Furthermore, Eq. 2.22 is solved in the reciprocal lattice, which is the Fourier transform of the direct space for a periodic crystal. The Brillouin zone (BZ) corresponds to the first primitive, or Wigner-Seitz, cell of this reciprocal lattice and has many essential properties. The sampling of this BZ cannot be done over an infinite number of k wavevectors, *i.e.* a finite set of k-points needs to be defined to perform the integration.

The technique widely used to sample the BZ is the Monkhorst–Pack [13, 14] scheme (MP). In this method, the defined grid divides each dimension of the reciprocal lattice into a specified number of points. The grid is centered at the gamma point (Γ), which corresponds to the center of the BZ in the cubic lattice system. It is then specified using the notation 'nkx × nky × nkz' where each component is the number of points in the x, y, and z directions respectively. By choosing different values of nk one can control the density of k-points in the BZ and the accuracy of the sampling.

To achieve accurate and converged DFT calculations, it is crucial to understand the relationship between the variables of interest and these parameters. Thus, conducting tests to ensure their convergence becomes necessary.

2.1.2.4 Pseudopotentials

In a solid (or molecule), the electronic structure problem involves solving the Schrödinger equation for all electrons. This *all-electrons* approach is however too expensive for DFT calculations as it requires high-energy, rapidly oscillating pw to describe accurately the behaviour of the wavefunctions near the atomic cores. In practice, only valence electrons, which occupy a region far from the atomic nuclei, are responsible for most of the chemical and physical properties of the solid. *Pseudopotentials* (PP) provide an approximation of the interactions for core electrons in a more computationally efficient manner, while fully describing the valence electrons interactions. In this so-called *frozen-core* approximation, the core electrons density in the pseudized region is replaced with a simplified smooth potential, designed to retain the essential features of the electron interactions while neglecting the rapidly varying and high-energy oscillations associated with the inner-core electrons. With this method, the size of the basis set is reduced and so the computational resources necessary to perform the calculations decrease.

There are different types of PP, which each provide distinct advantages depending on the system, the level of accuracy required or the computational resources available. Among the various types of PP, a commonly used kind are *ab initio* norm-conserving PP, as they provide a good compromise between accuracy and computational efficiency. Their main characteristic is that they are constructed to conserve the norm of the all-electron wavefunctions within the pseudized region. The potentials are also constructed to fit properties calculated for the isolated atoms and not fitted to experiments. All these characteristics render these PP more accurate and transferable (*i.e.* independent of the chemical environment) than other types.

In this study, DFT calculations were performed using norm-conserving Troullier-Martins PP with GIPAW reconstruction for core electrons [15], as found in [16]. The details concerning the PAW and GIPAW methods as well as the reconstruction to the PP are detailed in Section 2.2.

2.1.2.5 The band gap problem

As powerful a tool as DFT is for studying the electronic structure and properties of complex many-electron systems, there are some cases for which it presents some limitations and inaccuracies due to its inability to provide an exact solution for the Schrödinger equation. The most important and well-known of these issues is the systematic underestimation of the band gaps for semiconductors and insulators which can lead to incorrect predictions of the electronic properties for materials.

The fundamental gap of any semiconductor (or insulator) corresponds to the difference between its ionisation potential (IP) and electron affinity (EA) [17]. In the KS framework detailed in Section 2.1.1.4, it is also possible to express the band gap for any system with N electrons as a difference of KS total energies:

$$E_g = (E_{N-1} - E_N) - (E_N - E_{N+1}) \tag{2.23}$$

which can be derived to:

$$E_g = \varepsilon_{N+1} - \varepsilon_N + \Delta_{xc}^N \tag{2.24}$$

where ε_{N+1} and ε_N correspond to the lowest unoccupied (LUMO) and highest occupied (HOMO) KS orbitals respectively. This equation establishes that the difference between the KS states cannot be directly matched with the fundamental gap, and a rather large contribution to it Δ_{xc}^N arises from the discontinuity in the derivative of the exchange-correlation functional with respect to the number of electrons. Because of this effect, the band gap calculated with standard DFT calculations is systematically underestimated.

This band gap problem can be addressed and corrected using other more advanced XC functionals (*e.g.* hybrid and meta-GGA functionals) which provide improvement over standard functionals for some properties such as the band gap. In the case of hybrid functionals, which combine a fraction of HF exchange with the XC functionals from standard DFT, this involves tuning the fraction of XC to fit to the experimental band gap. This empirical correction however undermines the predictive capability of DFT calculations.

Another way to improve the accuracy of DFT calculations is through many-body perturbation theory with the GW approximation [18]. This approach is employed for predicting electronic excitations in addition to ground states in molecular compounds and materials, which allows to solve some well-known issues of DFT such as the self-interaction error, the absence of long-range polarization effects and the band-gap problem. This framework introduces the concept of *quasiparticles*, which describe the behaviour of interacting particles (*i.e.* both electrons and holes) as individual entities. The N-body problem is therefore simplified to single-particle interactions, which include the perturbation generated by each quasiparticle in the mean-field of other particles. In this case, the interaction between a single electron with all other electrons

in the system is reduced to the interaction with the perturbated immediate surrounding. This interaction within the quasiparticle, is referred to as the GW self-energy and accounts for the dynamical screening between electrons in a system. The GW method is however not commonly employed as it requires significant computational resources and very careful convergence and validation of the results.

2.1.2.6 Calculations of electronic structure and related properties

As stated previously, to solve the KS equations an SCF method is employed. Starting from a trial electron density, a first estimation of the effective potential is derived and included in the KS equations. The resulting wavefunctions are then used to compute a new, supposedly more accurate density. This cycle is iterated, generating a new guess by mixing both old and new densities, until two consecutive density estimates converge within a given accuracy threshold.

For DFT calculations, in order to have the initial guess of the electronic density as close as possible to the final density, *i.e.* to the real system, and thus save some computational time, it is judicious (even necessary) to perform calculations on optimised atomic structures. This is accomplished using a structure optimisation algorithm which consists in finding the atomic structure which minimises the total energy of the system. The energy of the initial guess is determined by an SCF cycle. Forces on each atom are then obtained as the derivative of the the total energy with respect to atomic positions. The positions of atoms are then updated based on these estimations, and the corresponding energy of the new structure is computed. This process is repeated iteratively to reach an energy minimum. As a result, the overall optimisation cycle requires convergence over two parameters, forces on atoms and electronic density.

Some key properties can be revealed through the study of atomic diffusion within the system, specifically the relative stability between different atomic configurations and how the system may evolve between them. This can be done by investigating the potential energy surface (PES) which is the energy landscape that depicts the total potential energy of the system as a function of the atomic positions (or any other reactional coordinates). As established previously, due to the Born-Oppenheimer approximation, electrons are assumed to instantaneously adjust to the positions of the nuclei. This enables separate treatment of the ground state electronic structure of each nuclear configuration for each point in the coordinate space. This in turn allows to map out the PES and identify stationary points of the surface. These are points for which the gradient of the potential with respect to nuclear positions (*i.e.* forces on atoms) is zero. As such, stable structures correspond to minima, whereas transition states are found at maxima or saddle points of the surface.

The Nudged Elastic Band (NEB) method [19] is commonly employed to explore the PES. This method consists in identifying the most energetically favorable transition pathway between critical points in the surface. It provides the Minimum Energy Path (MEP) with respect to a given nuclear shift connecting optimised configurations of the structure. The corresponding transition activation energy is then computed as the energy difference between the transition state and the initial stable state. In practice, a set of intermediate 'images' is placed between initial and final states, defining a first transition pathway (a simple linear interpolation between states). The images are connected with springs to create an elastic band, with the forces acting

on each image based on the energy gradients (forces) with respect to the nuclear coordinates. A 'nudging' technique is then introduced that ensures the forces are perpendicular to the band's direction. This nudging allows the band to smoothly follow the most energetically favorable pathway. Through an iterative process, the forces on each image are minimised to obtain a local minimum energy configuration. This process is repeated until the energy is minimised along the pathway, and the transition state is accurately located. This ensures that the pathway corresponds to the MEP between initial and final states.

2.2 EPR parameters: the GIPAW approach

To obtain an accurate picture of the magnetic properties of defects in solids, it is necessary to compute their spectroscopic signature, through the calculation of EPR parameters which include the $\overleftrightarrow{\mathrm{g}}$-tensor and hyperfine coupling tensor $\overleftrightarrow{\mathrm{A}}$. Some of these properties explicitly depend on the electronic density at the nucleus, which is not described well enough by standard pseudopotentials where the core regions are defined as an effective potential only. The Gauge Including Projector Augmented Wave (GIPAW) method is a computational approach used to perform calculations of magnetic properties in periodic solids [15, 20]. It is an extension of the projector augmented wave (PAW) method [21], which includes core electrons of atoms into the pseudopotential, instead of a simplified effective potential. This allows for better description of the core region of the system and of the interactions between core and valence electrons, which in turn gives a more accurate description of the magnetism of the system.

The PAW method employs two sets of wavefunctions: all-electron wavefunctions, which represent the true electronic wavefunctions (including both core and valence electrons), and pseudo-electron wavefunctions, where only valence electrons are explicitly described. An augmentation region is introduced around each atomic nucleus, which includes both core and valence electrons. The most common approach to define the augmentation region is as a sphere around each atomic nucleus. The radius of the sphere is chosen to include all electrons within a certain percentage of the muffin-tin radius of the atom. This approach ensures that the augmentation region encompasses most of the electronic charge of the atom. The pseudo-wavefunctions are then improved by introducing projector functions for electrons within this region, which match the all-electron core wavefunctions. The pseudo-wavefunctions are corrected by projecting the all-electron wavefunctions onto these projector functions. By using this method, the PAW method accurately accounts for core electron effects on valence electrons and ensures that the wavefunctions capture the behavior of the valence electrons accurately, while still incorporating the effect of core electrons through the projector functions.

The GIPAW approach is an extension of the PAW method as it goes one step further in the description of core electrons. The standard PAW formalism ensures gauge invariance for all physical observables. However, when dealing with magnetic properties that involve additional effects from core electrons (such as hyperfine coupling constants or magnetic response properties), there can be some gauge-dependent contributions which arise due to the treatment of core electrons with pseudopotentials. These contributions can become significant, especially

when dealing with systems with unpaired electrons. To address this issue and ensure full gauge invariance for magnetic properties in such situations, the GIPAW method was developed [15,20] by introducing core reconstruction. This method consists in constructing gauge-invariant projectors to describe the behaviour of both core and valence electrons within the augmentation region, rather than only valence electrons as with the PAW projectors. This step ensures gauge invariance in the calculation of magnetic properties in solids.

2.2.1 Computation of the g-tensor

As seen in Section 1.2.2, the electronic $\overleftrightarrow{g}$-tensor of a system with a paramagnetic electron (S = 1/2) can be derived from the Zeeman (EZ) splittings of the energy levels caused by the interaction between the external magnetic field and the unpaired electron:

$$\hat{H}_{EZ} = \mu_B \mathbf{B_{eff}} \cdot \overleftrightarrow{g} \cdot \mathbf{S} \tag{2.25}$$

With μ_B the Bohr magneton, $\mathbf{B_{eff}}$ the effective magnetic field, and $\mathbf{S}$ the electron spin. The $\overleftrightarrow{g}$ tensor corresponds to the expansion of the effective Hamiltonian in terms of both the magnetic field and electron spin, and can thus be treated as a second-order perturbation to the effective spin Hamiltonian [22,23]:

$$\overleftrightarrow{g} = \frac{2}{\alpha} \frac{\partial^2 \langle \Psi | \, | \hat{H}_{eff} \, | \Psi \rangle}{\partial \mathbf{B} \partial \mathbf{S}} \bigg|_{\mathbf{B}=\mathbf{S}=0} \tag{2.26}$$

Where α is the fine structure constant. The calculation of the $\overleftrightarrow{g}$-tensor involves applying a perturbation to the system in the form of an external magnetic field. The $\overleftrightarrow{g}$-tensor can then be computed from second-order perturbation theory, which states that the electronic wavefunction must be computed up to first order in one of the perturbations only [24–26]. This leads to expressing the tensor as a shift with respect to the Landé g-factor g_e which corresponds to the g value for a free electron in vacuum:

$$\overleftrightarrow{g} = g_e \overleftrightarrow{1} + \Delta\mathbf{g}_{Zke} + \Delta\mathbf{g}_{SO} + \Delta\mathbf{g}_{SOO} = g_e \overleftrightarrow{1} + \Delta\mathbf{g} \tag{2.27}$$

Where $\Delta\mathbf{g}_{Zke}$ is the correction due to the Zeeman kinetic energy, which accounts for relativistic effects in the motion of the electron in the presence of an external magnetic field. $\Delta\mathbf{g}_{SO}$ corresponds to the correction due to the spin-orbit coupling which arises from the interaction between the electron's spin and its orbital motion, leading to relativistic effects on the magnetic response. For the systems studied in this work, this contribution is the largest correction to g_e.

Finally, $\Delta\mathbf{g}_{SOO}$ is the correction due to the spin-other-orbit terms and includes higher-order contributions that arise from the relativistic interaction of the electron spin magnetic moment and the magnetic field induced by the orbital motion of other electrons. This correction to g_e is generally small in the systems treated in this thesis, and thus is often neglected [27]. Effectively, the shift depends on the spin-orbit coupling or crystal field effects. This may cause a more or less important deviation from the initial value of the Landé factor ($g_e \approx 2.0023193044$), *i.e.* systems including light impurities usually show only a small variation to this value as they usually have a small spin-orbit coupling whereas systems with transition metal impurities may

exhibit a large fluctuation due to a strong crystal field.

In terms of computation of this property [28], the response of the system to the external magnetic field perturbation is described through linear response theory. It involves determining the induced magnetization of the system in response to the applied magnetic field perturbation by computing the induced magnetic response current $\mathbf{j}(\mathbf{r})$ and the corresponding magnetic field $\mathbf{B}_{\text{ind}}(\mathbf{r})$ (obtained by the Biot-Savart law). This current is therefore necessary to properly describe the spin-orbit coupling $\Delta\mathbf{g}_{\text{SO}}$ which is the largest contribution to the $\overleftrightarrow{\text{g}}$-tensor components [23]:

$$\Delta\mathbf{g}_{\text{Zke}} = -\alpha^2 \text{g}_\text{e}(\text{T}^\uparrow - \text{T}^\downarrow) \tag{2.28}$$

$$\Delta\mathbf{g}_{\text{SO}} = \alpha(\text{g}_\text{e} - 1) \int \text{d}\mathbf{r}[\text{j}^\uparrow(\mathbf{r}) \times \nabla \text{V}^\uparrow_{\text{eff}}(\mathbf{r}) - \text{j}^\downarrow(\mathbf{r}) \times \nabla \text{V}^\downarrow_{\text{eff}}(\mathbf{r})] \tag{2.29}$$

$$\Delta\mathbf{g}_{\text{SOO}} = 2 \int \text{d}\mathbf{r}\mathbf{B}_{\text{ind}}\mathbf{r}[\rho^\uparrow(\mathbf{r}) - \rho^\downarrow(\mathbf{r})] \tag{2.30}$$

With T the unperturbed kinetic energy, V_{eff} an effective potential and ρ the electron probability density. In practice, the $\overleftrightarrow{\text{g}}$-tensor components can then be obtained as a sum of the three components, and g_e as in Eq. 2.27. The eigenvalues of g are obtained through a standard diagonalization procedure [29] and constitute the so called g-principal values. The latter are the diagonal values of the tensor when expressed in the basis of the eigenvectors. These represent the orientations of the principal axes.

2.2.2 Computation of the hyperfine coupling tensor A

As seen in Section 1.2.2, the hyperfine (hfi) coupling tensor $\overleftrightarrow{\text{A}}$ quantifies the interaction between the unpaired electrons and the nuclei carrying nuclear spin $\mathbf{I}$ in the system. This corresponds to the local electronic structure of the system:

$$\hat{\text{H}}_{\text{HF}} = \mathbf{S} \cdot \overleftrightarrow{\text{A}} \cdot \mathbf{I} \tag{2.31}$$

Similarly to the $\overleftrightarrow{\text{g}}$-tensor, it can be formally expressed with respect to both nuclear and electron spins:

$$\overleftrightarrow{\text{A}} = \left. \frac{\partial^2 \langle\Psi| \, |\hat{\text{H}}_{\text{eff}} \, |\Psi\rangle}{\partial\mathbf{I}\partial\mathbf{S}} \right|_{\mathbf{I}=\mathbf{S}=0}. \tag{2.32}$$

The $\overleftrightarrow{\text{A}}$ tensor can be decomposed into two parts, as is described in Section 1.2.2, the first is the isotropic interaction constant (or Fermi contact term), A_{iso}, which is proportional to the spin density at the nuclei, originating from s orbitals. It is associated with the overlap of the electronic wavefunction and the nuclear charge density at the atomic nuclei. The second part is the anisotropic or dipolar tensor $\overleftrightarrow{\text{A}}_{\text{aniso}}$ which introduces direction-dependent effects due to the interaction between the magnetic dipole moments of the unpaired electron and the nuclear

spins. It arises from the magnetic field generated by the unpaired electron at the location of the nuclei. The hfi tensor is computed, once the electron spin density is known, as

$$\overleftrightarrow{\mathrm{A}} = \mathrm{A_{iso}}\overleftrightarrow{1} + \overleftrightarrow{\mathrm{A}}_{\mathrm{aniso}} \tag{2.33}$$

where the components of both contributions to the tensor are obtained as [30]

$$\mathrm{A_{iso}} = \frac{2}{3}\mu_0 \mathrm{g_e}\mu_\mathrm{e}\mathrm{g_I}\mu_\mathrm{I}\rho_\mathrm{s}(\mathbf{R}) \tag{2.34}$$

$$\mathrm{A_{aniso}} = \frac{1}{4\pi}\mu_0 \mathrm{g_e}\mu_\mathrm{e}\mathrm{g_I}\mu_\mathrm{I}\int \mathrm{d}\mathbf{r}\rho_\mathrm{s}(\mathbf{r})\frac{3\cos^2\theta - 1}{2\mathrm{r}^3} \tag{2.35}$$

with μ_0 the permeability of vacuum ($4\pi \times 10^{-7}\mathrm{T}^2\mathrm{m}^3\mathrm{J}^{-1}$), $\mathrm{g_e}$ the free-electron g-factor, μ_e the Bohr magneton, $\mathrm{g_I}$ the gyromagnetic ratio of the nucleus (which is a well-tabulated constant for each element [31, 32]), μ_N the nuclear magneton, $\rho_\mathrm{s}(\mathbf{R})$ the electron spin density at nuclear site $\mathbf{R}$, equal to $[\rho^{\uparrow}(\mathbf{r}) - \rho^{\downarrow}(\mathbf{r})]$, and θ the angle between $\mathbf{r}$ and symmetry axes.

Defect centers in semiconductors generally have an isotropic or axial hfi interaction. In cases where the hfi interaction is anisotropic, *i.e.* it exhibits direction-dependent effects, the A-tensor is often expressed in terms of its parallel $\mathrm{A}_{\parallel}$ and perpendicular $\mathrm{A}_{\perp}$ components, defined as [33]

$$\mathrm{A}_{\parallel} = \mathrm{A_{iso}} + 2\mathrm{A_{aniso}} \tag{2.36}$$

$$\mathrm{A}_{\perp} = \mathrm{A_{iso}} - \mathrm{A_{aniso}} \tag{2.37}$$

The parallel component represents the hfi coupling constant along a specific reference axis based on the symmetry of the system, and the perpendicular component describes the interaction when the magnetic dipole moment is perpendicular to the reference axis.

On the computational side [28], the PAW reconstruction of the wavefunctions is sufficient and the all-electron density is simply computed as a reconstruction of the pseudo density at and around the nuclei. Its components provide information about the strength and anisotropy of the interaction between the unpaired electrons and the nearby atomic nuclei. Note that an accurate estimation of the hfi interaction relies on the spin density at the nuclei. Hence, to provide an accurate description of the core electron contribution to the density, which is crucial for estimating the Fermi contact, it could be necessary to take into account the relaxation of core electrons in response to the magnetization of valence electrons. However, for the specific cases explored in this thesis, focusing on N-related defects in Si, the extent of core relaxation for nitrogen atoms is minor, $\sim 10\%$ of the Fermi contact value obtained through the GIPAW method. Consequently, this relaxation effect was not incorporated into the results presented in Chapters 4 and 5.

2.3 Deep levels: calculation of Charge Transition Levels VS DLTS measurements

This work also focuses on characterising the electrical activity of deep-level defects within silicon. As will be explained in the following sections, by computing Charge Transition Levels

(CTLs) it becomes possible to provide direct comparison with activation energies obtained from DLTS measurements for deep levels in the band gap. CTLs play a fundamental role in understanding the electronic properties of defects in semiconductors. They determine the Fermi energy at which a defect can capture or emit a charge (and so, change its charge state), thereby influencing the electrical behaviour and optical properties of materials. Experimental techniques such as DLTS provide invaluable information about the energy levels of deep defects within the band gap which are often assigned to a subset of possible defects. However, assigning a spectroscopic signal to a specific defect has proven to be non-trivial. DFT calculations can be employed to determine the CTLs theoretically, providing insights into the structure of the defect responsible for a set of levels.

2.3.1 The standard DFT method

A naive way to compute the first ionisation potential (IP) would be as the energy difference between the valence band maximum (VBM) and highest occupied (HOMO) states. However, as mentioned in Section 2.1.1.4, the KS eigenvalues or states have no physical meaning and IP obtained from total energy differences between different charge states of the defect provide more accurate results when compared with experimental data. As such, the CTLs are defined as the Fermi energy at which two defect charge states have the same formation energy [34]. In simpler terms, a CTL represents the energy necessary for a transition to take place between two different charge states q and q' of a defect D. This transition can be expressed as

$$D^{q} \rightleftharpoons D^{q'} \pm e^{-}, \tag{2.38}$$

Considering the formation energy E_f^q of the charge state D^q as reference, the formation energy of the charge state $D^{q'}$ can be expressed as,

$$E_f^{q'} = E_f^q \pm \Delta(q/q') \pm \mu_e \tag{2.39}$$

In this equation, $\Delta(q/q')$ represents the energy exchanged during the transition between charge states q and q'. This difference accounts for the energy required to add or remove an electron from D^q, along with the energy released due to atomic relaxation. Fig. 2.4a shows a typical stability diagram for a defect in three charge states. In this representation, the CTLs act as frontiers delimiting the energy sections where one charge state is more stable (full line) than the others (dashed lines). The chemical potential of electrons, μ_e, is often written as the Fermi energy referred to the VBM, $\mu_e = \epsilon_{VBM} + \varepsilon_F$, where $\varepsilon_F \subset [0, \epsilon_{CBM} - \epsilon_{VBM}]$, where ϵ_{CBM} is the conduction band minimum. The CTL is then simply,

$$\varepsilon^{q/q'} = \pm\Delta(q/q') - \epsilon_{VBM}. \tag{2.40}$$

The CTLs can then be represented in an energy band diagram (Fig. 2.4b), with their positions relative the VBM and CBM. From equation 2.40, the CTLs can be calculated with DFT, where $\Delta(q/q')$ is evaluated as the difference in DFT total energies between the two relaxed defect structures at charge states q and q',

$$\Delta(q/q') = E^q_{DFT}\{\mathbf{R}^q\} - E^{q'}_{DFT}\{\mathbf{R}^{q'}\}, \tag{2.41}$$

where $\mathbf{R}^q$ denotes the ground state geometry at charge state q. The IP of the VBM, ϵ_{VBM}, is approximated by the corresponding Kohn-Sham eigenvalue in pristine silicon. Furthermore, the formation energy of charged defects (Eq. 2.39), is often corrected to mitigate the spurious electrostatic interaction between defect replicas [35]. This correction is usually evaluated by aligning the Density Of States (DOS) of the two defect states involved.

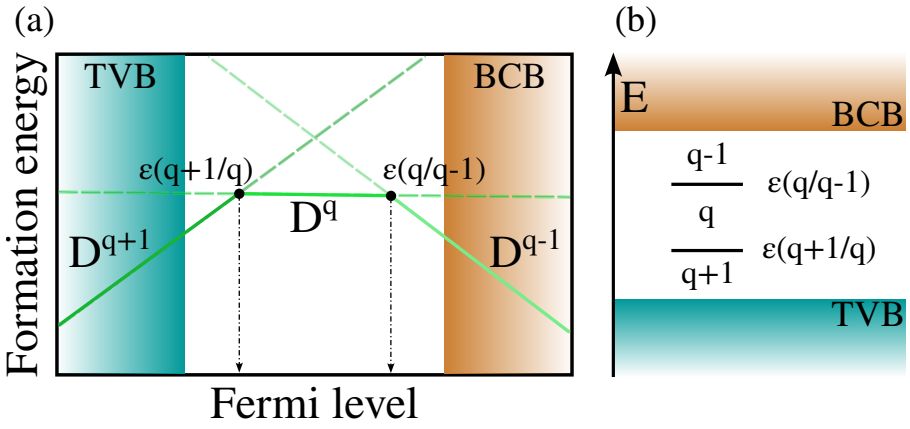

Fig. 2.4: (a) Formation energies for a defect D at different charge states q and q ± 1 as a function of the Fermi energy. (b) Corresponding charge transition levels on an energy band diagram.

2.3.2 The DFT+GW method

In order to circumvent the self-interaction contribution, and so the band gap problem in standard *ab initio* DFT calculations, a more refined approach is adopted in this thesis to compute formation energies of defects. It relies on the LDA+GW method [36], which introduces quasi-particles (QP), *i.e.* many-body corrections as a pertubation to DFT , to determine accurate IP and electronic affinities (EA) [37,38]. This method determines that the calculation of formation energies for different charge states of any defect D is accurate and reliable with respect to the reference energy E_f^q, in cases where the defect has unoccupied states within the band gap at charge state q. The formation energy in Eq. 2.39 then becomes, for charge state q'

$$E_f^{q'} = E_f^q + EA(\mathbf{g}^q,q) + \Delta E_{relax}^{q'} - \mu_e \tag{2.42}$$

Where $\mathbf{g}^q$ is the equilibrium ionic geometry at charge states q, $EA(\mathbf{g}^q,q)$ the first electronic affinity at this charge state and $\Delta E_{relax}^{q'}$ the relaxation energy given to the lattice. This approach is illustrated by a simple diagram in Fig. 2.5, which shows the path to compute the CTLs using the DFT + GW method.

In this framework, the CTL in Eq. 2.40 is redefined as

$$\varepsilon^{q/q'} = \pm\Delta(q/q') - IP_{VBM}. \tag{2.43}$$

Where ϵ_{VBM} in equation 2.40 becomes the QP energy of pristine Si $\mathrm{IP}_{\mathrm{VBM}}$. the difference $\Delta(\mathrm{q}/\mathrm{q}')$ is then determined as an IP/EA, evaluated as a QP energy at charge state q, minus/plus a relaxation energy. This relaxation energy is evaluated as a DFT total energy difference between the relaxed structures at q and q', evaluated for the final q' charge state. The $\Delta(\mathrm{q}/\mathrm{q}')$ difference is thus evaluated as,

$$\Delta(\mathrm{q}/\mathrm{q}') = \mathrm{EA/IP}^{\mathrm{q}} \pm \left[\mathrm{E}^{\mathrm{q}'}_{\mathrm{DFT}}\{\mathbf{R}^{\mathrm{q}'}\} - \mathrm{E}^{\mathrm{q}'}_{\mathrm{DFT}}\{\mathbf{R}^{\mathrm{q}}\}\right]. \tag{2.44}$$

Finally, it is notable from Fig. 2.5 that there are four different paths that can be used to compute the CTLs with this method. This characteristic leads to a more robust assessment of the reliability of these calculations as it allows to verify the consistency of the calculations with respect to each different path.

By including these corrections, the quasiparticle energies are substantially improved, leading to more accurate predictions of electronic band structures, band gaps, and electronic and optical properties of materials. However, this method is quite expensive, as the procedure for solving the QP equation requires significant computational resources. Thus, calculations of CTLs are still often performed at the DFT level only, despite the known failings it may exhibit. In the following sections of this thesis, thermodynamic CTLs are computed at both DFT and DFT+GW levels. The practical details of these calculations (softwares, calculation parameters) are descibed in Chapter 3.

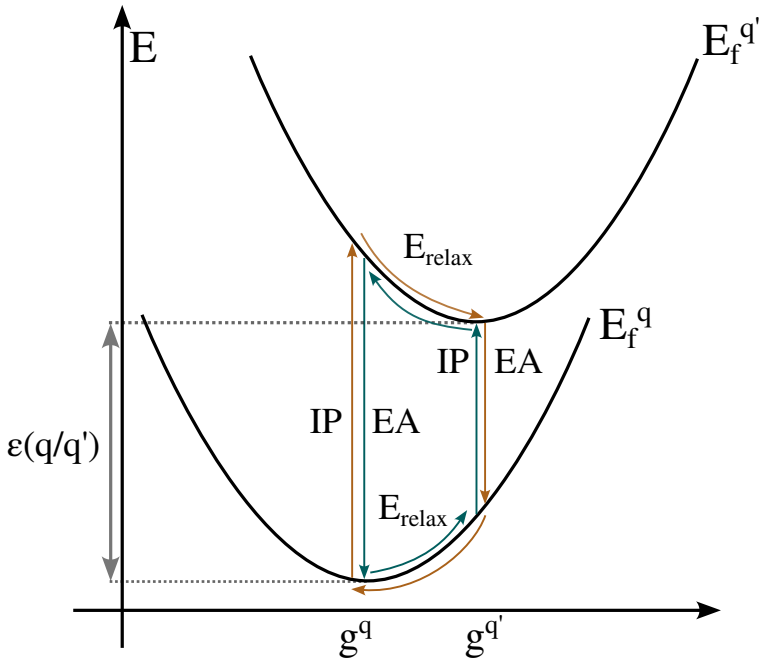

Fig. 2.5: Schematic representation of the different paths to compute the Charge Transition Level between charge states q and q' using the combined DFT + GW formalism.

Bibliography

[1] D. S. Sholl and J. A. Steckel. *Density Functional Theory: A Practical Introduction*. John Wiley & Sons, Ltd, 2009.

[2] A. Szabo and N. S. Ostlund. *Modern Quantum Chemistry: Introduction to Advanced Electronic Structure Theory*. Dover Publications, Inc., 1982.

[3] J. Toulouse. *Introduction to density-functional theory*, 2019. Available at: https://www.lct.jussieu.fr/?page_id=515.

[4] R. M. Martin. *Electronic Structure: Basic Theory and Practical Methods*. Cambridge University Press, 2004.

[5] P. Hohenberg and W. Kohn. Inhomogeneous electron gas. *Physical Review*, 136(3B):B864, 1964.

[6] W. Kohn and L. J. Sham. Self-consistent equations including exchange and correlation effects. *Physical Review*, 140(4A):A1133, 1965.

[7] J. P. Perdew and Y. Wang. Accurate and simple analytic representation of the electron-gas correlation energy. *Physical Review B*, 45(23):13244, 1992.

[8] J. P. Perdew, K. Burke, and M. Ernzerhof. Generalized gradient approximation made simple. *Physical Review letters*, 77(18):3865, 1996.

[9] A. D. Becke. A new mixing of hartree–fock and local density-functional theories. *The Journal of Chemical Physics*, 98(2):1372–1377, 1993.

[10] J. Tao, J. P. Perdew, V. N. Staroverov, and G. E. Scuseria. Climbing the density functional ladder: Nonempirical meta–generalized gradient approximation designed for molecules and solids. *Physical Review Letters*, 91(14):146401, 2003.

[11] F. Bloch. Über die quantenmechanik der elektronen in kristallgittern. *Zeitschrift für Physik*, 52(7-8):555–600, 1929.

[12] N. W. Ashcroft and N. D. Mermin. *Solid State Physics*. Saunders College Publishing, 1976.

[13] H. J. Monkhorst and J. D. Pack. Special points for Brillouin-zone integrations. *Physical Review B*, 13(12):5188–5192, June 1976.

[14] J. D. Pack and H. J. Monkhorst. "special points for brillouin-zone integrations"—a reply. *Physical Review B*, 16:1748–1749, Aug 1977.

[15] C. J. Pickard and F. Mauri. All-electron magnetic response with pseudopotentials: NMR chemical shifts. *Physical Review B*, 63:245101, May 2001.

[16] The pseudopotentials files used for calculations are `Si.pbe-tm-new-gipaw-dc.UPF`, `P.pbe-tm-new-gipaw-dc.UPF` and `N.pbe-tm-new-gipaw-dc.UPF` available online from D. Ceresoli's repository `https://sites.google.com/site/dceresoli/`.

[17] J. P. Perdew. Density functional theory and the band gap problem. *International Journal of Quantum Chemistry*, 28(S19):497–523, 1985.

[18] L. Hedin. New method for calculating the one-particle green's function with application to the electron-gas problem. *Physical Review*, 139(3A):A796, 1965.

[19] H. Jónsson, G. Mills, and K. W. Jacobsen. Nudged elastic band method for finding minimum energy paths of transitions. In *Classical and Quantum Dynamics in Condensed Phase Simulations*, pages 385–404. World Scientific, 1998.

[20] C. J. Pickard and F. Mauri. First-principles theory of the EPR g tensor in solids: Defects in quartz. *Physical Review Letters*, 88:086403, Feb 2002.

[21] P. E. Blöchl. Projector augmented-wave method. *Physical Review B*, 50(24):17953, 1994.

[22] G. Schreckenbach and T. Ziegler. Calculation of the g-tensor of electron paramagnetic resonance spectroscopy using gauge-including atomic orbitals and density functional theory. *The Journal of Physical Chemistry A*, 101(18):3388–3399, 1997.

[23] R. Declerck, V. Van Speybroeck, and M. Waroquier. First-principles calculation of the EPR g tensor in extended periodic systems. *Physical Review B*, 73(11):115113, 2006.

[24] A. Dalgarno, A. L. Stewart, and D. R. Bates. On the perturbation theory of small disturbances. *Proceedings of the Royal Society of London. Series A. Mathematical and Physical Sciences*, 238(1213):269–275, 1956.

[25] A. Dalgarno and A. L. Stewart. A perturbation calculation of properties of the 2 pπ state of HeH^{2+}. *Proceedings of the Royal Society of London. Series A. Mathematical and Physical Sciences*, 240(1221):274–283, 1957.

[26] A. Dalgarno, A. L. Stewart, and D. R. Bates. A perturbation calculation of properties of the helium iso-electronic sequence. *Proceedings of the Royal Society of London. Series A. Mathematical and Physical Sciences*, 247(1249):245–259, 1958.

[27] D. Ceresoli, U. Gerstmann, A. P. Seitsonen, and F. Mauri. First-principles theory of orbital magnetization. *Physical Review B*, 81(6):060409, 2010.

[28] P. Giannozzi, O. Andreussi, T. Brumme, O. Bunau, M. B. Nardelli, M. Calandra, R. Car, C. Cavazzoni, D. Ceresoli, M. Cococcioni, N. Colonna, I. Carnimeo, A. Dal Corso, De Gironcoli S., Delugas P., DiStasio Jr R. A., Ferretti A., Floris A., Fratesi G., Fugallo G., Gebauer R., Gerstmann U., Giustino F., Gorni T., Jia J., Kawamura M., Ko H.-Y., Kokalj A., Küçükbenli E., Lazzeri M., Marsili M., Marzari N., Mauri F., Nguyen N. L., Nguyen H.-V., Otero de-la Roza A., Paulatto L., Poncé S., Rocca D., Sabatini R., Santra B., Schlipf M., Seitsonen A. P., Smogunov A., Timrov I., Thonhauser T., Umari P., Vast N., Wu X., and Baroni S. Advanced capabilities for materials modelling with quantum ESPRESSO. *Journal of Physics: Condensed Matter*, 29(46):465901, 2017.

[29] J. A. Weil and J. R. Bolton. Zeeman energy (g) anisotropy. In *Electron Paramagnetic Resonance*, chapter 4, pages 85–117. John Wiley & Sons, Ltd, 2006.

[30] M. S. Bahramy, M. H. F. Sluiter, and Y. Kawazoe. Pseudopotential hyperfine calculations through perturbative core-level polarization. *Physical Review B*, 76:035124, Jul 2007.

[31] Stoll S. Easyspin nuclear isotope database, 2006. https://easyspin.org/documentation/isotopetable.html [Accessed: 01/02/2024].

[32] N. J. Stone. Table of nuclear magnetic dipole and electric quadrupole moments. *Atomic Data and Nuclear Data Tables*, 90(1):75–176, 2005.

[33] C. G. Van de Walle and P. E. Blöchl. First-principles calculations of hyperfine parameters. *Physical Review B*, 47(8):4244, 1993.

[34] C. Freysoldt, B. Grabowski, T. Hickel, J. Neugebauer, G. Kresse, A. Janotti, and C. G. Van de Walle. First-principles calculations for point defects in solids. *Reviews of Modern Physics*, 86:253–305, Mar 2014.

[35] R. M. Nieminen. Supercell methods for defect calculations. *Theory of Defects in Semiconductors*, pages 29–68, 2007.

[36] P. Rinke, A. Janotti, M. Scheffler, and C. G. Van de Walle. Defect formation energies without the band-gap problem: Combining density-functional theory and the GW approach for the silicon self-interstitial. *Physical Review Letters*, 102(2):026402, 2009.

[37] L. Hedin and S. Lundqvist. Effects of electron-electron and electron-phonon interactions on the one-electron states of solids. *Solid State Physics*, 23:1–181, 1969.

[38] M. Van Setten, F. Caruso, and P. Rinke. GW100. Available at: https://gw100.wordpress.com/.

Chapter 3

Method validation: the case of the phosphorus-vacancy complex in Si

The accuracy of the methods discussed in the previous chapter for characterising defects properties is validated through a convergence study on a well-known system, the phosphorus-vacancy complex in silicon, *i.e.* the so-called E-center. In Section 3.1, a review of the properties of this center is provided. The practical aspects of the methodology are presented (Section 3.2) and studies of the convergence of total energy per atom (Section 3.3), hyperfine structure parameter (Section 3.4) and $\overleftrightarrow{g}$-tensor (Section 3.5) with respect to the size of the simulated supercell, number of k-points to sample the Brillouin zone and kinetic energy cutoff are carried out. Finally, the extensive experimental and theoretical literature on this defect center serves as a good benchmark to assess the accuracy of the present method to compute electronic structures and related properties, with respect to both EPR spectroscopy measurements and previous theoretical works (Section 3.6).

3.1 Overview of the phosphorus-vacancy complex in Si

The *E*-center is one of the predominant defects in n-type P-doped silicon and can be formed by electron irradiation [1–3]. It corresponds to a phosphorus impurity next to a silicon vacancy and was first charaterised by EPR measurements of irradiated Si [1, 2]. These studies revealed that the ground state configuration of the neutral *E*-center PV^0 adopts a pairing (P) geometry. This structure is characterised by one of the three $S_i - S_i$ interatomic distances, between the three silicon atoms neighboring the vacancy, being shorter than the other two (Fig. 3.1a). Additionally, stress measurements unveiled the presence of three degenerate ground state geometries separated by an energy barrier of 60 – 70 meV. Subsequent optical absorption [3] studies on PV, AsV, and SbV indicated a different sense of the ground state Jahn-Teller distortion. In this resonant (R) configuration, one of the $S_i - S_i$ distances is longer than the other two. A simple single-electron molecular orbital model was then proposed to explain the reversal of the distortion when changing charge state, as well as the existence of degenerate ground states (Fig. 3.1b). According to this model, the Potential Energy Surface (PES) is predicted to take the shape of a Mexican hat. For PV^0, the PES exhibits three degenerate P configurations as ground state, and three degenerate R configurations as transition states. Within this model, the energy barrier between equivalent ground states corresponds to the energy difference between pairing and resonant configurations. Furthermore, at the top of the PES lies the higher energy maximum breathing mode configuration $\mathcal{B}$, which corresponds to the high symmetry structure, before Jahn-Teller distortion.

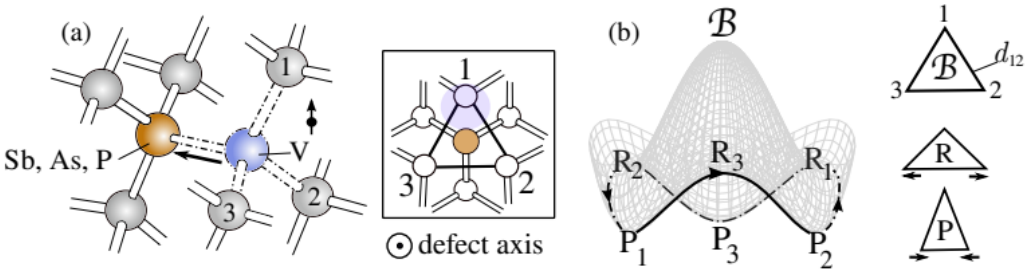

Fig. 3.1: (a) The silicon *E*-center and its projection along the vacancy-dopant axis. The probability density for the unpaired electron at neutral charge state is also shown. (b) Watkins *et al.* model for the *E*-center potential energy surface at the neutral charge state. Three geometries are distinguished depending on the relative interatomic distances between atoms 1, 2 and 3: the symmetric breathing configuration ($\mathcal{B}$), the pairing configuration (P), and the resonant bond configuration (R). P_i and R_i denote the pairing and resonant geometries with unpaired distances $d_{jk} < d_{ij} = d_{ik}$ and $d_{jk} > d_{ij} = d_{ik}$, respectively. Figure by [4], reprinted with permission.

Since the experimental identification of the silicon *E*-center, there has been some controversy among theoreticians concerning the ground state configuration and subsequently the ordering between P and R states [5–8]. However, these works only relied on total energies to ascertain the ground state configuration without investigating the PES. Most recently, this task was carried out [4, 9] and results in agreement with experimental observations were achieved.

Nevertheless, there still was a lack of evidence allowing to unequivocally associate a defect structure of PV to the measured EPR spectra as it was uncommon for studies to compute EPR parameters to be **directly** compared with EPR spectroscopy. Due to the difficulties in calculating the $\overleftrightarrow{g}$-tensor, the hfi parameter was usually provided [10], with values in good agreement with experimental data. This parameter alone however is not sufficient to provide unambiguous attribution of this defect structure and calculations of both $\overleftrightarrow{g}$ and $\overleftrightarrow{A}$ tensors were later reported [8], showing excellent concordance with EPR measurements. The present study relies on the abundance of both experimental and theoretical data on PV to test the accuracy of the methods adopted in this thesis to compute ground state density and related properties based on DFT. Convergence tests of DFT calculation parameters for the well-known *E*-center in silicon have been carried out to establish the parameters necessary to obtain accurate and reliable results.

3.2 Methodology

All calculations were carried out using the Quantum-ESPRESSO package for electronic structure calculations [11,12]. The PBE XC functional [13], together with norm-conserving Troullier–Martins pseudopotentials with GIPAW reconstruction [14,15] were used. The hyperfine $\overleftrightarrow{A}$ and $\overleftrightarrow{g}$ coupling tensors of the paramagnetic defect were computed using the QE-GIPAW module of the QE package [12,16].
The defect at neutral charge state was embedded in different silicon cells. The initial structure was determined based on symmetry considerations, as obtained in [4,9]. In the present study, calculations were applied only to the pairing configuration of the defect, which was optimized maintaining a constant lattice parameter. The value of this parameter was set to the estimated one for pristine silicon for each SC, with cell sides of $a_{64} = 10.6$ Å, $a_{216} = 16.4$ Å and $a_{512} = 21.7$ Å for the $2 \times 2 \times 2$ (64 atoms without defect), $3 \times 3 \times 3$ (216 atoms without defect) and $4 \times 4 \times 4$ (512 atoms without defect) respectively. A Broyden-Fletcher-Goldfarb-Shanno (BFGS) algorithm [17,18] was used to find equilibrium structures of the defect, with a convergence threshold on forces set to 0.026 eV/Å. The convergence threshold for self-consistency was set to 1.36×10^{-7} eV.

Table 3.1 records the calculation parameters used for this convergence study, depending on the property of interest and the convergence criterion. The range of variation of the kinetic energy cutoff, between 20 and 90 Ry, was chosen to match the values reported and commonly used for different elements [19]. For the SC size and k-point mesh, the range of variation for checking convergence was limited to computationally achievable values. The BZ was sampled with grids of k-points varying from the Γ point only, to $2 \times 2 \times 2$ (8 k-points), $3 \times 3 \times 3$ (27 k-points) and $4 \times 4 \times 4$ (64 k-points) grids. These were used to integrate different SC with 64, 216 or 512 atoms.
Reasonably affordable calculations are currently limited, especially for $\overleftrightarrow{g}$ tensor calculations, to sampling the BZ with a $3 \times 3 \times 3$ k-points grid on a 512 atoms cell. Beyond this, the calculation cost becomes prohibitively large. Furthermore, The GIPAW method can face chal-

lenges when calculating EPR parameters in materials with defects, particularly in silicon. The presence of defects introduces additional complexities and can lead to instabilities in the calculations (Section 2.2), rendering them highly challenging for larger systems with finer grids.

Tab. 3.1: Calculation parameters for convergence studies. The properties relevant for checking the convergence include the total energy of the system and both EPR parameters (hyperfine $\overleftrightarrow{A}$ and $\overleftrightarrow{g}$ coupling tensors). Their convergence is checked with respect to three DFT calculation parameters: size of the supercell (SC) in number of atoms in the pristine Si cell, k-point grid for sampling of the Brillouin zone and kinetic energy cutoff (E_{cut}) in Ry.

Property	Parameters	Convergence with respect to SC size	Convergence with respect to k-point mesh	Convergence with respect to E_{cut} (Ry)
E_{tot}	SC size	64 to 512 atoms	216 atoms	216 atoms
	K-point mesh	Γ	Γ to $4 \times 4 \times 4$	Γ
	E_{cut} (Ry)	50	50	20 to 90
EPR parameters	SC size	64 to 512 atoms	216 atoms	216 atoms
	K-point mesh	$2 \times 2 \times 2$	Γ to $4 \times 4 \times 4$	$2 \times 2 \times 2$
	E_{cut} (Ry)	50	50	20 to 90

3.3 Total energy per atom convergence

The total energy is directly linked with the ground state electronic structure, which provides critical information about the stable configuration of the system and other ground state properties. Converged total energies ensure that the electronic structure is well described, leading to reliable and accurate predictions of other properties, (*i.e.* band gaps, vibrational frequencies, magnetic moments). Moreover, as detailed in Section 2.3, CTLs are often computed as total energy differences between ground states of multiple charge states, highlighting the importance to obtain precise and dependable energies. In the case of the *E*-center, comparing the total energies of different structures (pairing, resonant and breathing) can determine the most stable configuration, which leads to a proper understanding of the dynamics between them.

As illustrated in Fig. 3.2b, the total energy per atom is rather weakly dependent on the k-point grid, as it is already converged to within 14 meV at Γ. Even more accurate values could be obtained by integrating over a $2 \times 2 \times 2$, however this would drastically increase the calculation cost which scales linearly with the number of k-points.

On the other hand, the total energy per atom is much more impacted by the size of the simulation cell. In particular, Fig. 3.2a does not show a clear convergence even for a large 512 atoms cell. However, as stated previously, current computational resources limit the size

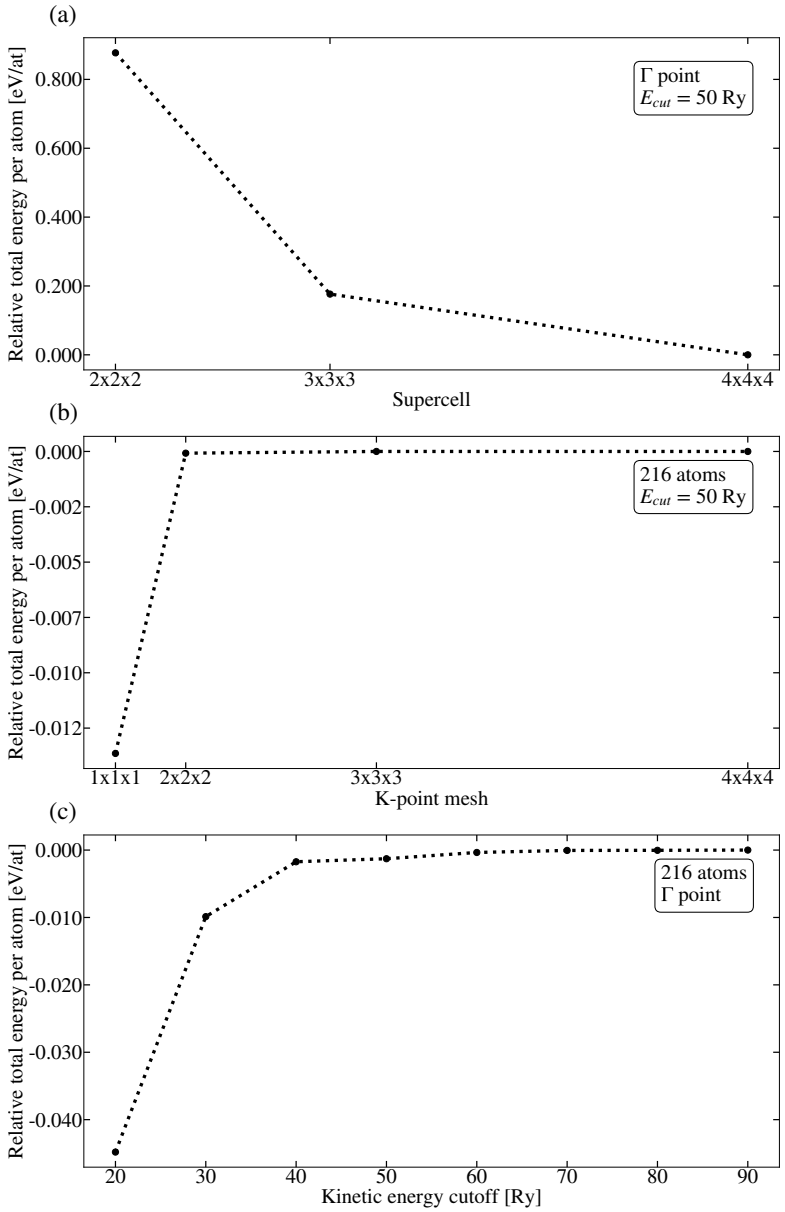

Fig. 3.2: Convergence of the total energy per atom with respect to: (a) supercell size. The format of the cells presented 'ncx × ncy × ncz' corresponds to the number of replicas of the unit cell nc in each x, y, or z direction of space. (b) K-points grid used to sample the Brillouin zone. Each mesh is displayed in the format defined by the Monkhorst–Pack scheme, 'nkx × nky × nkz' where each component is the number nk of k-points used in each x, y, or z direction. (c) kinetic energy cutoff E_{cut}. The lines are a guide to the eye.

of the SC, especially for calculations of EPR parameters which are the limiting factor for the parameters chosen, as will be discussed below.

Finally, the convergence with respect to E_{cut} shown in Fig. 3.2c follows a more typical trend and shows a clear convergence within 1.3 meV for 50 Ry.

3.4 Hyperfine structure parameter convergence

As one of the main properties of interest of this thesis, it is necessary to test the convergence of the hfi coupling parameter $\overleftrightarrow{A}$ in order to obtain the optimal calculation parameters ensuring the most accurate results. As stated in Sections 1.2.2 and 2.2, the hfi structure tensor is composed by the Fermi contact constant A_{iso} and the hfi dipolar tensor $\overleftrightarrow{A}_{dip}$, that can be computed for each atom in the system. Since the hfi tensor depends on the unpaired spin density, the most relevant contributions comes from the atoms close to the defect itself. Those values are compared directly with experimental data (*e.g.* hfi splittings) extracted from EPR measurements which generally have a resolution high enough to correctly characterise the nearest neighbor shell (and more rarely also next nearest neighbors shell) around the defect. Fig. 3.3 presents the same convergence checks as those for the total energy per atom. Values are reported for the P impurity and the three Si around the vacancy, two of which have the same electronic environment and so, are equivalent. For each test all atoms exhibit similar behaviour, converging at the same rate with respect to the input parameter.

In the case of the convergence with respect to the SC size (Fig. 3.3a), the hfi constant is

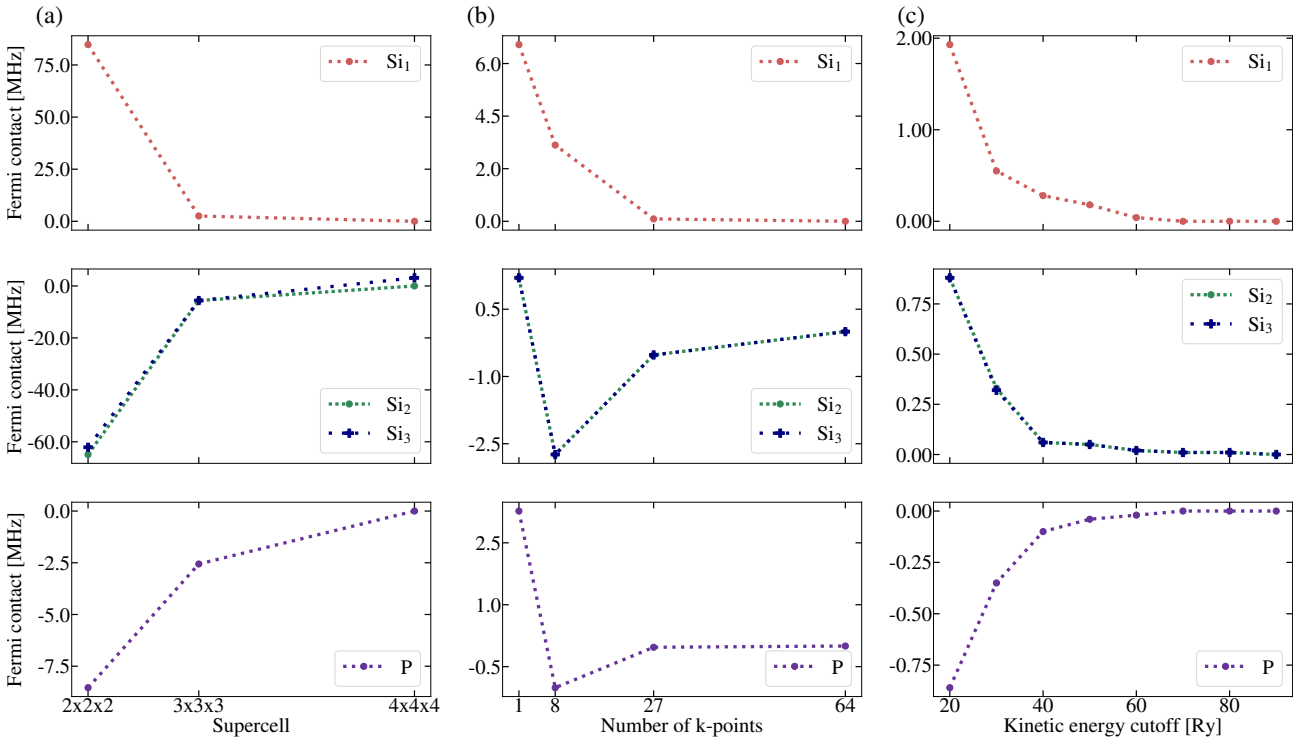

Fig. 3.3: Convergence of the Fermi contact A_{iso} with respect to: (a) supercell size. The format of the cells presented 'ncx × ncy × ncz' corresponds to the number of replicas of the unit cell nc in each x, y, or z direction of space. (b) Number of k-points used to sample the Brillouin zone, as defined by the Monkhorst–Pack scheme. (c) Kinetic energy cutoff E_{cut}. The tests were performed for each most relevant contributions of the *E*-center EPR spectrum, the phosphorus impurity (P) and the three silicon atoms (Si_{1-3}) around the vacancy, as shown in Fig. 3.1. The lines are a guide to the eye.

converged within 3 and 10 MHz for the Si_1 and $Si_{2,3}$ atoms respectively when modelling using the 216 atoms cell. For the P impurity however, there is no clear convergence achieved with the supercells tested. This tendency may be explained by it being a deep well of potential compared to the Si atoms. In that respect, as P introduces highly localised electronic states, the challenges of DFT (detailed in Section 2.1.2.5) are exacerbated and may lead to larger inaccuracies in the magnetic properties of the system. This effect is however not so significant and the SC size still provides reliable results for the hfi parameter, as the Fermi contact difference for this atom between 216 and 512 atoms is 3 MHz only, comparable to the level of convergence for the Si atoms at 216 atoms. It is also interesting to note that the values for Si_2 and Si_3 (which are supposed to be identical since they are equivalent) are no longer the same in the 512 atoms cell. This is due to some numerical inaccuracies of the calculations (*i.e.* notably due to computational limitations), but the small deviation of ~ 3 MHz is within the expected inaccuracy estimates of the GIPAW method [20, 21].

The number of k-points used to sample the BZ is rather significant for convergence of the Fermi contact, as indicated by Fig. 3.3b, and for all atoms considered the calculations are satisfyingly converged for a $3 \times 3 \times 3$ mesh (27 k-points), with convergence within 0.1, 0.5 and 0.05 MHz for Si_1, $Si_{2,3}$ and P respectively.

The dependence of the hfi parameter on the cutoff energy is weaker than for the other parameters, of the order of a couple of MHz at most, and all systems are converged to within 0.01 MHz at 50 Ry (Fig. 3.3c).

The same trends are observed for the main values of the hfi coupling tensor (A_1, A_2, A_3), leading to the same set of calculation parameters.

3.5 g-tensor parameter convergence

Finally, the effect of the convergence of the $\overleftrightarrow{g}$-tensor isovalue g_{iso} and main values (g_1, g_2, g_3) is investigated and plotted in Fig. 3.4. Calculations of $\overleftrightarrow{g}$-tensor are significantly more costly and heavy compared to the previous properties. This implies that the parameters set in this section are likely limiting in terms of computational cost and will define the framework used all throughout this work.

The variation of the g-value is somewhat similar to what is observed for the Fermi contact, and similar parameters can be extracted from Figs. 3.4a, b and c. In particular, concerning the g-shift convergence with respect to the kinetic energy cutoff (Fig. 3.4c), as for previous checks, this parameter presents the weakest influence, *i.e.* a few hundred ppm at most which is small as compared to previous estimations of the inaccuracy (vs experiment) of the GIPAW method $\sim$ 1000−3000 ppm [20, 21]. In particular for example as found ($\sim$ 1000 ppm) in recent calculations carried out for the positively charged silicon vacancy V^+ in silicon (G1 center) [22]. Furthermore, all four values are exceedingly well converged, within 15 ppm at 50 Ry.

On the other hand, there is no clear convergence of the g-shift with respect to the SC, as shown in Fig. 3.4a, indicating that a larger 1000 atoms cell is required to obtain fully converged calculations when using just a Γ point sampling. However $\overleftrightarrow{g}$-tensor calculation time increases tremendously when increasing the SC size (*i.e.*, the calculation for one k-point in the 512 SC is

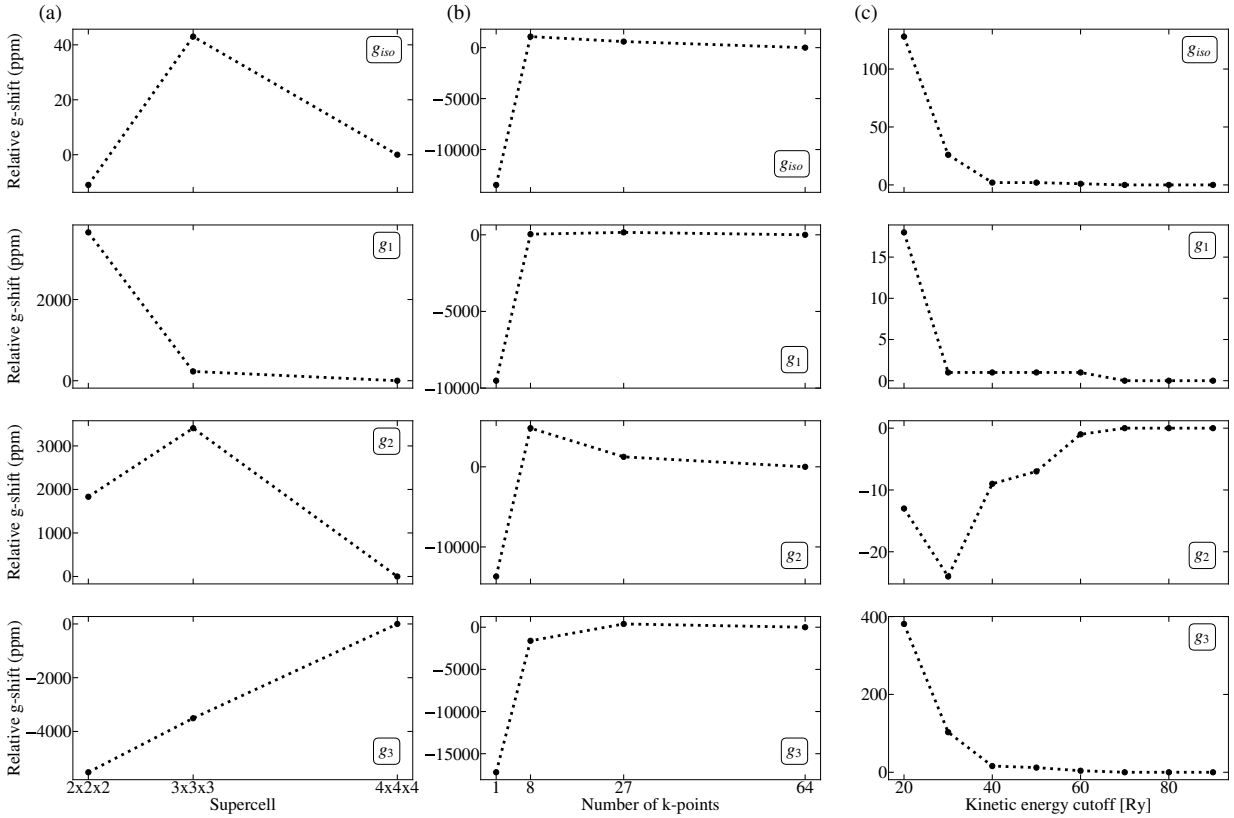

Fig. 3.4: Convergence of the main (g_1, g_2, g_3) and isotropic (g_{iso}) values of the $\overleftrightarrow{g}$-tensor with respect to: (a) supercell size. The format of the cells presented 'ncx × ncy × ncz' corresponds to the number of replicas of the unit cell nc in each x, y, or z direction of space. (b) Number of k-points used to sample the Brillouin zone, as defined by the Monkhorst–Pack scheme. (c) Kinetic energy cutoff E_{cut}. The lines are a guide to the eye.

$\sim$ 12 times longer than in the 216 SC). Therefore, further increasing the SC size is not a viable possibility considering current computational limitations. The observed deviations for the 216 atoms SC are 40, 230, $\sim$ 3400 and $\sim$ 3500 ppm for g_{iso}, g_1, g_2 and g_3 respectively which are, in the largest divergences, still in similar order of magnitude as the inaccuracy of the method.

Finally, the case of the convergence with respect to the number of k-points used to sample the BZ is presented in Fig. 3.4b. Values for g_{iso}, g_1 and g_3 appear well converged for a $3\times3\times3$ mesh corresponding to 27 k-points within a few hundred ppm. Although not as well converged, the deviation for g_2 is nonetheless satisfactory, within $\sim$ 1200 ppm for this grid of k-points.

3.6 Comparison with experiments

The results of $\overleftrightarrow{g}$ and $\overleftrightarrow{A}$ tensors computed using the calculation parameters identified above, *i.e.* integrating a 216 atoms SC over a $3\times3\times3$ k-point mesh with an E_{cut} of 50 Ry, are included in Table 3.2 and compared with data from EPR measurements and previous calculations.

We obtain excellent agreement with the values reported by Watkins *et al.* [1,2] (denoted by

Tab. 3.2: EPR parameters for neutral PV in pairing configuration. The estimated $\overleftrightarrow{\mathrm{g}}$ and the hyperfine $\overleftrightarrow{\mathrm{A}}$ tensors for the P impurity (P) and the three Si atoms around the vacancy (Si_{1-3}) are shown (tw) and compared with EPR data of the *E*-center [1,2], denoted by †. Previous calculations for PV are also included, denoted by ∗. A similar DFT method was used in all cases, but different calculation parameters and functionals (PBE or HSE) were used [8,10].

	$\overleftrightarrow{\mathrm{g}}$			$\overleftrightarrow{\mathrm{A}}$ ($^{29}Si_1$) (MHz)				$\overleftrightarrow{\mathrm{A}}$ ($^{29}Si_{2,3}$) (MHz)				$\overleftrightarrow{\mathrm{A}}$ (P) (MHz)			
Ref.	$\mathbf{g_1}$	$\mathbf{g_2}$	$\mathbf{g_3}$	$\mathbf{A_1}$	$\mathbf{A_2}$	$\mathbf{A_3}$	$\mathbf{A_{iso}}$	$\mathbf{A_1}$	$\mathbf{A_2}$	$\mathbf{A_3}$	$\mathbf{A_{iso}}$	$\mathbf{A_1}$	$\mathbf{A_2}$	$\mathbf{A_3}$	$\mathbf{A_{iso}}$
tw	1.9997	2.0123	2.0085	–476.2	–322.3	–322.1	–373.5	–49.8	–43.9	–42.4	–45.4	32.7	27.6	27.5	29.3
[10] (PBE)*	-	-	-	–388.6	–244.3	–244.1	-	–40.7	–35.1	–33.6	-	29.9	25.4	25.3	-
[10] (HSE)*	-	-	-	–429.9	–251.3	–250.8	-	–31.5	–27.2	–24.9	-	35.5	30.7	30.0	-
[8]*	1.9996	2.0128	2.0079	–451	–300	–300	–350	-	-	-	-	-	-	-	–40,–42
[1,2]†	2.0005	2.0112	2.0096	449.7	295.3	295.3	–346.9	-	-	-	–37.2	31.7	26.2	25.9	27.9

* Theoretical method
† Experimental reference

† in Table 3.2), within ~ 1000 ppm for all three main components of the $\overleftrightarrow{g}$-tensor. The discrepancy between calculations and measurements is within the expected imprecision estimates of the GIPAW method [20–22] which further validates its accuracy. For the hfi tensor of Si_1, the correct behaviour of the interaction is captured since the expected axial symmetry is shown, with $A_1 = A_{\parallel}$ and $A_2 = A_3 = A_{\perp}$. The presented values are within 5 % of the experimental $A_{\parallel}$ and within 10 % for $A_{\perp}$. Only the isotropic contribution to the hfi structure for the two equivalent atoms Si_2, Si_3 was reported [1, 2], which corresponds to the trace of the calculated $\overleftrightarrow{A}$ tensor, $A_{iso} = (A_{xx} + A_{yy} + A_{zz})/3$ (Section 1.2.2). This contribution is the least accurate value as a 22 % difference with the experimental value is obtained. Finally, results for the P impurity are close to experiments, within 3 % for A_1, 5 % for A_2 and 6 % for A_3.

We also compare the results of the present study with previous computational studies of EPR parameters for PV (denoted by $*$ in Table 3.2). These works employ the same DFT with SC and pw basis sets frameworks, but used different calculation parameters, allowing to validate the consistency and robustness of the method. Ref. [10] performed both GGA (PBE in the table) and hybrid (HSE in the table) DFT calculations, with PAW pseudopotentials on a 512 atoms SC. They sampled the BZ with a $2 \times 2 \times 2$ grid (PBE) or at the Γ point only (HSE), and used a kinetic energy cutoff of ≈ 30 Ry to obtain the hyperfine signature of the defect. The presented results align with their PBE data, any observed deviations likely attributable to differences in accuracy arising from the use of different parameters and pseudopotential. The HSE results at Γ provide an improvement over their PBE results only for the Si_1 atom. In this case however they still show worse agreement with experiments than the results obtained in this work, likely due to the sampling of the BZ which is not enough to correctly describe the behaviour of the electronic states throughout the cell. Ref. [8] performed calculations of both $\overleftrightarrow{g}$ and $\overleftrightarrow{A}$ tensor through *ab initio* DFT calculations with the PBE functional on a 216 atoms supercell. They used norm-conserving pseudopotentials with scalar-relativistic correction for the Si only, a 30 Ry cutoff and sampled the BZ with a $3 \times 3 \times 3$ for the hfi structure and $6 \times 6 \times 6$ for the $\overleftrightarrow{g}$-tensor. The $\overleftrightarrow{g}$-tensor given in this study is almost identical to theirs even though the k-point mesh is much more dense in their case, suggesting that the $3 \times 3 \times 3$ grid is converged enough. Moreover, the values for the hfi coupling for Si_1 are close as well. In this case, the small difference between both sets of hfi values (≈ 20 MHz) may be due to the use of relativistic corrections in the pseudopotentials for both Si and P in this work [15] since this is the only actual difference between the two calculations.

Since the presented results are consistent with both previous calculations, particularly those performed in [8], and experiments, the adopted methodological approach proves reliable to predict the electronic structure and spectroscopic properties for other systems.

Bibliography

[1] G. D. Watkins and J. W. Corbett. Electron paramagnetic resonance of defects in irradiated silicon. *Discussions of the Faraday Society*, 31:86–95, 1961.

[2] G. D. Watkins and J. W. Corbett. Defects in irradiated silicon: Electron paramagnetic resonance and electron-nuclear double resonance of the si-E center. *Physical Review*, 134(5A):A1359, 1964.

[3] G. D. Watkins. Optical properties of group-V atom-vacancy pairs in silicon. *Radiation Effects and Defects in Solids*, 111(1-2):487–500, 1989.

[4] G. Herrero-Saboya. *Defects in silicon: revisiting theoretical frameworks to guide ab initio characterization*. PhD thesis, Université Toulouse 3 Paul Sabatier, 2020.

[5] R. Virkkunen and R. M. Nieminen. First-principles study of the phosphorous-vacancy pair in silicon. *Computational Materials Science*, 1(4):351–357, 1993.

[6] A. N. Larsen, A. Mesli, K. B. Nielsen, H. K. Nielsen, L. Dobaczewski, J. Adey, R. Jones, D. W. Palmer, P. R. Briddon, and S. Öberg. E center in silicon has a donor level in the band gap. *Physical Review Letters*, 97(10):106402, 2006.

[7] M. G. Ganchenkova, A. Y. Kuznetsov, and R. M. Nieminen. Electronic structure of the phosphorus-vacancy complex in silicon: A resonant-bond model. *Physical Review B*, 70(11):115204, 2004.

[8] G. Pfanner, C. Freysoldt, J. Neugebauer, and U. Gerstmann. Ab initio EPR parameters for dangling-bond defect complexes in silicon: Effect of Jahn-Teller distortion. *Physical Review B*, 85:195202, May 2012.

[9] G. Herrero-Saboya, L. Martin-Samos, A. Jay, A. Hémeryck, and N. Richard. A comprehensive theoretical picture of E centers in silicon: From optical properties to vacancy-mediated dopant diffusion. *Journal of Applied Physics*, 127(8), 2020.

[10] K. Szász, T. Hornos, M. Marsman, and A. Gali. Hyperfine coupling of point defects in semiconductors by hybrid density functional calculations: The role of core spin polarization. *Physical Review B*, 88(7):075202, 2013.

[11] P. Giannozzi, S. Baroni, N. Bonini, M. Calandra, R. Car, C. Cavazzoni, D. Ceresoli, G. L. Chiarotti, M. Cococcioni, I. Dabo, A. Dal Corso, S. De Gironcoli, S. Fabris, G. Fratesi, R. Gebauer, U. Gerstmann, C. Gougoussis, A. Kokalj, M. Lazzeri, L. Martin-Samos, N. Marzari, F. Mauri, R. Mazzarello, S. Paolini, A. Pasquarello, L. Paulatto, C. Sbraccia, S. Scandolo, G. Sclauzero, A. P. Seitsonen, A. Smogunov, P. Umari, and R. M. Wentzcovitch. Quantum ESPRESSO: a modular and open-source software project for quantum simulations of materials. *Journal of Physics: Condensed Matter*, 21(39):395502, 2009.

[12] P. Giannozzi, O. Baseggio, P. Bonfà, D. Brunato, R. Car, I. Carnimeo, C. Cavazzoni, S. De Gironcoli, P. Delugas, F. Ferrari Ruffino, A. Ferretti, N. Marzari, I. Timrov, A. Urru, and S. Baroni. Quantum ESPRESSO toward the exascale. *The Journal of Chemical Physics*, 152(15):154105, 2020.

[13] J. P. Perdew, K. Burke, and M. Ernzerhof. Generalized gradient approximation made simple. *Physical Review Letters*, 77(18):3865, 1996.

[14] C. J. Pickard and F. Mauri. All-electron magnetic response with pseudopotentials: NMR chemical shifts. *Physical Review B*, 63:245101, May 2001.

[15] The pseudopotentials files used for calculations are `Si.pbe-tm-new-gipaw-dc.UPF`, `P.pbe-tm-new-gipaw-dc.UPF` and `N.pbe-tm-new-gipaw-dc.UPF` available online from D. Ceresoli's repository `https://sites.google.com/site/dceresoli/`.

[16] N. Varini, D. Ceresoli, L. Martin-Samos, I. Girotto, and C. Cavazzoni. Enhancement of DFT-calculations at petascale: Nuclear magnetic resonance, hybrid density functional theory and Car–Parrinello calculations. *Computer Physics Communications*, 184(8):1827–1833, 2013.

[17] R. Fletcher. A new approach to variable metric algorithms. *The Computer Journal*, 13(3):317–322, 1970.

[18] C. G. Broyden. The convergence of a class of double-rank minimization algorithms 1. general considerations. *IMA Journal of Applied Mathematics*, 6(1):76–90, 1970.

[19] M. J. Van Setten, M. Giantomassi, E. Bousquet, M. J. Verstraete, D.R. Hamann, X. Gonze, and G.-M. Rignanese. The pseudodojo: Training and grading a 85 element optimized norm-conserving pseudopotential table. *Computer Physics Communications*, 226:39–54, 2018.

[20] D. Skachkov, W. R. L. Lambrecht, H. J. Von Bardeleben, U. Gerstmann, Q. D. Ho, and P. Deák. Computational identification of Ga-vacancy related electron paramagnetic resonance centers in β-Ga_2O_3. *Journal of Applied Physics*, 125(18):185701, 05 2019.

[21] L. Giacomazzi, L. Martin-Samos, and N. Richard. Paramagnetic centers in amorphous GeO_2. *Microelectronic Engineering*, 147:130–133, 2015. Insulating Films on Semiconductors 2015.

[22] H. J. von Bardeleben, E. Rauls, and U. Gerstmann. Carbon vacancy-related centers in 3c-silicon carbide: Negative-u properties and structural transformation. *Phys. Rev. B*, 101:184108, May 2020.

Chapter 4

Unraveling spectroscopic fingerprints of the substitutional nitrogen in silicon: an instance of the pseudo Jahn-Teller effect

Spectroscopic techniques are powerful tools that provide valuable data about molecules and solid-state systems. However, they have some limitations and challenges. For instance, experimental conditions need to be closely monitored and some instruments have a limited resolution which restricts the ability to distinguish fine details in spectra. Moreover, a given technique provides specific types of information (*e.g.*, absorption, emission, vibrational frequencies), and some properties or interactions may not be directly observable through spectroscopic methods. Indeed, it is often necessary to couple several methods to obtain a complete characterisation of a defect properties. In the case of defects in semiconductors, atomic scale computational methods such as DFT play a crucial role in complementing interpretation of experimental data. They also allow to predict properties that cannot accurately be accessed via experiments, thus guiding identification and characterisation of centers. Paramagnetic N-related defects were the object of several electron paramagnetic spectroscopy investigations which assigned the so-called SL5 signal to the presence of substitutional nitrogen (N_{Si}). Nevertheless, its behaviour at finite temperatures has been imprecisely linked to the metastability of the center. In this chapter, based on the robust identification of the SL5 signature, a theoretical model for N_{Si} is provided. In section 4.1, a review of both experimental and theoretical characteristics of the defect is provided. Next, in section 4.2, a theoretical picture of the substitutional nitrogen is established. Through an understanding of its symmetry-breaking mechanism, a model of its fundamental physical properties (*e.g.* its energy landscape) based on simple symmetry considerations [1, 2] and *ab initio* calculations is provided. Moreover, by including more refined density functional theory-based approaches, EPR parameters ($\overleftrightarrow{g}$- and $\overleftrightarrow{A}$ tensors) are calculated, elucidating the debate on the metastability of N_{Si}. Finally, by computing thermodynamic charge transition

levels within the GW method, reference values for the donor and acceptor levels of N_{Si} are presented.

4.1 Review of N_{Si} center spectroscopic properties and previous *ab initio* models

As mentioned in Section 1.1.2, nitrogen is used as dopant in silicon to enhance its mechanical and chemical properties [3–7]. The precise nature of the nitrogen-related centers responsible for these effects is unclear. Nonetheless the suppression of the formation of voids has been directly correlated to the creation of nitrogen–vacancy complexes [8]. Indeed, several nitrogen-related defects (nitrogen–nitrogen pairs, nitrogen–vacancy complexes, etc.) have been associated with the electrical and/or optical signature of N-doped silicon [9–18]. However, it has been challenging to assign a spectroscopic signal to a specific defect. In the case of DLTS, one set of deep levels is often assigned to the overall presence of nitrogen or to a subset of N-related defects. This ambiguous assignment can even include defects that do not share a similar atomic structure, such as substitutional nitrogen (N_{Si}) or the nitrogen–vacancy complex (NV), for instance [19]. On the other hand, from EPR spectroscopy several signals have been associated with the presence of nitrogen [20, 21]. Among these EPR signals, only the so-called SL5 center has been unequivocally associated with the substitutional nitrogen (N_{Si}) [20–23].

From the first EPR measurements [20, 21], it was inferred that contrary to other group V substitutional impurities in silicon (*e.g.,* phosphorous and arsenic), nitrogen does not remain in its tetra-coordinated on-center (T_d) site (Figure 4.1). Instead, it resides in a tri-coordinated off-center configuration along one of the ⟨111⟩ crystal directions, with a lower C_{3v} symmetry. This symmetry-breaking (SB) mechanism was first associated with a Jahn–Teller effect [20, 21] that predicts the instability of high symmetry configurations with partially occupied degenerate states [24]. This hypothesis was rejected by early electronic structure calculations [25, 26] that located the unpaired electron in a single-particle non-degenerate a_1 state of the T_d configuration. The triply degenerate states t_2 were found within the conduction band (CB) and the SB mechanism was referred to as a pseudo Jahn–Teller effect [26].

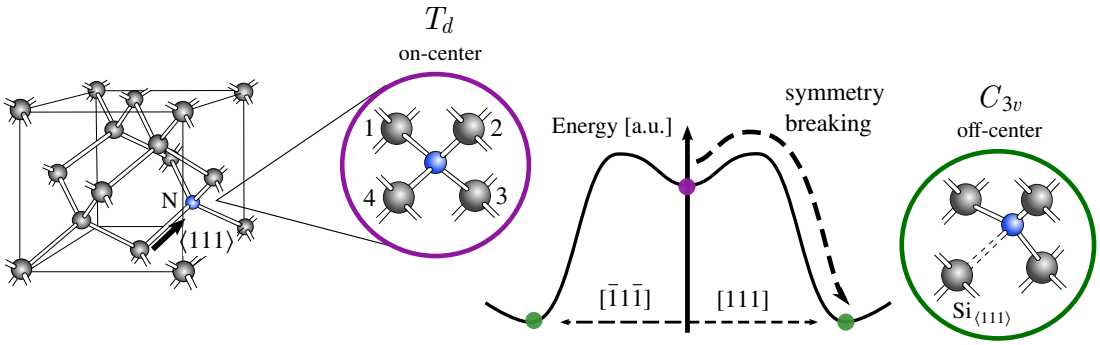

Fig. 4.1: Substitutional nitrogen in silicon. The proposed symmetry breaking (SB) mechanism $T_d \rightarrow C_{3v}$ for this point-defect is depicted for nitrogen (in blue) and its first silicon neighbours [20, 21]. In the lower C_{3v} symmetry, the Si atom positioned along the axes of the distortion or the ⟨111⟩ direction is explicitly labelled. The suggested PES corresponding to this SB is also illustrated. Two equivalent off-center minima with C_{3v} symmetry are represented in green for the crystal directions [1̄1̄1̄] and [111]. A metastable on-center minimum (T_d symmetry) is depicted in purple.

The energy landscape associated with this pseudo Jahn–Teller mechanism was investigated from electronic structure calculations by displacing the N atom along one of the equivalent ⟨111⟩ crystal directions [26]. The resulting potential energy surface (PES) presented a small energy barrier of ∼0.05 eV between the on-center and off-center configurations, indicating the possible metastability of the defect (see PES in Figure 4.1). The authors of this study, however, express caution regarding the accuracy of this value due to the simplicity of their model. Through early EPR stress measurements [20,21], the reorientation between equivalent off-center configurations at finite temperatures (T > 35 K) was observed, with a barrier of 0.107 ± 0.02 eV. As a consequence of this thermally activated mechanism, the center was interpreted to be in an average tetrahedral configuration (*i.e.* each defect in the sample randomly orients along one direction, resulting in an overall tetrahedral signal). Later EPR measurements [23, 27, 28] did, however, associate the existence of an on-center configuration with an increase of the hyperfine splitting when the temperature rises. For temperatures above 150 K, the increase of the splitting indicates that the reorientation of the center is faster with raising temperatures [28]. This evidence was then correlated to the model of the PES in Figure 4.1 [23, 27, 28], postulating that the finite temperature dynamics of N_{Si} are characterised by the existence of a metastable on-center geometry and the reorientation between equivalent off-center configurations. The energy difference between configurations and hyperfine splitting of the on-center structure were then mathematically extrapolated using experimental measurements and this model, with values of 73 meV and 134 G (∼ 376.4 MHz) respectively.

Even if the symmetry-breaking mechanism depicted in Figure 4.1 was undoubtedly associated with the existence of deep levels in the silicon band gap, early optical measurements were incapable of providing a clear picture of their nature and relative position [20,21]. Furthermore, a majority of DLTS activation energies have been attributed to the overall presence of nitrogen in the sample rather than to a specific center [9–15]. Previous studies have also referred to both the substitutional impurity and the nitrogen–vacancy complex as the NV center, leading to confusion in assigning the observed levels [4, 8, 19, 29]. Among these investigations, two independent set of deep levels were tentatively assigned to substitutional nitrogen: the first set of DLTS activation energies were attributed to a single donor and single acceptor levels at 0.31 eV and 0.08 eV from CB, respectively [30], whereas the second DLTS spectra were associated with single and double acceptor levels at 0.64 eV and 0.34 eV from CB [19].

On the computational side, many works have attempted to establish a model of the structural and electronic properties for substitutional nitrogen matching experimental data of the SL5 center, using a range of computational methods. Through either Hartree-Fock calculations on clusters [31, 32], LDA calculations on supercells [33, 34] or a tight-binding method on a cluster [35], the off-center configuration is consistently identified as the ground state while the on-center is found as a metastable state. While the HF method [32] produces energy difference between configurations and reorientation barrier values that are one order of magnitude too large, LDA calculations [33, 34] provide results consistent with experimental measurements [20, 21, 28]. Similarly, the electronic structure, in particular splitting of the t_2 degenerate states of the on-center and the ordering of the single-particle defect states on the off-center are qualitatively correct [32, 33]. Recent works have performed state-of-the-art electronic structure calculations on various N-related defects in silicon [36–38]. While these studies have addressed

the structural properties of substitutional nitrogen [36–38], as well as its single-particle band structure [37, 38], no attempts were made to explore the possible metastability of the center or estimate its deep levels with a sufficient level of theory.

4.2 *Ab initio* spectroscopic properties of the N_{Si} center in silicon

In the following section, a thorough investigation of the SB mechanism in substitutional nitrogen from *ab initio* calculations is performed, enabling to establish its fundamental physical properties. Moreover, by including more refined DFT-based methods (i.e., linear response treatments and many-body corrections), a direct comparison between the atomistic model of substitutional nitrogen and the spectroscopic signals assigned to it, i.e., EPR parameters and DLTS levels is established.

4.2.1 The symmetry breaking in N_{Si}: pseudo Jahn-Teller effect

The first-principle calculations presented in this work confirms that the ground state geometry of N_{Si}^0 displays an off-center configuration with C_{3v} symmetry, rather than the on-center configuration or the tetrahedral (T_d) symmetry. In the on-center configuration, four equivalent N – Si interatomic distances of 2.05 Å are found between the N atom and its nearest neighbours (or silicon atoms 1, 2, 3 and 4 in Fig. 4.1). These Si atoms form a tetrahedron with an edge length of 3.34 Å. With the atomic distortion, the N atom moves away from one of its nearest neighbours (silicon atom 4 in Fig. 4.1), elongating the N-Si distance to 3.15 Å (Fig. 4.2a). The remaining three equivalent N-Si distances are shortened to 1.86 Å, similar to the N-Si bond length (1.73 Å) in silicon nitride [39]. The displacement of the N atom along the C_3 symmetry axis also distorts the tetrahedron formed by its nearest neighbours. The Si atom along the axis of distortion (denoted from now on the $Si_{\langle 111 \rangle}$ atom) is 3.87 Å away from the remaining three Si atoms, whose interatomic distances are 3.20 Å. The analysis of the symmetry breaking indicates that the total displacement of the nitrogen atom away from its substitutional site is 0.57 Å. In its off-center configuration, the N atom lies relatively close (0.25 Å) to the interatomic plane defined by its nearest neighbours (or silicon atoms 1, 2 and 3 in Fig. 4.1). Both these distances are in agreement with previously reported values [37, 38].

To gain a deeper understanding of the symmetry breaking (SB) in substitutional nitrogen, the one-electron defect states of both the on-center and off-center configurations are examined. The one-electron wavefunctions are approximated using Kohn–Sham eigenfunctions and their corresponding energy levels using quasiparticle (Kohn–Sham) eigenvalues computed at Γ. Fig. 4.2b shows the one-electron energies corresponding to the on-center and off-center geometries, along with the real space projection of the wavefunctions of the singlet defect states. In the on-center configuration, a partially occupied a_1 state is located at 0.43 (0.20) eV from the valence band maximum (VBM). As depicted in Fig. 4.2b, the one-electron wavefunction is

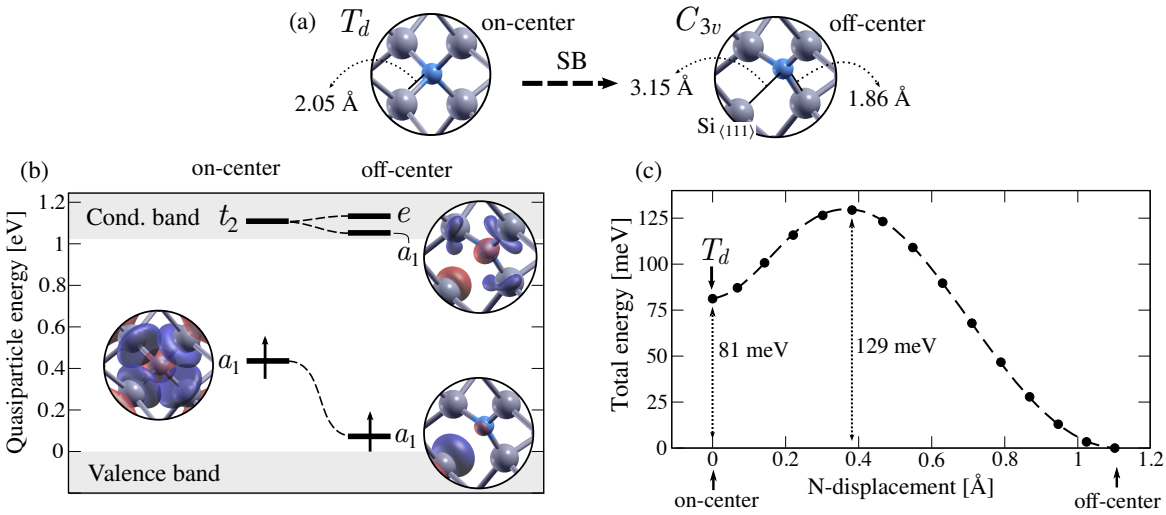

Fig. 4.2: *Ab initio* characterisation of the symmetry-breaking mechanism (SB) in substitutional nitrogen. (a) Relaxed defect structures depicting nitrogen and its nearest neighbours for the on-center and off-center configurations. Interatomic distances between nitrogen and its first neighbours are displayed. (b) Defect-induced states for the on-center and off-center configurations. Quasiparticle (QP) energies (computed at the GW level) of defect states estimated at Γ for a 216 atoms SC are represented with respect to the valence band maximum and the conduction band minimum for the spin-up channel. Defect states are labelled according to their irreducible representation and the Kohn–Sham wavefunctions corresponding to singlet states a_1 are shown. (c) Minimum energy path (MEP) between the on-center and off-center configurations. The DFT total energy is plotted with respect to the displacement of the N atom from its on-center position to its off-center configuration. The energy difference between the two minima is shown, as well as the energy barrier from off-center to on-center geometries.

centered in the N atom and is equally distributed among the four neighboring Si atoms. The unoccupied triplet states t_2, predicted in the theoretical model [26] (Fig. 4.1), are found within the CB, at 0.09 (0.08) eV from the conduction band minimum (CBM). After the symmetry breaking, the partially occupied a_1 state lowers its energy, whereas the t_2 state splits into a second singlet a_1 and a doublet e (in agreement with symmetry considerations [2] and the previous model [26]). The partially occupied singlet state is located within the band gap, at 0.07 (0.02) eV from the VBM, and is primarily localized on the $Si_{\langle 111\rangle}$ atom and to a lesser extent on the nitrogen atom. The second singlet state is found within the CB, at 0.03 (0.03) eV from the CBM. The doublet state hybridizes with the conduction states and is found at 0.11 (0.11) eV from the CBM. It is interesting to notice that both the KS wavefunctions and the QP eigenvalues are computed at Γ and represented within the folded bulk bands. However, when k-points are added to the calculation, a large dispersion of the defect states is observed, as shown in the band structures for both defect configurations in Fig. 4.3. For both the on-center and off-center configurations, the highest occupied state corresponds to a spin up defect state, $a_1^{\uparrow}$, located within the silicon bands. The lowest unoccupied state is therefore the spin down projection of that defect state, $a_1^{\downarrow}$. In the case of the on-center configuration, the dispersion

is rather significant, since the highest occupied state becomes lower than the lowest unoccupied state, $\epsilon_{a_1^{\uparrow}}(\mathbf{k} = \mathrm{L}) < \epsilon_{a_1^{\downarrow}}(\mathbf{k} = \Gamma)$, resulting in a **negative band gap**. In the case of the off-center configuration, the dispersion of defect states is most notable for the $a_1^{\downarrow}$ state, and almost negligible for the $a_1^{\uparrow}$ state. The band dispersion is therefore more important for the spin down projection of the relevant states, emphasizing the necessity to include both spins to properly characterise the band structure of the defect and ascertain limits to the current model. This inaccuracy, though crucial to assess the limitations of PBE calculations in quantifying fundamental properties of this defect, was not previously reported in prior DFT calculations employing parameters akin to those presented in this work [37].

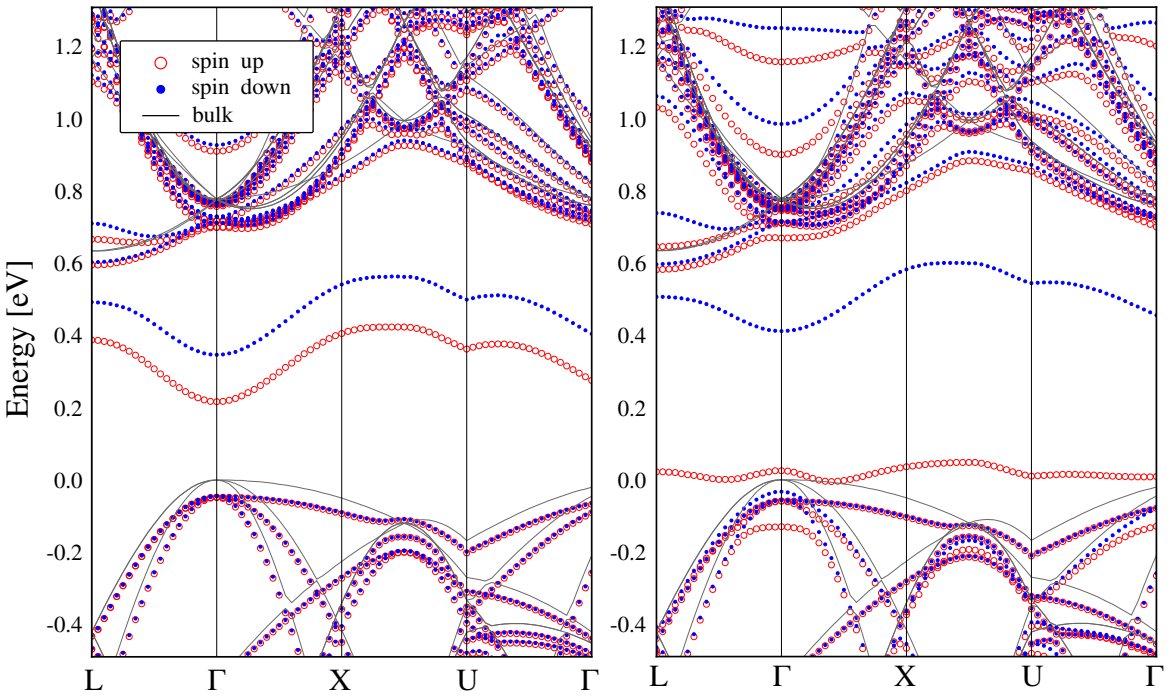

Fig. 4.3: Band structures of substitutional nitrogen in 216-atom cells from standard PBE calculations. Kohn-Sham eigenvalues for the on-center (left) and off-center (right) configurations are shown. Spin up *versus* spin down contributions are represented in red and blue respectively. The eigenvalues corresponding to the pristine cell are depicted in black. The zero energy corresponds to highest occupied Kohn-Sham eigenvalue in the pristine cell (or the top of the valence band).

Based on the energy diagrams shown in Fig. 4.2b and, in particular, the absence of partially occupied degenerate states, the symmetry breaking $\mathrm{T_d} \rightarrow \mathrm{C_{3v}}$ is not a Jahn–Teller effect [24]. Thus, the PES of substitutional nitrogen does not exhibit the standard conical intersection, where the highly symmetric configuration is located at the top of the so called Mexican hat-shaped PES. In this case (or in the case of a pseudo Jahn–Teller effect [26]), the shape of the PES cannot be induced from symmetry considerations and so the nature of the critical points ($\mathrm{T_d}$, $\mathrm{C_{3v}}$) of the PES cannot be predicted without explicit electronic structure calculations. To begin exploring the PES of substitutional nitrogen in silicon, the Minimum Energy Path (MEP)

between the on-center and off-center configurations is examined. In Fig. 4.2c, the total DFT energy is plotted along the MEP, whose coordination reaction is taken as the displacement of the N atom away from its ideal on-center position. As depicted in Fig. 4.2c, the MEP between these geometries corresponds to a linear interpolation between both structures. It should be noted that the energy difference between the two configurations is not negligible, with a value of 81 meV. This value is in decent agreement with previous estimations of 50 meV [37] and 80 meV [36]. Additionally, an energy barrier of 129 meV between the on-center and off-center configurations is observed. The existence of two energy minima separated by a saddle point therefore indicate that both the tetrahedral (T_d) and the trigonal (C_{3v}) configurations are metastable states of the substitutional nitrogen.

The PES of substitutional nitrogen is further explored by investigating the transition path between equivalent off-center configurations. Since the symmetry breaking preserves any of the original C_3 symmetry axes, the nitrogen atom can move along any of the equivalent $\langle 111 \rangle$ directions away from its first silicon neighbors (Fig. 4.1). As a result, the PES is characterised by four equivalent global minima as off-center configurations and the defect can reorient at finite temperatures. As a first approximation to the MEP between equivalent configurations, a linearly interpolated path along which the N atom avoids its on-center site is tested. However, the transition path relaxes to pass through the tetrahedral (T_d) symmetry, resulting in the MEP in Fig. 4.2c. The N atom is therefore forced to transit through its on-center configuration to jump between equivalent off-center configurations. It is important to note that the activation energy for this reorientation mechanism cannot be simply estimated as the energy barrier between the on-center and off-center configurations, since the T_d symmetry is a metastable minimum. Namely, the defect could remain trapped in its on-center configuration, delaying the transition to another global minimum. Before comparing the shape of the PES presented to experimental observations, the potential influence of size effects on the MEP is addressed. For this purpose, relaxation calculations for both on-center and off-center defect structures within a 512-atom cell are performed. The resulting interatomic distances differ by no more than 0.03 Å, from the previously described bond lengths. The energy difference between these structures is 81 meV and the energy barrier is 129 meV, indicating that the MEP obtained with the 216-atom cell is converged within 10 meV.

4.2.2 *Ab initio* EPR parameters

Once the ground state configuration of the neutral substitutional nitrogen is well described, the corresponding EPR parameters are calculated to provide an explicit comparison with experimental data. In particular, in Table 4.1, the principal values of the $\overleftrightarrow{g}$ tensor and of the hyperfine tensors together with their isovalues (g_{iso} and A_{iso}) for the off-center configuration are shown. The hyperfine tensors refer to the silicon atom along the atomic distortion (or the $Si_{\langle 111 \rangle}$ atom) and to the nitrogen impurity. The substantial disparity between A_i principal values corresponding to the $Si_{\langle 111 \rangle}$ atom and the N atom reflects the notable localization of the unpaired electron on the Si atom (see wavefunction of the a_1 state in Fig. 4.2b). Concerning the $\overleftrightarrow{g}$ tensor, the defect has an axial symmetry and the principal value g_1 is designated as the

one corresponding to the principal axis parallel to the ⟨111⟩ direction (or $g_{\parallel}$). Consequently, the g_2 and g_3 values correspond to any two axes perpendicular to the ⟨111⟩ direction (or $g_{\perp}$).

From the values in Table 4.1, it is apparent that the axial symmetry is not fully preserved, as indicated by the inequality of g_2 and g_3. This small deviation is within the expected inaccuracy estimates of the GIPAW method [40, 41] and cannot be attributed to a poor description of the defect geometry, since the estimated interatomic distances are fully compliant with the C_{3v} symmetry. However, it can be assigned to the artificial dispersion of the defect states when several k-points are included in the sampling of the Brillouin zone (as seen from Fig. 4.3).

In Table 4.1, the EPR parameters calculated in this work for the off-center configuration are compared to the reported EPR data of the SL5 center [20–22]. The calculated principal values of the hyperfine structure tensor $\overleftrightarrow{A}$ are within 12% of the experimental ones for the silicon atom along the ⟨111⟩ distortion and within 20% for the nitrogen impurity [20–22]. Moreover, both the principal values and the isovalue of the $\overleftrightarrow{g}$ tensor lie within ∼1000 ppm of those measured by Brower [20, 21] and with even better agreement (∼700 ppm) with the most recent measurements [22]. Earlier theoretical calculations of the hyperfine tensors for the off-center configuration, were derived using the Hartree–Fock approximation for a relatively small atomic cluster NSi_4H_{12} [42]. However, the calculated isovalues exhibited significant discrepancies when compared to experimental EPR data [20–22]. Specifically, the calculated value for $A_{iso}(^{29}Si)$ was overestimated, while the one for $A_{iso}(N)$ was underestimated, with deviations of nearly a factor of 2 in both cases [42]. By contrast, the computed *ab initio* EPR parameters in this work (both $\overleftrightarrow{g}$ and $\overleftrightarrow{A}$ tensors) display excellent agreement with the experimental data and hence provide a firmly grounded theoretical assignment of the SL5 EPR center to the distorted off-center configuration of the substitutional nitrogen.

Besides investigating the magnetic properties of a frozen N atom, the dynamics of the SL5 center were also investigated from EPR stress measurements [20, 21]. In particular, the broadening of the spectral lines at temperatures above 35 K was attributed to the reorientation of the defect between equivalent off-center configurations. Based on this analysis, the activation energy for the N atom to jump from one ⟨111⟩ distortion to another was inferred to be 0.11 ± 0.02 eV [21]. From the exploration of the PES, an energy barrier of at least 0.129 eV between equivalent off-center distortions is obtained (Fig. 4.2c). This evaluation is in rather good agreement with the experimental estimate of 0.11 eV. Notice, however, that given the existence of a metastable on-center minimum in the reorientation path in the present study, the effective activation energy for the reorientation process is expected to be slightly higher. Before even estimating this effective barrier, in the following, the existence of a metastable on-center configuration is reassessed. From EPR measurements [20–23, 27, 28], an argument in favour of a metastable on-center configuration was put forward to explain the observed increase in the hyperfine splitting when increasing the temperature [23, 28]. In order to elucidate the existence of this metastable minimum, its EPR parameters (Table 4.1) are estimated and compared to the values previously assigned to this tetrahedral configuration [23, 28]. In this highly symmetric configuration, the $\overleftrightarrow{g}$ tensor and the $\overleftrightarrow{A}$(N) hyperfine tensor are expected to be isotropic. In fact, as reported in Table 4.1, an isotropic hyperfine tensor with a considerably large isovalue

Tab. 4.1: EPR parameters of substitutional nitrogen in silicon. For the off-center configuration, the estimated $\overleftrightarrow{g}$ and the hyperfine $\overleftrightarrow{A}$ tensors for the N impurity (^{14}N) and Si atom along the $\langle 111 \rangle$ distortion ($^{29}\mathrm{Si}_{\langle 111 \rangle}$) are shown (tw-off), together with EPR data of the SL5 center [20–22]. Calculated hyperfine $\overleftrightarrow{A}$ tensors are also displayed for the on-center geometry in the 216-atom cell (tw-on) and in the NSi_4H_{12} cluster (tw-cluster). These values are compared to EPR data [23, 28]. Also, the $\overleftrightarrow{g}$-tensor as calculated for the NSi_4H_{12} cluster is given.

	$\overleftrightarrow{\mathbf{g}}$				$\overleftrightarrow{\mathbf{A}}$ ($^{29}\mathbf{Si}_{\langle 111 \rangle}$) (MHz)				$\overleftrightarrow{\mathbf{A}}$ (^{14}N) (MHz)			
Ref.	$\mathbf{g_1}$	$\mathbf{g_2}$	$\mathbf{g_3}$	$\mathbf{g_{iso}}$	$\mathbf{A_1}$	$\mathbf{A_2}$	$\mathbf{A_3}$	$\mathbf{A_{iso}}$	$\mathbf{A_1}$	$\mathbf{A_2}$	$\mathbf{A_3}$	$\mathbf{A_{iso}}$
tw-off	2.0020	2.0089	2.0078	2.0062	–380.4	–205.9	–205.9	–264.1	37.5	29.6	29.6	32.2
[20, 21]	2.0026	2.0089	2.0089	2.0068	397.5	231.7	231.7	287.0	45.3	36.3	36.3	39.3
[22]	2.00219	2.00847	2.00847	2.00638	396.6	234.7	234.7	288.7	45.85	36.49	36.49	39.61
tw-on	-	-	-	-	–55.0	–32.6	–32.6	–40.1	165.7	165.7	165.7	165.7
tw-cluster	2.0056	2.0056	2.0056	2.0056	–58.4	–13.2	–13.2	–28.3	226.6	226.6	226.6	226.6
[23] ([28])	-	-	-	2.0065	-	-	-	-	-	-	-	45.5 (376.2)

(165.7 MHz) is found, while the isovalue on the silicon ($|A_{iso}(^{29}Si)| = 40.1$ MHz) is about the same as found for the nitrogen impurity in the off-center configuration. Because of numerical instabilities in the calculations of the $\overleftrightarrow{g}$ tensor for the on-center configuration (*i.e.* due to instabilities in the GIPAW calculations), an EPR demonstration calculation on a hydrogen-passivated silicon cluster, specifically the NSi_4H_{12} cluster, is performed. This cluster features four N-Si bonds with a length of 1.89 Å and Si-Si distances of 3.08 Å. As shown in Table 4.1, both the calculated $\overleftrightarrow{g}$ and $\overleftrightarrow{A}$(N) tensors are isotropic and the value of the hyperfine coupling constant (226.6 MHz) is consistent with the one (165.7 MHz) calculated for the on-center N_{Si} in the silicon supercell.

The calculated hfi tensors $\overleftrightarrow{A}$(N) of the on-center configuration are in disagreement with the experimental room temperature hfi splitting value given in [23]. Yet, in [28] the temperature dependence of the hfi splittings is fitted by means of Boltzmann weights. From the fit, a remarkably large value of 376 MHz was assigned to the N in the on-center configuration. From the presented model, the defect state is transferred from N to Si when moving from on-center to off-center configuration (see Fig. 4.2c). This implies that the value of A_{iso}(N) drastically decreases with this transfer, thus it would seem unlikely that this value only differs by ~ 5 MHz between the two configurations [21, 23, 30]. A remarkably larger difference can be expected, as suggested by Murakami's fit [28] and by the calculated results presented in Table 4.1. In fact, A_{iso} should be significantly larger for the atom around which the paramagnetic state is located. In the calculations performed in this work, the values are for instance $A_{iso}(^{14}N)$ and $A_{iso}(^{29}Si)$ of 226.6 MHz and –28.3 MHz, respectively, for the on-center configuration that become 32.2 MHz and –264.1 MHz, respectively, in the off-center configuration. From the computational model suggested, this means that even if a metastable on-center minimum is found in the exploration of the PES, the ratio between the off-center and on-center occupation (from Boltzmann weights) is about 120 at room temperature. Hence, its implication in the thermally activated dynamics is minimal and its contribution to the *averaged* spectroscopic signals is minor, leading just to a small increase ($\sim$5 MHz) in the hfi splittings at room temperature. Yet, the on-center configuration can be tracked down from the temperature-induced increase in the hfi splittings [28]. The latter, however, might also involve an effect due to coupling with the phonons of the off-center potential well. Therefore, contrary to the interpretation suggested by Ref [23], the on-center configuration should not be mistaken with the room- or high-temperature averaged configuration of N_{Si}. In fact, the averaged spectroscopic signals depend on the occupation probability of both minima (the four degenerate off-center and the on-center).

4.2.3 Charge Transition Levels of N_{Si}

Once a computational model for neutral substitutional nitrogen has been proposed, its relative stability compared to other charge states is investigated. In particular, charge states +1, –1 and –2 are investigated and their respective CTLs determined. At charge state +1, there is no *trapped* electron within the silicon band gap and the defect remains in an on-center configuration, with a N-Si bond length of 2.05 Å. At charge state –1, the off-center configuration is

preferred and so the a_1 defect state is fully occupied. Along the distortion, the N-Si$_{\langle 111 \rangle}$ bond is 3.07 Å, whereas the remaining three N-Si distances are equal to 1.85 Å. If yet another electron is added to the defect, the system remains in an off-center configuration, with a characteristic N-Si$_{\langle 111 \rangle}$ distance of 1.85 Å, compared to the three N-Si bond lengths of 3.04 Å. This charge state –2 is paramagnetic, with the defect state a_1 in the CB partially occupied.

Calculated thermodynamic CTLs, obtained within the PBE+GW (PBE) approach, for the single donor and the single acceptor levels of substitutional nitrogen are presented in Table 4.2. The donor level is found relatively close to the VBM, with calculated values of $\epsilon_{\mathrm{VBM}} + 0.19$ (0.08) eV. In contrast, the acceptor level is located deep in the silicon band gap, positioned at $\epsilon_{\mathrm{CBM}} - 0.55$ (0.32) eV from the CBM. Notice that both values correspond to the mid-region of the silicon band gap, considering that the band gap is estimated to be 1.02 (0.63) eV. Finally, the double acceptor level is found within the CB, at 0.06 (0.06) eV from the CBM. The charge state –2 is therefore thermodynamically unstable. The existence of a single donor and acceptor levels for N_{Si} was previously reported via an *ab initio* calculation [36]. The proposed values were $\epsilon_{\mathrm{VBM}} + 0.5$ eV and $\epsilon_{\mathrm{CBM}} - 0.4$ eV, respectively. Notice, however, that they reported an electrical gap of 0.5 eV and that a corrective shift of the estimated levels was made. Contrary to the approaches used in this thesis (Table 4.2), their corrected levels are both deep in the band gap, at ∼0.25 eV from each other. Given the well-established accuracy of the DFT+GW approach estimating single donor and acceptor levels, the existence of a donor level close to the VBM is reiterated.

In Table 4.2, a comparison between calculated CTLs and the DLTS activation energies tentatively assigned to the off-center substitutional nitrogen [19, 30] is presented. There is a significant disparity between the reported values in [30] and those estimated in this study. Given the accuracy of the DFT+GW method [43], the assignment of the levels $\epsilon_{\mathrm{CBM}} - 0.31$ eV and $\epsilon_{\mathrm{CBM}} - 0.08$ eV to substitutional nitrogen appears incorrect. In contrast, the proximity of the estimated acceptor level with the one proposed in a recent DLTS investigation [19] is noted. Nonetheless, the discrepancy between their identified double acceptor level and the computed value is acknowledged. From this disparity, either the assignment of both acceptor levels to substitutional nitrogen was incorrect or these levels are the signature of another N-related defect (*e.g.*, the nitrogen–vacancy complex).

To conclude this section, a systematic investigation of the symmetry-breaking mechanism in substitutional nitrogen from first-principle calculations was performed. The fundamental properties of both the on-center and off-center configurations of N_{Si} were characterised, including the relative position of its single-particle defect states within the band gap. Moreover, we proposed a model for its potential energy surface by performing an extensive search of the minimum energy path between equivalent off-center configurations. Such a transition path forces the nitrogen center to pass through the on-center configuration that is estimated to be a shallow metastable minimum. In order to provide a direct comparison with spectroscopic signals, the EPR parameters and the thermodynamic CTLs of N_{Si} were computed. The EPR values presented in this thesis for the off-center configuration are in excellent agreement with the SL5 EPR signature. Moreover, the energy barrier calculated for the reorientation mechanism be-

Tab. 4.2: Deep levels located within the band gap associated with substitutional nitrogen in silicon. Thermodynamic CTLs were calculated within a standard PBE approximation (tw-PBE) and within the combined DFT and GW approach (tw-PBE+GW). Previously estimated levels (pw) are also included [36]. DLTS levels were tentatively assigned to susbstitutional nitrogen [30] and activation energies associated with the off-center nitrogen, however, also addressed as NV center, in [19]. All levels are given from the conduction band minimum in eV.

Reference	$\epsilon(+/0)$	$\epsilon(0/-)$	$\epsilon(-/2-)$
tw-PBE	0.55	0.32	-
tw-PBE+GW	0.83	0.55	-
pw [36]	-	0.40	-
Exp. [30]	0.31	0.08	-
Exp. [19]	-	0.64	0.34

tween equivalent off-center configurations is in fair agreement with EPR stress measurements, validating our model for its potential energy surface. Furthermore, the calculations further support a large hyperfine splitting value for the N_{Si} in the on-center configuration as estimated in [28]. Finally, a set of deep levels was proposed for N_{Si}, corresponding to a single donor and acceptor levels. The values allowed to identify incorrect assignments between DLTS activation energies and the electrical activity of N_{Si} and they can guide its identification in future works.

Bibliography

[1] G. Herrero-Saboya. *Defects in silicon: revisiting theoretical frameworks to guide ab initio characterization*. PhD thesis, Université Toulouse 3 Paul Sabatier, 2020.

[2] G. Herrero-Saboya, L. Martin-Samos, N. Richard, and A. Hémeryck. Common defects in diamond lattices as instances of the general $T\otimes(e + t_2)$ Jahn-Teller effect. *Physical Review Materials*, 6(3):034601, 2022.

[3] V. Orlov, H. Richter, A. Fischer, J. Reif, T. Müller, and R. Wahlich. Mechanical properties of nitrogen-doped CZ silicon crystals. *Materials Science in Semiconductor Processing*, 5(4):403–407, 2002.

[4] V. V. Voronkov and R. J. Falster. Multiplicity of nitrogen species in silicon: The impact on vacancy trapping. In *Gettering and Defect Engineering in Semiconductor Technology XII*, volume 131 of *Solid State Phenomena*, pages 219–224. Trans Tech Publications Ltd, 1 2008.

[5] S. Yuan and D. Yang. Nitrogen impurity in crystalline silicon. *Handbook of Photovoltaic Silicon*, pages 463–494, 2019.

[6] C. R. Alpass, J. D. Murphy, R. J. Falster, and P. R. Wilshaw. Nitrogen diffusion and interaction with dislocations in single-crystal silicon. *Journal of Applied Physics*, 105(1):013519, 2009.

[7] W. V. Ammon, P. Dreier, W. Hensel, U. Lambert, and L. Köster. Influence of oxygen and nitrogen on point defect aggregation in silicon single crystals. *Materials Science and Engineering: B*, 36(1-3):33–41, 1996.

[8] V. V. Voronkov and R. Falster. Nitrogen interaction with vacancies in silicon. *Materials Science and Engineering: B*, 114:130–134, 2004.

[9] J. B. Mitchell, J. Shewchun, D. A. Thompson, and J. A. Davies. Nitrogen-implanted silicon. II. Electrical properties. *Journal of Applied Physics*, 46(1):335–343, 1975.

[10] Y. Tokumaru, H. Okushi, T. Masui, and T. Abe. Deep levels associated with nitrogen in silicon. *Japanese Journal of Applied Physics*, 21(7A):L443, 1982.

[11] K. Nauka, M. S. Goorsky, H. C. Gatos, and J. Lagowski. Nitrogen-related deep electron traps in float zone silicon. *Applied Physics Letters*, 47(12):1341–1343, 1985.

[12] N. E. Grant, V. P. Markevich, J. Mullins, A. R. Peaker, F. Rougieux, D. Macdonald, and J. D. Murphy. Permanent annihilation of thermally activated defects which limit the lifetime of float-zone silicon. *Physica Status Solidi (a)*, 213(11):2844–2849, 2016.

[13] J. Mullins, V. P. Markevich, M. Vaqueiro-Contreras, N. E. Grant, L. Jensen, J. Jabłoński, J. D. Murphy, M. P. Halsall, and A. R. Peaker. Thermally activated defects in float zone silicon: Effect of nitrogen on the introduction of deep level states. *Journal of Applied Physics*, 124(3):035701, 2018.

[14] M. Nakamura, S. Murakami, and H. Udono. Origins of the nitrogen-related deep donor center and its preceding species in nitrogen-doped silicon determined by deep-level transient spectroscopy. *Applied Physics Express*, 12(2):021005, 2019.

[15] D. Hiller, V. P. Markevich, J. A. T. De Guzman, D. König, S. Prucnal, W. Bock, J. Julin, A. R. Peaker, D. Macdonald, N. E. Grant, and J. D. Murphy. Kinetics of bulk lifetime degradation in float-zone silicon: Fast activation and annihilation of grown-in defects and the role of hydrogen versus light. *Physica Status Solidi (a)*, 217(17):2000436, 2020.

[16] R. Sauer, J. Weber, and W. Zulehner. Nitrogen in silicon: Towards the identification of the 1.1223-eV (A,B,C) photoluminescence lines. *Applied Physics Letters*, 44(4):440–442, 02 1984.

[17] H. J. Stein. Vibrational absorption bands for implanted nitrogen in crystalline silicon. *Applied Physics Letters*, 43(3):296–298, 08 1983.

[18] H. J. Stein. Infrared absorption band for substitutional nitrogen in silicon. *Applied Physics Letters*, 47(12):1339–1341, 12 1985.

[19] L. Scheffler, A. Lei, S. Duun, and B. Julsgaard. On the nature of thermally activated defects in n-type FZ silicon grown in nitrogen atmosphere. *AIP Advances*, 12(3):035151, 2022.

[20] K. L. Brower. Jahn-Teller-distorted nitrogen donor in laser-annealed silicon. *Physical Review Letters*, 44(24):1627, 1980.

[21] K. L. Brower. Deep-level nitrogen centers in laser-annealed ion-implanted silicon. *Physical Review B*, 26(11):6040, 1982.

[22] M. Belli, M. Fanciulli, and D. Batani. Electron spin resonance of substitutional nitrogen in silicon. *Physical Review B*, 89:115207, Mar 2014.

[23] K. Murakami, K. Masuda, Y. Aoyagi, and S. Namba. Experimental tests of non-thermal effect for pulsed-laser annealing by time-resolved reflectivity and EPR measurements. *Physica B+C*, 116(1-3):564–569, 1983.

[24] H. A. Jahn and E. Teller. Stability of polyatomic molecules in degenerate electronic states-I—orbital degeneracy. *Proceedings of the Royal Society of London. Series A-Mathematical and Physical Sciences*, 161(905):220–235, 1937.

[25] H. P. Hjalmarson, P. Vogl, D. J. Wolford, and J. D. Dow. Theory of substitutional deep traps in covalent semiconductors. *Physical Review Letters*, 44:810–813, Mar 1980.

[26] G. G. DeLeo, W. B. Fowler, and G. D. Watkins. Theory of off-center impurities in silicon: substitutional nitrogen and oxygen. *Physical Review B*, 29(6):3193, 1984.

[27] K. Murakami, H. Itoh, K. Takita, and K. Masuda. Substitutional nitrogen impurities in pulsed-laser annealed silicon. *Applied Physics Letters*, 45(2):176–178, 1984.

[28] K. Murakami, H. Kuribayashi, and K. Masuda. Motional effects between on-center and off-center substitutional nitrogen in silicon. *Physical Review B*, 38(2):1589, 1988.

[29] V. V. Voronkov and R. Falster. Out-diffusion of deep donors in nitrogen-doped silicon and the diffusivity of vacancies. *Journal of Applied Physics*, 112(1):013519, 2012.

[30] H. Itoh, K. Murakami, K. Takita, and K. Masuda. Charge-state changes of substitutional nitrogen impurities in silicon induced by additional impurities and defects. *Journal of Applied Physics*, 61(10):4862–4868, 1987.

[31] H. P. Hjalmarson and D. R. Jennison. Investigation of off-center substitutional N in Si. *Physical Review B*, 31(2):1208, 1985.

[32] C. Cunha, S. Canuto, and A. Fazzio. Role played by N and NN impurities in type-IV semiconductors. *Physical Review B*, 48(24):17806, 1993.

[33] M. Saito and Y. Miyamoto. Atomic and electronic structures of the N substitutional impurity in Si. *Physical Review B*, 56(15):9193, 1997.

[34] H. Sawada and K. Kawakami. First-principles calculation of the interaction between nitrogen atoms and vacancies in silicon. *Physical Review B*, 62(3):1851, 2000.

[35] J. A. Verges. A simple tight-binding model for deep impurity levels: application to the Jahn-Teller-distorted nitrogen donor in silicon. *Journal of Physics C: Solid State Physics*, 14(4):365, 1981.

[36] J. P. Goss, I. Hahn, R. Jones, P. R. Briddon, and S. Öberg. Vibrational modes and electronic properties of nitrogen defects in silicon. *Physical Review B*, 67(4):045206, 2003.

[37] Z. Zhu, H. Shao, X. Dong, N. Li, B.-Y. Ning, X.-J. Ning, L. Zhao, and J. Zhuang. Electronic band structure and sub-band-gap absorption of nitrogen hyperdoped silicon. *Scientific Reports*, 5(1):10513, 2015.

[38] A. Platonenko, F. S. Gentile, F. Pascale, A. M. Ferrari, M. D'amore, and R. Dovesi. Nitrogen substitutional defects in silicon. a quantum mechanical investigation of the structural, electronic and vibrational properties. *Physical Chemistry Chemical Physics*, 21(37):20939–20950, 2019.

[39] L. Giacomazzi and P. Umari. First-principles investigation of electronic, structural, and vibrational properties of a-Si_3N_4. *Physical Review B*, 80:144201, Oct 2009.

[40] D. Skachkov, W. R. L. Lambrecht, H. J. Von Bardeleben, U. Gerstmann, Q. D. Ho, and P. Deák. Computational identification of Ga-vacancy related electron paramagnetic resonance centers in β-Ga_2O_3. *Journal of Applied Physics*, 125(18):185701, 05 2019.

[41] L. Giacomazzi, L. Martin-Samos, and N. Richard. Paramagnetic centers in amorphous GeO_2. *Microelectronic Engineering*, 147:130–133, 2015. Insulating Films on Semiconductors 2015.

[42] P. A. Schultz and R. P. Messmer. Valence-bond theory of off-center impurities in silicon: Substitutional nitrogen. *Physical Review B*, 34(4):2532, 1986.

[43] P. Rinke, A. Janotti, M. Scheffler, and C. G. Van de Walle. Defect formation energies without the band-gap problem: Combining density-functional theory and the GW approach for the silicon self-interstitial. *Physical Review Letters*, 102(2):026402, 2009.

Chapter 5

Unraveling spectroscopic fingerprints of the NV pair in Si: similarities with other *E*-centers

Contrary to the substitutional nitrogen center, little to no spectroscopic evidence is decisively attributed to the nitrogen-vacancy complex (NV). Some EPR and DLTS signals have been tentatively attributed to this center, yet the computation of the spectroscopic signature of the defect has not previously been carried out. Furthermore, activation energies obtained from deep-level transient spectroscopy are often assigned to a subset of possible defects that include non-equivalent atomic structures, such as the substitutional nitrogen and the nitrogen–vacancy complex. The aim of this chapter is to clarify the spectroscopic fingerprints of the NV center by performing state of the art first principles calculations grounded in symmetry considerations, *i.e.* guided by a Jahn-Teller model. A review of the literature on the spectroscopic data linked with the presence of nitrogen and vacancies in silicon is presented in Section 5.1. The methods developed in previous chapters are employed to model the NV pair and establish its model structure. As this defect shares equivalent atomic structure as the silicon *E*-center (PV, AsV, SbV), its symmetry-breaking mechanism is linked to the Jahn-Teller effect observed in these systems. Section 5.2 presents *ab initio* calculations elucidating the fundamental structural and electronic properties of the NV pair, along with its energy landscape. The unique characteristics of this complex, such as the displacement of the N impurity into an off-center position akin to the substitutional impurity, are emphasized in comparison to other *E*-centers (particularly PV). EPR parameters and CTLs are provided to assist forthcoming experimental endeavours aimed at identifying the signature of the NV complex in Si. Section 5.3 concludes by establishing a clear differentiation between properties of the substitutional impurity and the NV pair. This clarification addresses past ambiguities, particularly in attributing certain properties, such as thermodynamic CTLs, to these centers.

5.1 The NV complex in silicon

The family of defect complexes containing Si vacancies and N atoms, referred to as V_xN_y centers, have gained some interest in recent years in particular in the field of photovoltaics. A dramatic degradation of minority carrier lifetime was observed in float-zone silicon grown in nitrogen ambient and thermally treated in the $400-800°C$ range [1–3]. It has been shown that this effect is related to the presence of electrically active traps introduced in the material band gap by these V_xN_y centers [4–6]. This degradation effect greatly reduces solar cells efficiency and thus a deep understanding of these defects and their microscopic interactions is essential. A consequent number of DLTS studies [2,4–9] have been performed in order to characterise the deep levels generated, however no defect structure was identified. These works report a variety of levels which differ in number, position and intensity depending on samples, experimental conditions and treatments (Table 5.1). In particular, two of these levels $\epsilon_{CBM}-0.33-0.34$ eV and $\epsilon_{CBM}-0.64-0.65$ eV were linked with the degradation [5] and were shown to be two states, a double acceptor and an acceptor respectively, of the same defect [8]. On the other hand, they were tentatively attributed to both the substitutional nitrogen [8] and the NV complex [6], emphasizing the necessity to properly characterise spectroscopic properties of both defect centers. The perplexing nature of the attribution of a set of levels to defects with a different number of components in their structure is further enhanced by the structure designation method introduced some years ago [10–12]. In this approach, a substitutional component, such as N_{Si}, is equated to the recombination of a silicon vacancy with an interstitial nitrogen impurity and is thus also denoted as V_1N_1. This notation is believed to be source of some confusion for N_{Si}, or V_1N_1, and the NV pair to be thought of as one and the same defect, as is believed to be the case in Refs. [8,9].

Tab. 5.1: DLTS activation energies of traps located within the band gap of N-doped float-zone Si as reported in [2,4–6,8]. The typical error provided for measurements is ±0.01eV, therefore values within this uncertainty are tentatively combined. All levels are given from the conduction band minimum in eV.

Level	**Reference**
0.16-0.17	[2,5,6,8]
0.18	[4]
0.20-0.21	[2,5,6,8]
0.28	[2,6,8]
0.33-0.34	[4–6,8]
0.356	[2]
0.39	[6]
0.64-0.65	[5,6,8]

Contrary to the substitutional nitrogen, there is no clear experimental evidence of the NV center in silicon from EPR measurements, despite very accurate low temperature studies of

N-doped samples [13, 14]. On the other hand, other N-related defects spectra were recorded together with the SL5 spectrum [13]. In particular, the SL6 spectrum, which has not yet been attributed to a defect structure, is formed under similar conditions as the SL5 spectrum. The intensity of this center however increases after the SL5 center is annealed out, above 400°C. It was reported to contain a N impurity within a defect structure with C_{3v} symmetry. The main characteristics of the SL6 spectrum were reported with $g_{\parallel} = 2.0018$, $g_{\perp} = 2.0085$ and a hfi structure characterised only for the N impurity with $A_{\parallel} = 23.4$ MHz, $A_{\perp} = 19.2$ MHz. The hfi intensity is smaller than for the SL5, suggesting a weaker electron density (*i.e.* a weaker s component) on the impurity. This, coupled with the higher temperature stability of the defect, suggests that the defect is very similar to the SL5 center, but is larger (*i.e.* contains more atomic components). Moreover, through a study of motional effects with temperature on the spectrum linewidth, the authors determined that this defect likely corresponds to a combination of a substitutional N with another intrinsic defect. The presence of another impurity has been discounted as no change in the spectrum was observed when implanting samples with C or O.

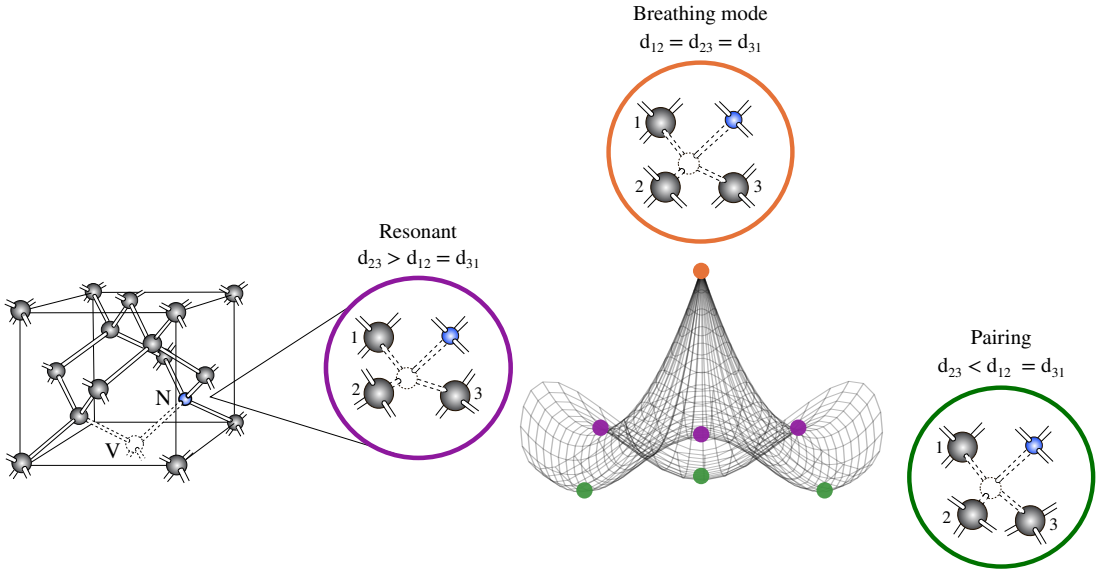

Fig. 5.1: Schematic representation of the Jahn-Teller effect in the neutral nitrogen-vacancy complex in Si, NV^0. In green, purple and orange circles, pairing (p), resonant (r) and breathing mode configurations are represented along the nitrogen-vacancy axis. The difference between the structures lies in the characteristic Si_2-Si_3 bond distance. The geometries are placed on the potential energy surface model for the *E*-center as established in [15, 16].

A later DFT study of multiple N-related defects in silicon [17] has tentatively assigned this spectrum to the NV center, but this attribution remained unclear as only indirect evidence (binding energy and spin density) was provided. This study also predicts single and double acceptor levels for NV at $\epsilon_{CBM} - 0.7$ eV and $\epsilon_{CBM} - 0.5$ eV respectively. The authors however caution a possible failing of their method in calculating these levels as they are so close together.

The assumption in this work, as in previous studies, is that the NV complex corresponds to

a substitutional N impurity (in blue in Fig. 5.1) next to a Si vacancy (dashed circle in Fig. 5.1). This atomic structure is analogous to a well studied defect in doped silicon, the *E*-center, introduced in Section 3.1. The aim of this section is not to provide an extensive review of the literature concerning the *E*-center, as that has been done previously [15], and only a summary of the results relevant to this study is provided below. EPR measurements unveiled the presence of this center in irradiated silicon [18, 19], with a defect structure composed of a group-V impurity (phosphorus, arsenic or antimony) next to a silicon vacancy. It was then postulated, and confirmed by further experiments [20] and later calculations [15, 16, 21–24], that the *E*-center in neutral charge state (PV^0, AsV^0, Sb^0) follows a Jahn-Teller (JT) effect, illustrated in Fig. 5.1. This effect is characterised by the symmetry breaking of a high symmetry C_{3v} structure, denoted as a breathing configuration (in orange in Fig. 5.1), into a lower symmetry C_s configuration. This distortion breaks the degeneracy of a partially filled electronic doublet located in the band gap of the breathing configuration, lowering the overall energy of the system. Recently, a model of the *E*-center was developed based on symmetry considerations [15, 16] in which its defect structure is characterised by a trimer formed by the vacancy first Si neighbours ($Si_1 - 3$ in Fig. 5.1). In the breathing structure, all three Si – Si distances (d_{12}, d_{23} and d_{31}) in the trimer are perfectly equal, whereas in the distorted C_s configuration one of the distances (*e.g.* d_{23}) is different than the others. This leads to two senses of the JT distortion with either a pairing configuration (in green) in which the characteristic distance is shortened, or a resonant configuration (in purple) where it is elongated. Within this JT model, the PES of the NV center is proposed to have the shape of a Mexican hat. Moreover, this PES is characterised by three degenerate minima and three degenerate saddle points. Furthermore, the high-symmetry breathing configuration is found at the top of the PES.

Recent works dedicated to the characterisation of the *E*-center however rarely consider the NV pair and focus on other group-V impurity complexes. This can be attributed (among other reasons), as detailed in Section 1.1.2 and throughout this section, to challenges in accurately controlling nitrogen diffusion in silicon, the complex electrical characteristics of samples when nitrogen is employed as a dopant, and the singular difficulties in clearly characterising specific defect centers in samples such as the NV pair whereas other *E*-centers are quite easily observed and well understood. Consequently, this system is less significant for wide range industrial applications, and therefore receives less research attention. This results in an unclear picture of fundamental properties of the defect ground state, in particular with respect to other *E*-centers, and to very little established spectroscopic signals related to this complex.

5.2 *Ab initio* spectroscopic properties of the NV complex in silicon

As mentioned previously, assigning deep levels within the band gap to a particular defect structure poses a significant challenge. In the context of N-related defects in silicon, there has been some ambiguity regarding the source of specific levels, whether they originate from the substitutional nitrogen or the nitrogen-vacancy complex [8, 9]. Given that the NV center follows the same JT effect as the other *E*-centers, the fundamental properties of NV are compared with

those for the PV complex. In order to guide experimental scientists and solve the uncertainties concerning the levels in the gap of N-doped silicon, the CTLs are calculated. Furthermore, the EPR parameters for this defect are also determined, in an effort to identify the origin of other EPR spectra related to the nitrogen impurity (such as the so-called SL6 center).

5.2.1 The symmetry breaking in NV: Jahn-Teller effect

As expected from previous studies and symmetry considerations [15, 16, 21], the neutral NV complex (NV^0) exhibits similar symmetry and distortion as other *E*-center systems (PV, AsV, SbV), and the different configurations of this system (pairing, resonant, breathing) are stationary points of the Mexican hat shaped PES (Fig. 5.2a). Based on the calculations performed in this study, the defect in neutral charge state (NV^0) presents a C_s symmetry, and its ground state geometry is indeed in a distorted *pairing* configuration. The distortion results in a trimer formed by the vacancy nearest neighbours, for which one characteristic distance (Si_2-Si_3 in Fig. 5.2a) is shortened to 3.07 Å, while the other two distances are 3.62 Å. One Si_i-N distance between the N impurity and the vacancy first Si neighbours is therefore slightly elongated to 4.40 Å and the remaining two equivalent shortened to 4.24 Å. On the other hand, there is little variation on the positions of the three Si nearest neighbours to the impurity (Si_N), for which the N-Si_N bond length of 1.85 Å is the same as that of substitutional nitrogen (1.86 Å). These distances are consistent with previous estimates for both the *E*-center (as evidenced in Table 5.2) and the substitutional nitrogen center. It is interesting to note that the presence of a vacancy seems to have only little effect on the displacement of the N atom with respect to its first neighbours, compared to the substitutional defect, as the distance between the impurity and the plane defined by the three nearest silicon Si_N is identical for both centers (0.25 Å). Therefore, even when forming a complex with a vacancy, the N impurity resides in an off-center position, as is the case in N_{Si}^0. This result highlights the major difference of NV with respect to other *E*-centers, in which the impurity remains in an on-center position [16]. On the other hand, in the *resonant* configuration, the characteristic Si_2-Si_3 bond is elongated to 3.66 Å and the other two shortened to 3.36 Å, again in alignement with values obtained for PV (Table 5.2). Consequently, the N-Si_i distances are altered as well, as one alone is 4.23 Å and the other two are 4.32 Å.

Tab. 5.2: Calculated bond distances for the pairing and resonant configurations of NV^0 and PV^0.

Config.	**NV^0** (Å)	**PV^0** (Å)
Pairing	3.07	2.99
	3.62	3.62
Resonant	3.36	3.31
	3.66	3.66

To establish that this center presents a JT distortion as other *E*-centers, its electronic

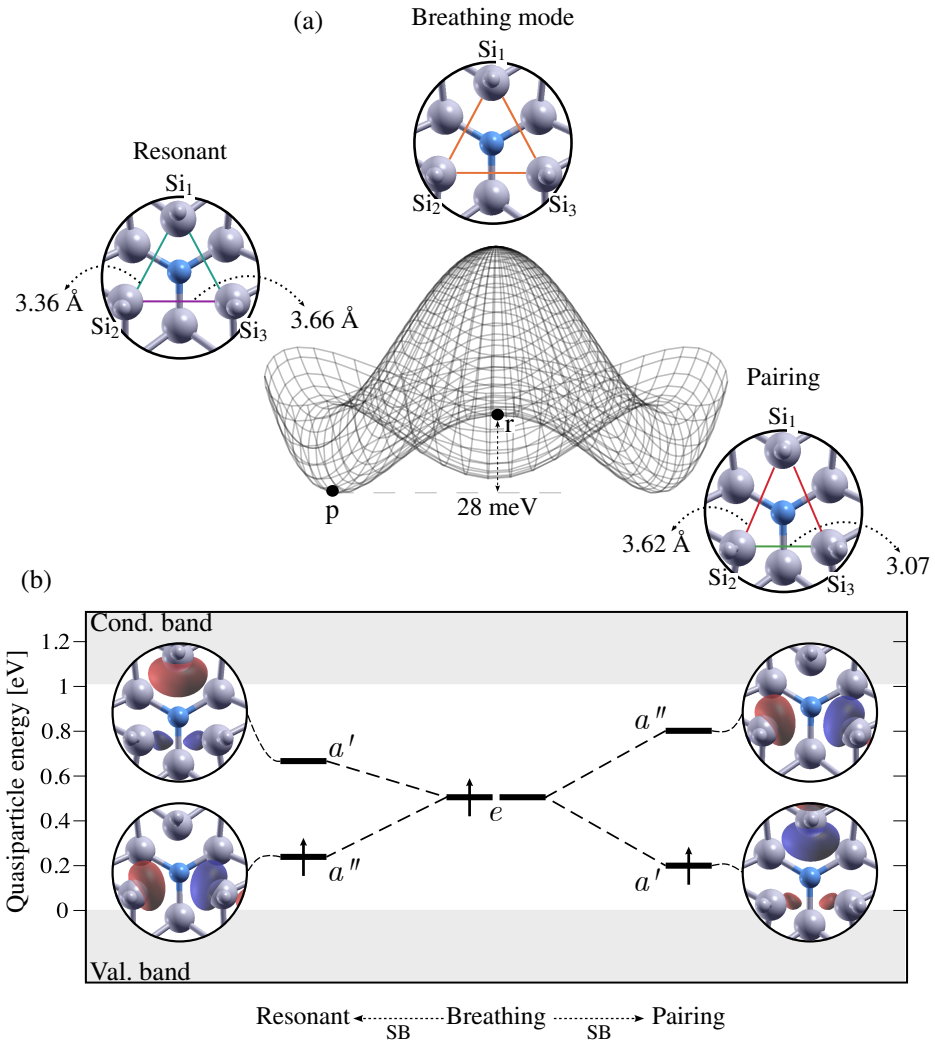

Fig. 5.2: *Ab initio* characterisation of the Jahn-Teller effect in the neutral nitrogen-vacancy complex (NV^0). (a) Relaxed defect structures depicting nitrogen (blue) and the vacancy nearest neighbours for the breathing, pairing (p) and resonant (r) configurations. Interatomic distances between the three vacancy closest neighbours (Si_{1-3}) are displayed. The geometries are represented along the *E*-center PES which shows the energy difference between pairing and resonant. At the top of the PES lies the Breathing mode configuration which is not a stationary point of the PES. To obtain the total energy of this structure, a relaxation at the +1 charge state, which stabilises in the undistorted C_{3v} configuration, is performed, followed by a single point calculation of the neutral charge state configuration. (b) Quasiparticle (QP) energies (computed at the GW level) of defect-induced states estimated at Γ for a 216 atoms SC for the breathing configuration and the symmetry-breaking (SB) resulting in the pairing and resonant states. Kohn–Sham (KS) energies and wavefunctions of defect states estimated at Γ are represented with respect to the valence band maximum and the conduction band minimum for the spin-up channel. Defect states introduced by the vacancy are labelled according to their irreducible representation and wavefunctions corresponding to the fully and partially occupied singlet states are shown.

structure is characterised and the corresponding one-electron defect states within the band gap are presented in Fig. 5.2b for the high symmetry breathing structure as well as for the two senses of the symmetry-breaking, *i.e.* pairing and resonant. The paramagnetic electron in the high symmetry breathing configuration, *i.e.* before distortion, is contained within a doublet e state, which therefore undergoes a JT distortion. The resulting symmetry breaking leads to a splitting of these levels into two singlet a defect states in the distorted C_s configurations. The one-electron wavefunctions are approximated using Kohn–Sham eigenfunctions and their corresponding energy levels using quasiparticle (Kohn–Sham) eigenvalues computed at Γ. The unpaired electron is located in a singlet defect state located 0.20 (0.16) eV and 0.23 (0.21) eV from the VBM for the pairing and resonant configurations respectively. The symmetry of these states and their corresponding wavefunctions however is different between the two senses of the distortion, as depicted in Fig. 5.2b. The paramagnetic state is an a' state in the pairing configurations, which corresponds to a wavefunction mainly localised on one of the Si neighbours (Si_1 in Fig. 5.2b) and in a smaller degree on the other two nearest Si atoms. On the other hand, the paramagnetic a'' state of the resonant distortion is characterised by a wavefunction that extends only over two of the nearest silicon neighbours. The second level arising from the e doublet lies 0.79 (0.53) eV and 0.68 (0.45) eV above the VBM for the pairing and resonant configurations respectively, and their wavefunctions have respectively a'' and a' symmetry. The positions of the defect levels within the band gap are very close to those of PV^0, recorded in Table 5.3 with Kohn-Sham energies, which are located 0.17 eV and 0.56 eV from the VBM for the pairing structure, and 0.22 eV and 0.47 eV from the VBM for the resonant configuration. Similarly, the symmetry of the corresponding wavefunctions are in agreement between the two complexes. This result highlights the similarities in the electronic structure of the defects.

Tab. 5.3: Calculated one-electron defect states for the pairing and resonant configurations of NV^0 and PV^0. The levels, reported as Kohn-Sham eigenvalues, are referenced to the valence band maximum.

Config.	**NV^0(eV)**	**PV^0(eV)**
Pairing	0.16	0.17
	0.53	0.56
Resonant	0.21	0.22
	0.45	0.47

Similarly to what is observed for N_{Si}, the band structures displayed in Fig. 5.3 for both pairing and resonant configurations of NV, show that the dispersion of the defect states due to the addition of more k-points to sample the BZ is significant. Both structures are close, the major difference being in the shift observed in the spin up contribution of the defect states located within the band gap. The dispersion effect is therefore similar in both pairing and resonant configurations, and more pronounced for the spin up for all defect states. Furthermore, multiple crossing of the spin up and down of the highest occupied state are observed between high-symmetry points X and U, as well as between the spin down contributions of the highest occupied and lowest unoccupied states around the Γ point. Although in this case the dispersion

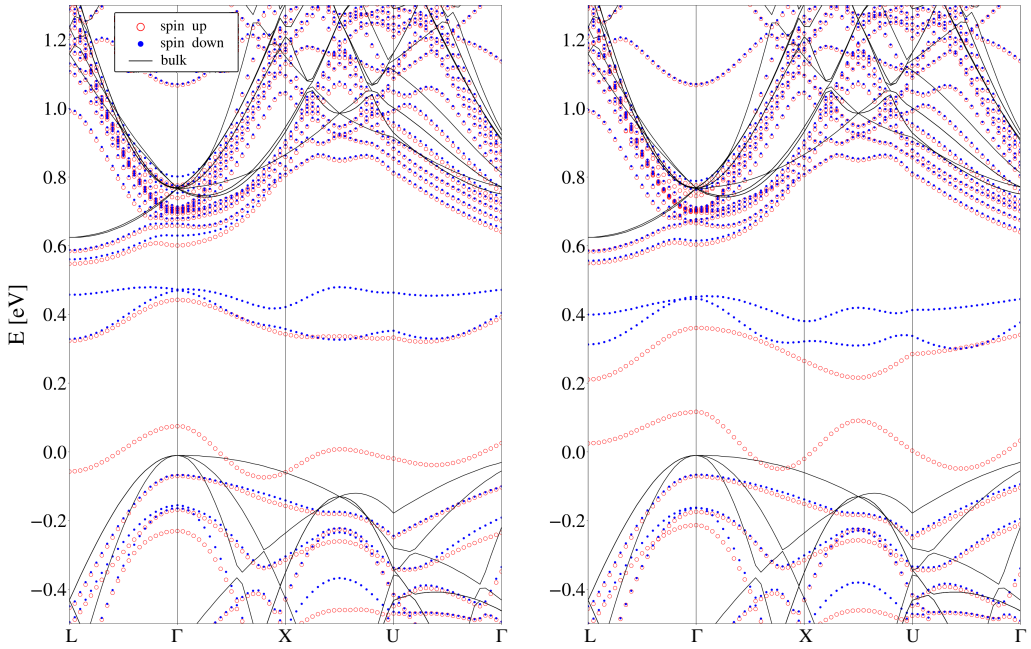

Fig. 5.3: Band structures of nitrogen-vacancy complex in 216-atom cells from standard PBE calculations. Kohn-Sham eigenvalues for the pairing (left) and resonant (right) configurations are shown. Spin up *versus* spin down contributions are represented in red and blue respectively. The eigenvalues corresponding to the pristine cell are depicted in black. The zero energy corresponds to highest occupied Kohn-Sham eigenvalue in the pristine cell (or the top of the valence band).

does not have as critical an impact as that found in N_{Si} (*i.e.* the negative band gap shown in Fig.4.3), this demonstrates that the results reported in this study provide a qualitative picture of basic ground state properties for this category of defects. However, more refined methods are required in order to obtain more accurate and predictive characteristics, as has been done previously [15, 16, 21].

Thus the neutral NV^0 center exhibits similar electronic structure and JT distortion as other *E*-center defects. Its PES therefore corresponds to that determined in the case of the JT Effect [21], *i.e.* the so-called Mexican hat shaped PES, as is depicted in Fig. 5.2a, for which the breathing mode configuration $\mathcal{B}$ is located at the top. Lower in energy, the three equivalent ground states in pairing configuration are found as minima of the surface. They each correspond to the three possible distortions in which one of the characteristic Si_2-Si_3 bond length is shorter than the other two (Fig. 5.2a). Between these structures, three degenerate saddle points correspond to the three resonant structures, obtained for one characteristic distance longer than the other two. The corresponding energy difference between pairing and resonant configurations is 28 meV, which is comparable to k_BT at room temperature. As such, the barrier between pairing and resonant configurations can be overcome and thus, the defect can reorient. This value is consistent with estimations and measurements for other group V impurity-vacancy complexes [16, 18, 19, 22] which are included in Table 5.4. The breathing configuration shown in Fig. 5.2 is not a stationary point on the PES and therefore, does not represent a real

stable structure. Instead, it necessarily distorts into a C_s structure. This configuration is an idealised representation, and the corresponding doublet state is merely indicative of the JT distortion. Nevertheless, an estimation of the total energy for this ideal structure indicates that it sits $\sim 90-100$ meV higher than the pairing configuration. This finding aligns with the E-center PES model, confirming that the idealised structure cannot be the ground state. It also contradicts previous suggestions that the JT distortion in the NV complex is weak [17].

Tab. 5.4: Energy difference between pairing and resonant configurations of group-V impurity-vacancy complexes in neutral charge state. The values obtained in this work for NV^0 (tw) are compared with previous calculations for PV^0, AsV^0 and SbV^0 [16, 22]. Experimental data [18, 19] for PV and AsV are also reported for reference.

Ref.	**NV^0(meV)**	**PV^0(meV)**	**AsV^0(meV)**	**SbV^0(meV)**
tw	28		-	-
[22]	-	-	20	-
[16]	-	36	31	28
[18, 19]	-	60-70	70	-

Size effects have been shown to matter for E-centers, notably for SbV [16]. The calculations presented in this study have then been repeated for both pairing and resonant configurations using a 512-atoms cell in order to investigate these effects. The energy difference between pairing and resonant structures increases to 33 meV using the 512-atoms cell, meaning that the energy is converged within 5 meV for NV between the 216- and 512-atoms supercell. The interatomic distances on the other hand decrease when increasing the supercell size, but remain close in both cell, with the largest difference of 0.07 Å in both pairing and resonant configurations. This is consistent with what is found for N_{Si} in Section 4.2.1, and suggests that size effects are not as considerable in this system as in larger impurities-containing complexes.

5.2.2 Elucidating spectroscopic properties of the NV complex in Si

The ground state of NV corresponds to the E-center, therefore more advanced properties such as EPR parameters and CTLs are likely to follow similar trends as other E-centers. These parameters are then computed and provided in Tables 5.5 and 5.6. Since there is no direct experimental evidence specifically attributed to the NV complex, the results are compared with previous experimental measurements for another group-V impurity complex, the phosphorus-vacancy pair PV. The accuracy of the results is also tested by comparison with theoretical estimations for PV, conducted in this study using the same calculation parameters employed for NV. Concerning EPR parameters, computed values of $\overleftrightarrow{g}$ and hfi $\overleftrightarrow{A}$ tensors for both pairing and resonant configurations are presented in Table 5.5. The relevant contributions for E-centers to the hfi signature include the impurity and the three vacancy closest neighbours, two of which are equivalent. Similarly as for N_{Si}, this center possesses a symmetry plane along the nitrogen-vacancy axis, leading to a near-axial symmetry of the principal values of the $\overleftrightarrow{g}$

and hyperfine $\overleftrightarrow{A}$ tensors. This results in a main value g/A_1 parallel to this plane and two slightly different $g/A_{2,3}$ values perpendicular to it.

The lack of experimental data pertaining to this defect results in a qualitative analysis of the values calculated in this study and presented in Table 5.5. In this regard, the estimates for the pairing (tw-p) configuration are in better agreement with the trends observed in other *E*-center systems than those of the resonant structure (tw-r). The ordering of the main values of the $\overleftrightarrow{g}$-tensor measured by EPR measurements of PV [18] is as follow: the value parallel to the vacancy-dopant axis, g_1, is very close to 2.00 and the other two components, g_2 and g_3, are respectively slightly above and below 2.01. This distribution is observed in the pairing but absent in the resonant. Furthermore, the isotropic value g_{iso} of 1.9980 in the resonant is much too small, whereas that of the pairing, 2.0055, is more consistent with the values recorded for PV both measured and calculated of 2.0071 and 2.0068 respectively. On the other hand, the hyperfine structure exhibits a substantial difference between the pairing and resonant configurations. In each case, the main $\overleftrightarrow{A}$ values of the single Si ($^{29}Si_1$) and the two equivalent Si ($^{29}Si_2$ and $^{29}Si_3$) are in concordance with their corresponding electronic structures (as illustrated with the wavefunctions in Fig. 5.2b). In other words, the pairing has the largest hfi contribution for Si_1 on which the electron density is mostly localised and a smaller contribution for $Si_{2,3}$ where the density is less prominent, whereas this is inverted in the resonant following the change in electronic density. In both cases the contribution of the N atom is almost non-existent, reflecting that the unpaired electron is not localised on the impurity at all, as it is so withdrawn from the vacancy. In the case of PV, the impurity remains in an on-center position, close to the vacancy site, and thus retains more of the electron density. Again, the pairing configuration is in better agreement with measurements and estimates for PV as the largest contribution of the hfi tensor is on Si_1. As for the $Si_{2,3}$ contribution, only the isotropic value was recorded for the PV spectrum. Nevertheless, the obtained isotropic value in this investigation aligns with the experimental measurement and remains sufficient for distinguishing between the two potential structures. Specifically, the isotropic value for the pairing (–60.9 MHz) is rather consistent with measurements for PV, whereas that of the resonant (–308.4 MHz) is too large by one order of magnitude.

The calculations of EPR parameters for the NV center in silicon therefore provide, through direct comparison with experiments and previous calculations, *e.g.* for PV, an unequivocal proof that the ground state of the NV complex, and by extension of *E*-center defects in Si, is in a pairing configuration. Furthermore, they provide a basis to guide the identification of the EPR spectrum of this defect. In particular, the parameters presented in Table 5.5 can be compared to those reported for the SL6 center [13], which has been tentatively assigned to the NV center [17]. Firstly, it seems unlikely that the SL6 spectrum could be attributed to the NV center, due to different symmetries. The SL6 spectrum exhibits C_{3v} symmetry, while the NV center possesses C_s symmetry. This leads to a difference in the symmetries of the EPR parameters themselves. The parameters of the SL6 spectrum display an axial symmetry whereas those for the NV center have a *near*-axial symmetry for the $\overleftrightarrow{g}$-tensor and the impurity contribution of the $\overleftrightarrow{A}$-tensor. By comparing the computed values with the measurements of the SL6 center for the hfi component on the impurity, it is possible to establish that these two systems are incompatible. The calculations show that the spin density on the impurity is negligible, for both the pairing (A_{iso} = 0.49 MHz) and resonant (A_{iso} = 0.16 MHz) configurations, whereas

Tab. 5.5: EPR parameters of nitrogen impurity-vacancy complex in silicon for both pairing (tw-p) and resonant (tw-r) configurations. The estimated $\overleftrightarrow{g}$ and hyperfine $\overleftrightarrow{A}$ tensors for the N atom (impurity) and the three vacancy nearest Si neighbours ($^{29}Si_i$) are reported, two of which ($^{29}Si_2$ and $^{29}Si_3$) are equivalent. No direct EPR spectrum was associated to this center, the values are compared with data for the phosphorus-vacancy complex, both computed with the same method as NV (tw-PV) and measured [18]. Values for the SL6 center are also included [13].

	$\overleftrightarrow{g}$				$\overleftrightarrow{A}$ ($^{29}Si_1$) (MHz)				$\overleftrightarrow{A}$ ($^{29}Si_{2,3}$) (MHz)				$\overleftrightarrow{A}$ (impurity) (MHz)			
Ref.	$\mathbf{g_1}$	$\mathbf{g_2}$	$\mathbf{g_3}$	$\mathbf{g_{iso}}$	$\mathbf{A_1}$	$\mathbf{A_2}$	$\mathbf{A_3}$	$\mathbf{A_{iso}}$	$\mathbf{A_1}$	$\mathbf{A_2}$	$\mathbf{A_3}$	$\mathbf{A_{iso}}$	$\mathbf{A_1}$	$\mathbf{A_2}$	$\mathbf{A_3}$	$\mathbf{A_{iso}}$
tw-p	1.9996	2.0101	2.0069	2.0055	–466.3	–316.0	–315.8	–366.0	–67.0	–58.6	–57.0	–60.9	0.87	0.33	0.27	0.49
tw-r	2.0060	1.9956	1.9923	1.9980	46.7	27.8	27.3	33.9	–369.5	–278.8	–277.0	–308.4	–0.13	0.36	0.24	0.16
SL6 [13]	2.0018	2.0085	2.0085	-	-	-	-	-	-	-	-	-	23.4	19.2	19.2	20.6
tw-PV	1.9997	2.0123	2.0085	2.0068	–476.2	–322.3	–322.1	–373.5	–49.8	–43.9	–42.4	–45.4	32.7	27.6	27.5	29.3
PV ([18])	2.0005	2.0112	2.0096	2.0071	449.7	295.3	295.3	–346.9	-	-	-	–37.2	31.7	26.2	25.9	27.9

the SL6 center displays non-zero contribution ($A_{\parallel}$ = 23.4 MHz, $A_{\perp}$ = 19.2 MHz). Therefore, the SL6 center can not be attributed to the NV center in silicon.

As established in Section 5.1, there has been some confusion in more recent works on electrical activity of N-doped Si [8, 9]. Different sets of DLTS activation energies have been attributed to the *NV center in silicon*, cited as both the off-center substitutional nitrogen and the nitrogen-vacancy complex. To solve the uncertainties on the nature of deep levels in N-doped Si, the CTLs for the NV complex are determined and compared with those previously estimated for N_{Si}. As for N_{Si}, the relative stability of NV^0 with respect to charge states +1, –1 and –2 is investigated in order to compute the corresponding CTLs. From the present *ab initio* calculations, charge state +1, is found in a breathing configuration and charge states –1 and –2 in resonant configurations, in agreement with previous theoretical [15,16] and experimental [18, 19] studies on *E*-center defects. At charge state +1 the electron trap is empty, therefore no distortion takes place and the three characteristic Si_i-Si_i bonds are equal to 3.60 Å. For charge state –1, the a′ defect state is fully occupied, and for the –2 charge state the following a″ state in the band gap is partially occupied. In both cases the characteristic elongated bond length is equal to 3.56 Å and the other two shortened to 2.91 Å.

Tab. 5.6: Deep levels located within the band gap associated with NV in silicon. Thermodynamic CTLs are calculated within a standard PBE approximation (tw-PBE) and within the combined DFT and GW approach (tw-PBE+GW). Values are compared with activation energies for which the attribution to either N_{Si} or NV is unclear [8]. Other DLTS measurements associated to a defect complex for which the precise structure has not been resolved but containing N and vacancies [25] are also included. Finally, both DLTS and estimated levels for the phosphorus-vacancy complex (pw-PV, Exp. PV) are added for comparison [26], with CTLs computed using a standard PBE approximation, corrected with an empirical shift. The donor level is given with respect to the valence band maximum, and the acceptor and double acceptor levels are given from the conduction band minimum in eV.

Reference	$\mathbf{E_v + \epsilon(+/0)}$	$\mathbf{E_c - \epsilon(0/-)}$	$\mathbf{E_c - \epsilon(-/2-)}$
tw-PBE	0.17	0.43	0.23
tw-PBE+GW	0.27	0.38	-
Exp. [8]	-	0.64	0.34
Exp. [25]	-	0.43,0.40	-
pw-PV [26]	0.22	0.36	-
Exp. PV [26]	0.27	0.45	-

Calculated thermodynamic CTLs, obtained within the PBE+GW (PBE) approach, for the single donor, the single and double acceptor levels of NV are presented in Table 5.6. The band gap is estimated to be 1.01 (0.77) eV, consequently the donor level is low in the band gap at ϵ_{VBM}+0.27 (0.17) eV (or ϵ_{CBM}−0.75 (0.58) eV) and the single acceptor level is located close to mid-gap at ϵ_{CBM}−0.37 (0.43) eV. The double acceptor level is located at ϵ_{CBM}−0.08 (0.23) eV from the CBM, very close to the CB. Notably, due to the estimations of the error bars for

levels computed from electronic affinities, *i.e.* acceptor levels, with the PBE+GW method ($\sim$ 0.1 – 0.2 eV) [15], the NV complex in charge state –2 is considered thermodynamically unstable, and the corresponding level is not included in Table 5.6. The calculated CTLs are compared with DLTS activation energies assigned to the NV complex [25]. Only an acceptor level, located at 0.43 eV and 0.40 eV below the CB in Cz and FZ silicon respectively is reported, in good agreement with the value estimated using the PBE+GW method. Finally, concerning the set of levels reported in [8], (as detailed in Section 4.2.3) it seems unlikely for the defect responsible for this signal to be either the substitutional nitrogen or the nitrogen-vacancy pair. Calculations show that charge state –2 of NV is thermodynamically unstable, therefore this defect exhibits no double acceptor CTL either. Furthermore, the values reported in this thesis are in excellent agreement with both DLTS measurements and previous computations of CTLs for the PV complex, validating their accuracy. The signal reported in [8] is therefore most likely due to another nitrogen-related defect. It is also noted that previous DLTS measurements for *E*-centers reported difficulties in measuring the donor level [26], which may constitute an explanation for the lack of activation energy reported in N-doped silicon as well. Note that other sets of levels were also measured (see Table 5.1) and attributed to the general presence of N and vacancies in the defect however no discussion concerning the nature of the level (donor or acceptor) is provided. The values of $\epsilon_{\mathrm{CBM}} - 0.34$ eV and $\epsilon_{\mathrm{CBM}} - 0.64$ eV are most commonly found, yet as detailed above are unlikely due to the NV complex. The other commonly found values $\epsilon_{\mathrm{CBM}} - 0.16$ eV and $\epsilon_{\mathrm{CBM}} - 0.20$ eV, are located rather high in the gap which indicates that these levels originate from different defects. Furthermore, it has been shown that levels in this part of the gap are not directly linked with the observed lifetime degradation [5], suggesting that they appear more likely to arise from shallow traps. On the other hand, the computed single acceptor value is in excellent agreement with a level measured in a recent study of N-doped Si [6]. No level was reported deeper than 0.65 eV below the CB, likely due to similar difficulties in measuring donor levels of *E*-centers [26].

In summary, an analysis of fundamental properties of the nitrogen-vacancy complex in silicon, the so-called *E*-center, was performed. A systematic comparison with a model developed for other *E*-centers (PV, AsV, SbV) [15,16,21] was carried out in order to validate the findings. It is shown that this model can be extended to NV. In particular, a ground state in pairing configuration was found and its atomic and electronic properties are consistent with other *E*-center systems. This model was also further validated through calculations of EPR parameters, allowing direct comparison with experimental evidence. Since no EPR spectrum of NV has been identified yet, the comparison was established with respect to spectra and calculations for PV, obtained using the same method as for NV. The calculated parameters are consistent with the previously reported values and in very good agreement with data for PV. In order to fully assess the accuracy of the current method in describing paramagnetic properties of *E*-center systems, it is necessary to compute EPR parameters for other complexes, *i.e.* AsV, SbV. Although this would provide quantitative estimations of the errors and trends that depend on the impurity species, such an endeavor is not within the scope of this work and may be considered for future investigation. Nevertheless, the results obtained for N_{Si} and PV being encouraging in their accuracy with respect to their respective experimental evidence, we reiterate that the values presented for NV provide a solid basis to guide the identification of the EPR spectrum of this

defect. Finally, different charge states of NV were characterised and thermodynamic CTLs calculated in order to resolve uncertainties regarding the origin of the electrical activity of N-doped Si. The estimated single acceptor levels allow to identify promising agreement with one set of activation energies attributed to NV [25]. Furthermore, both single donor and acceptor levels show excellent concordance with previous calculations and measurements obtained for PV [26], validating the accuracy of the method employed throughout this thesis. Regarding the tentative attribution of the NV complex to the SL6 center, the results presented in this work show undoubtedly that this defect is not compatible with the EPR measurements. A possible future pursuit for this work would be to characterise spectroscopic properties of various N-related defects in order to identify the origin of the SL6 signal. Some promising candidates include the N_3V complex and the di-substitutional which have been shown to have C_{3v} symmetry [27]. Another interesting family of defects to explore is the NV_n group (*i.e.* NV_2, NV_3) which have not previously been characterised. Applying the methodology used in this work on these defects may allow to identify which defect is responsible for the SL6 signal. The data presented can therefore be used as starting point to guide the identification of the NV complex in future experimental campaigns. Finally, with this study of the NV complex in Si, it was confirmed that this defect indeed exhibits similar properties as other *E*-center. In particular, static properties of the defect (*i.e.* reorientation barriers, EPR parameters, CTLs) are in excellent agreement with those of PV obtained with calculations performed using the method employed throughout this thesis. A possible perspective regarding NV is to verify whether the stability of the complex (*i.e.* binding energy, defect diffusion) is impacted by the off-center position of the impurity, with respect to other *E*-centers.

5.3 Summary: comparison between spectroscopic fingerprints of N_{Si} and NV

As established in Section 5.1, some spectroscopic signals have been assigned to both N_{Si} and NV, even though they have different atomic structure. It is therefore crucial to characterise properly the ground state properties and corresponding spectroscopic fingerprints of each of these defects in order to gain a better understanding of their impact in N-doped Si, which in turn is essential to obtain a better grasp of processes and reactions occurring in semiconductor devices at the microscopic scale. A summary of the findings presented in this thesis through *ab initio* calculations of EPR parameters and deep levels for N_{Si} and NV is presented in Tables 5.7 and 5.8.

Both defects share an important component in their structure, *i.e.* the presence of a N impurity in a substitutional site, therefore similarities in their behaviours is expected. Nonetheless the presence of a Si vacancy next to the impurity in NV alter greatly its spectroscopic signature, compared to N_{Si}, as is evidenced in Tables 5.7 and 5.8. In the case of the hfi structure, a similar behaviour is displayed by the Si atom involved in the distortion in both defects. Both $^{29}Si_1$ and $^{29}Si_{\langle 111\rangle}$ carry the largest fraction of the electron density, which highlights the importance of the Si dangling bonds in defect properties. However, the contributions to the hfi structure

Tab. 5.7: Comparison of EPR parameters for N_{Si} and NV, as calculated in this study. For the hyperfine $\overleftrightarrow{A}$ tensor, the defects exhibit different behaviours. In particular, N_{Si} has a strong contribution for one Si atom only, along the $\langle 111 \rangle$ distortion (($^{29}Si_{\langle 111 \rangle}$)), whereas NV features important contribution for the three vacancy closest Si neighbours ($^{29}Si_i$), two of which ($^{29}Si_2$ and $^{29}Si_3$) are equivalent. In both defects the contribution on the N atom (^{14}N) is also reported for comparison.

	$\overleftrightarrow{g}$				$\overleftrightarrow{A}$ ($^{29}Si_1/^{29}Si_{\langle 111 \rangle}$) (MHz)				$\overleftrightarrow{A}$ ($^{29}Si_{2,3}$) (MHz)				$\overleftrightarrow{A}$ (^{14}N) (MHz)			
Ref.	$\mathbf{g_1}$	$\mathbf{g_2}$	$\mathbf{g_3}$	$\mathbf{g_{iso}}$	$\mathbf{A_1}$	$\mathbf{A_2}$	$\mathbf{A_3}$	$\mathbf{A_{iso}}$	$\mathbf{A_1}$	$\mathbf{A_2}$	$\mathbf{A_3}$	$\mathbf{A_{iso}}$	$\mathbf{A_1}$	$\mathbf{A_2}$	$\mathbf{A_3}$	$\mathbf{A_{iso}}$
N_{Si}	2.0020	2.0089	2.0078	2.0062	–380.4	–205.9	–205.9	–264.1	N/A	N/A	N/A	N/A	37.5	29.6	29.6	32.2
NV	1.9996	2.0101	2.0069	2.0055	–466.3	–316.0	–315.8	–366.0	–67.0	–58.6	–57.0	–60.9	0.87	0.33	0.27	0.49

Tab. 5.8: Comparison of Charge Transition Levels (CTLs) for N_{Si} and NV, as calculated in this study. Thermodynamic CTLs were calculated within the combined DFT and GW approach (N_{Si}-PBE+GW, NV-PBE+GW) for both defects. All levels are given from the conduction band minimum in eV.

Reference	$\epsilon(+/0)$	$\epsilon(0/-)$
N_{Si}-PBE+GW	0.83	0.55
NV-PBE+GW	0.75	0.38

on the impurity and other relevant Si atoms show great disparity. In substitutional nitrogen, the impurity still retains some density while it is spread to two other Si dangling bonds in NV. This result is due to the nature of the distortion which is different in each case. The **Jahn-Teller** effect observed in NV leads to a C_s defect structure whereas for N_{Si} the **pseudo Jahn-Teller** effect distorts the high symmetry arrangement to a C_{3v} configuration. This difference is translated into the spin density of each defect, leading to the noted disparity. The $\overleftrightarrow{g}$-tensor as well exhibits striking divergence, notably in its symmetry. The lower symmetry of the *E*-center leads to a deviation of the perfect axial symmetry reported for the substitutional nitrogen. Finally, the computation of CTLs further helps in discriminating these centers, as both single donor and acceptor levels are deeper within the band gap for N_{Si}.

The above comparative analysis reveals an interesting contrast in behaviour between the two examined defects. N_{Si} exhibits a significantly different behaviour compared to other group-V substitutional impurities, specifically manifesting deep trap behaviour rather than the shallow defect behavior observed in other impurities. On the other hand, in the case of NV, the properties, especially the electronic structure of the defect, arise from the Si dangling bonds surrounding the vacancy, rather than from the impurity itself. This results in a behaviour closely resembling that of other group-V impurity-vacancy complexes.

This thesis establishes clear distinctions in the spectroscopic signatures between two N-related centers, providing valuable guidance for identifying these defects in future experiments on N-doped Si. Linking the spectroscopic properties of defects with their real atomic structures is a challenging task. To achieve this, DFT calculations were employed to characterise symmetry-breaking mechanisms and electronic structures of N-related defects. Additionally, more refined methods based on many-body perturbation theory and linear responses were utilized to compute spectroscopic properties. This approach demonstrates the feasibility of accurately establishing a link between the spectroscopic properties of defects and their real atomic structures, particularly in the complex case of N-related defects in Si.

Bibliography

[1] F. Rougieux, N. E. Grant, C. Barugkin, D. Macdonald, and J. D. Murphy. Influence of annealing and bulk hydrogenation on lifetime-limiting defects in nitrogen-doped floating zone silicon. *IEEE Journal of Photovoltaics*, 5(2):495–498, 2014.

[2] N. E. Grant, V. P. Markevich, J. Mullins, A. R. Peaker, F. Rougieux, D. Macdonald, and J. D. Murphy. Permanent annihilation of thermally activated defects which limit the lifetime of float-zone silicon. *Physica Status Solidi (a)*, 213(11):2844–2849, 2016.

[3] N. E. Grant, V. P. Markevich, J. Mullins, A. R. Peaker, F. Rougieux, and D. Macdonald. Thermal activation and deactivation of grown-in defects limiting the lifetime of float-zone silicon. *Physica Status Solidi (RRL)*, 10(6):443–447, 2016.

[4] J. Mullins, V. P. Markevich, M. Vaqueiro-Contreras, N. E. Grant, L. Jensen, J. Jabłoński, J. D. Murphy, M. P. Halsall, and A. R. Peaker. Thermally activated defects in float zone silicon: Effect of nitrogen on the introduction of deep level states. *Journal of Applied Physics*, 124(3):035701, 2018.

[5] D. Hiller, V. P. Markevich, J. A. T. De Guzman, D. König, S. Prucnal, W. Bock, J. Julin, A. R. Peaker, D. Macdonald, N. E. Grant, and J. D. Murphy. Kinetics of bulk lifetime degradation in float-zone silicon: Fast activation and annihilation of grown-in defects and the role of hydrogen versus light. *Physica Status Solidi (a)*, 217(17):2000436, 2020.

[6] J. A. T. De Guzman, V. P. Markevich, D. Hiller, I. D. Hawkins, M. P. Halsall, and A. R. Peaker. Passivation of thermally-induced defects with hydrogen in float-zone silicon. *Journal of Physics D: Applied Physics*, 54(27):275105, 2021.

[7] M. Nakamura, S. Murakami, and H. Udono. Origins of the nitrogen-related deep donor center and its preceding species in nitrogen-doped silicon determined by deep-level transient spectroscopy. *Applied Physics Express*, 12(2):021005, 2019.

[8] L. Scheffler, A. Lei, S. Duun, and B. Julsgaard. On the nature of thermally activated defects in n-type FZ silicon grown in nitrogen atmosphere. *AIP Advances*, 12(3):035151, 2022.

[9] L. Scheffler, A. Lei, S. Duun, and B. Julsgaard. Comparison of the properties of defect states in nitrogen-containing n-and p-type float-zone silicon: A combined deep-level transient spectroscopy and minority-carrier transient spectroscopy study. *Physica Status Solidi (a)*, 220(3):2200633, 2023.

[10] V. V. Voronkov and R. Falster. Nitrogen interaction with vacancies in silicon. *Materials Science and Engineering: B*, 114:130–134, 2004.

[11] V. V. Voronkov and R. J. Falster. Multiplicity of nitrogen species in silicon: The impact on vacancy trapping. In *Gettering and Defect Engineering in Semiconductor Technology XII*, volume 131 of *Solid State Phenomena*, pages 219–224. Trans Tech Publications Ltd, 1 2008.

[12] V. V. Voronkov and R. Falster. Out-diffusion of deep donors in nitrogen-doped silicon and the diffusivity of vacancies. *Journal of Applied Physics*, 112(1):013519, 2012.

[13] K. L. Brower. Deep-level nitrogen centers in laser-annealed ion-implanted silicon. *Physical Review B*, 26(11):6040, 1982.

[14] M. Belli, M. Fanciulli, and D. Batani. Electron spin resonance of substitutional nitrogen in silicon. *Physical Review B*, 89:115207, Mar 2014.

[15] G. Herrero-Saboya. *Defects in silicon: revisiting theoretical frameworks to guide ab initio characterization*. PhD thesis, Université Toulouse 3 Paul Sabatier, 2020.

[16] G. Herrero-Saboya, L. Martin-Samos, A. Jay, A. Hémeryck, and N. Richard. A comprehensive theoretical picture of E centers in silicon: From optical properties to vacancy-mediated dopant diffusion. *Journal of Applied Physics*, 127(8), 2020.

[17] J. P. Goss, I. Hahn, R. Jones, P. R. Briddon, and S. Öberg. Vibrational modes and electronic properties of nitrogen defects in silicon. *Physical Review B*, 67(4):045206, 2003.

[18] G. D. Watkins and J. W. Corbett. Defects in irradiated silicon: Electron paramagnetic resonance and electron-nuclear double resonance of the si-E center. *Physical Review*, 134(5A):A1359, 1964.

[19] E. L. Elkin and G. D. Watkins. Defects in irradiated silicon: Electron paramagnetic resonance and electron-nuclear double resonance of the arsenic- and antimony-vacancy pairs. *Physical Review*, 174:881–897, Oct 1968.

[20] G. D. Watkins. Understanding the Jahn–Teller distortions for the divacancy and the vacancy–group-V-atom pair in silicon. *Physica B: Condensed Matter*, 376:50–53, 2006.

[21] G. Herrero-Saboya, L. Martin-Samos, N. Richard, and A. Hémeryck. Common defects in diamond lattices as instances of the general $T\otimes(e + t_2)$ Jahn-Teller effect. *Physical Review Materials*, 6(3):034601, 2022.

[22] S. Öğüt and J. R. Chelikowsky. Charge state dependent Jahn-Teller distortions of the E-center defect in crystalline Si. *Physical Review Letters*, 91(23):235503, 2003.

[23] G. Pfanner, C. Freysoldt, J. Neugebauer, and U. Gerstmann. Ab initio EPR parameters for dangling-bond defect complexes in silicon: Effect of Jahn-Teller distortion. *Physical Review B*, 85:195202, May 2012.

[24] K. Szász, T. Hornos, M. Marsman, and A. Gali. Hyperfine coupling of point defects in semiconductors by hybrid density functional calculations: The role of core spin polarization. *Physical Review B*, 88(7):075202, 2013.

[25] N. Fuma, K. Tashiro, K. Kakumoto, and Y. Takano. Diffused nitrogen-related deep level in n-type silicon. *Japanese Journal of Applied Physics*, 35(4R):1993, 1996.

[26] A. N. Larsen, A. Mesli, K. B. Nielsen, H. K. Nielsen, L. Dobaczewski, J. Adey, R. Jones, D. W. Palmer, P. R. Briddon, and S. Öberg. E center in silicon has a donor level in the band gap. *Physical Review Letters*, 97(10):106402, 2006.

[27] A. Platonenko, F. S. Gentile, F. Pascale, A. M. Ferrari, M. D'amore, and R. Dovesi. Nitrogen substitutional defects in silicon. a quantum mechanical investigation of the structural, electronic and vibrational properties. *Physical Chemistry Chemical Physics*, 21(37):20939–20950, 2019.

Conclusions and perspectives

This thesis aimed to characterise defects in silicon for semiconductor applications through symmetry considerations and *ab initio* calculations. In particular, comprehensive models for the ground state properties of two N-related defects were provided. Through these models, the fundamental properties of these defects were elucidated. Moreover, a direct comparison with experiments was established by estimating spectroscopic parameters.

The findings of this study have shed light on the intricate nature of nitrogen-related defects within the silicon lattice and their consequential effects on material properties. Through the integration of *ab initio* calculations based on Density Functional Theory, a global picture of defect structure and properties has been built and a deeper understanding of defect characteristics, symmetries, and interactions achieved. Moreover, by including more advanced methods based on linear response functions and perturbation theory applied to DFT, accurate spectroscopic properties have been computed, enabling direct comparisons with experimental data. Finally, the identification and exploration of Jahn-Teller effects have provided valuable insights into the spontaneous symmetry breaking mechanism of defect ground states, allowing for a more rigorous identification of the ground state structure, rather than depending solely on the level of accuracy of the simulation method.

In particular, by performing a systematic investigation of the symmetry-breaking mechanisms in two nitrogen-related defects, substitutional nitrogen (N_{Si}) and nitrogen-vacancy pair (NV), the fundamental properties of different possible configurations have been characterised, including the electronic structure and relative position of their single-particle defect states within the band gap. Models for their potential energy surfaces have been established, by performing an extensive search of the minimum energy path between equivalent configurations. For N_{Si}, it was found that such a transition path forces the off-center nitrogen center to pass through the on-center configuration that is estimated to be a shallow metastable minimum. In the case of NV, analogous to the *E*-center, the so-called Mexican hat shaped surface has been reproduced, finding three equivalent pairing ground states, separated by three degenerate resonant saddle points. A distinctive feature of NV with respect to other *E*-centers has been pinpointed in the position of the impurity within the defect structure. The nitrogen has been found in an off-center position, similar to what was observed in N_{Si}, whereas models developed

in previous studies for other group-V-impurity-vacancy complexes have located the impurity in an on-center position. This singularity is consistent with the behaviour observed for the simple substitutional impurity, and may account for the difficulty in identifying the NV complex through experimental means.

The computation of EPR parameters for the ground state configurations has been performed and is in excellent agreement with the SL5 EPR signature for N_{Si}. The energy barrier computed for the reorientation mechanism between equivalent off-center structures has been characterised and is in fair agreement with EPR stress measurements, validating the proposed model for the defect potential energy surface. Additionally, estimates are provided that further support a large hyperfine splitting value for the on-center configuration, which contradicts measurements displaying a splitting comparable to the off-center previously associated with this structure. Given that no prior EPR signal was associated with NV, the computed parameters have been evaluated in relation to patterns and trends discerned from earlier calculations and measurements involving other group-V-impurity-vacancy complexes. Consequently, these values align with existing data and can guide experimentalists in future endeavours. Finally, the calculation of thermodynamic Charge Transition Levels for both centers has resulted in a set of deep levels within the band gap. The reported values have therefore allowed to identify incorrect assignments between DLTS activation energies and the electrical activity of the systems, and can guide their identification in future works.

While the present thesis has provided meaningful and unprecedented results concerning the spectroscopic properties of N-related defects in silicon, allowing a better understanding and characterisation of these systems, it is essential to acknowledge the challenges encountered, particularly in terms of constrained computational resources and inherent limitations associated with DFT calculations. As shown in Chapter 2, the careful choice of calculation parameters is essential to obtain accurate results. Current computational resources, though consequent, still are a limiting factor in the convergence of some key values, such as the g-tensor. More importantly however, lies in the approximations done within the DFT framework, in particular regarding the choice of the exchange-correlation functional. The PBE functional, used throughout this work, produces reasonably accurate results in good agreement with experimental EPR measurements for some systems (*e.g.* E-center, N_{Si}). However, inherent inaccuracies in DFT, which tends to delocalise the spin density too much, leads to some failure in correctly describing the electronic structure, and therefore other fundamental physical characteristics such as atomic distortions. This effect can be particularly important for paramagnetic systems for which the potentially high localisation of the electron spin leads to inaccuracies in the description of correlation and exchange interactions. To resolve this matter, a higher level of theory is therefore necessary, such as many-body perturbation theory calculations through the GW approximation.

In conclusion, this thesis has contributed to the ongoing advancements in semiconductor technology by providing a comprehensive theoretical characterisation of defects in silicon-based materials, elucidating their characteristics, behaviours and impacts, and laying the groundwork for future investigations in the field. As semiconductor technology continues to evolve and drive progress in various areas, the insights and findings derived from this study hold promise for guiding future developments, ensuring the continued enhancement and optimisation of semi-

conductor devices and materials for the continued evolution of technology.

As such, a natural extension of this work consists in furthering the analysis of the NV complex. In particular, by conducting a thorough exploration of the potential energy surface, elucidating the differences introduced by the nitrogen displacement on the properties of the defect with respect to other E-centers, researchers can gain a deeper understanding and potentially uncover novel applications. Other perspectives include applying the methodology employed in the present thesis to characterise other defects. In particular, some EPR spectra have been recorded together with that of the SL5 spectrum, namely the SL6 and SL7 spectra, for which no clear assignment has been made. An interesting pursuit could involve the theoretical characterisation of N-related defects in Si by unraveling the defect structure responsible for these signals, that could lead to advancements in our understanding of silicon-based materials and inform future material design. Finally, the characterisation of defect ground states based on symmetry considerations, rather than numerical results, should be adopted more consistently in order to obtain a full picture of defect properties and impact on material characteristics. This approach, coupled with a sufficiently accurate level of theory, would allow to solve long standing controversies in the community regarding defect ground states, as is the case of the silicon divacancy, where the determination of ground states based on symmetry considerations provides a more comprehensive and conclusive understanding of defect properties. The detailed understanding of defects and their behaviors in silicon-based materials could offer valuable insights into the material's electronic and spin properties. The intricate knowledge gained from the thesis on defects, such as the NV complex, provides a foundation for exploring the spin-related properties of silicon at high temperatures. Insights into defect behaviours and their impact on material characteristics might inform the development of materials tailored for specific quantum computing applications. For instance, understanding how defects influence spin states and electronic properties at elevated temperatures is crucial for the design and optimization of spin-based quantum bits (qubits) in unconventional quantum computing architectures.

RÉPUBLIQUE FRANÇAISE
Liberté
Égalité
Fraternité

Université de Toulouse

Titre : Caractérisation ab initio des propriétés spectroscopiques des défauts dans le silicium

Mots clés : Théorie de la Fonctionnelle de la Densité, Silicium, Résonance Paramagnétique Electronique, Défauts ponctuels

Résumé : Le silicium a joué un rôle fondamental dans la technologie moderne des semi-conducteurs au cours des sept dernières décennies. Cependant, l'optimisation des dispositifs basés sur le silicium dépend d'une compréhension approfondie des défauts qui peuvent être introduits dans sa structure, ce qui a un impact significatif sur les performances et la fiabilité de ces dispositifs. Bien que des recherches approfondies aient été menées sur les défauts ponctuels du silicium, certains aspects demeurent encore incompris ou non résolus. Ainsi, la caractérisation des défauts dans le silicium est cruciale pour faire progresser la physique des semi-conducteurs, garantir la fiabilité des dispositifs et stimuler l'innovation dans les applications électroniques. Plusieurs techniques de caractérisation ont été développées pour élucider les propriétés spécifiques des défauts. Notamment, la spectroscopie des niveaux profonds, qui fournit des informations sur le comportement électrique des défauts, comme le nombre et la nature des niveaux profonds au sein de l'échantillon, et la spectroscopie de Résonance Paramagnétique Électronique (RPE), qui offre des informations sur les structures atomiques et électroniques du défaut et de son environnement, sont des outils précieux pour identifier les défauts et évaluer leur impact sur les propriétés du matériau. Cependant, l'identification de structures de défaut spécifiques par des moyens spectroscopiques est souvent complexe et nécessite la combinaison de plusieurs techniques pour obtenir une image complète du défaut. Ces vingt dernières années, les efforts d'identification ont été de plus en plus soutenus par des méthodes théoriques, telles que les calculs ab initio basés sur la Théorie de la Fonctionnelle de la Densité (DFT), qui jouent un rôle complémentaire et crucial pour améliorer la compréhension de la physique du défaut.
Cette thèse présente des modèles de structures à l'état fondamental pour plusieurs défauts dans le silicium. Contrairement à de nombreuses simulations atomistiques antérieures qui déterminent l'état fondamental à partir de résultats numériques, cette étude définit la structure à travers des considérations de symétrie, en s'appuyant sur des approches d'orbitales moléculaires et de théorie des groupes. Cette approche renforce la fiabilité du modèle et n'est pas limitée par la précision numérique des calculs DFT. Les propriétés physiques fondamentales du défaut, telles que son paysage énergétique ou sa structure électronique, sont alors établies par des calculs DFT. De plus, en incluant des approches plus raffinées basées sur la théorie des perturbations et les corrections à plusieurs corps, les paramètres RPE et les niveaux de transition de charge thermodynamiques sont calculés pour permettre une comparaison directe avec les expériences de spectroscopie. La fiabilité et la précision de cette méthodologie sont d'abord validées sur un système bien connu, le complexe phosphore-vacance, également connu sous le nom de centre E du silicium, montrant une excellente concordance avec les expériences et les méthodes théoriques précédentes pour les paramètres RPE. Ensuite, cette méthode est appliquée à divers défauts liés à l'azote dans le silicium, qui sont moins bien compris. Les paramètres spectroscopiques calculés permettent ainsi d'établir une correspondance sans équivoque entre les signaux expérimentaux disponibles et les structures de défaut, tout en fournissant des valeurs de référence pour guider les expérimentateurs dans les cas où les données ne sont pas disponibles.

Title: Ab initio characterisation of spectroscopic properties of defects in silicon

Key words: Density Functional Theory, Silicon, Electron Paramagnetic Resonance, Point defects

Abstract: Silicon has been a cornerstone of modern semiconductor technology for the last seven decades. However, the optimisation of silicon-based devices hinges on a deep understanding of the defects that can be introduced into its structure, which can significantly influence device performance and reliability. Although extensive research has been conducted on point defects in silicon, certain aspects are still not fully understood or have not yet been resolved. Therefore, characterising defects in silicon is a critical imperative for advancing semiconductor physics, ensuring device reliability, and driving innovation in electronic applications. Multiple characterisation techniques have been developed to unravel defect specific properties. In particular, Deep Level Transient Spectroscopy which allows obtaining information on the electrical behaviour of defects and more specifically the number and nature of deep levels within the gap of the sample containing them, and Electron Paramagnetic Resonance spectroscopy (EPR) which provides information on the atomic and electronic structures of the defect and its environment are invaluable in identifying defects and evaluating their impact on the properties of the material. Yet, identifying specific defect structures through spectroscopic means is often non-trivial and requires to combine several techniques to obtain a complete picture of the system. In the last two decades, the identification effort has been more and more supported by theoretical methods, such as ab initio calculations based on Density Functional Theory (DFT), that play a complementary and crucial role in improving the understanding of the physics of the defect.
This thesis presents models of ground state structures for several defects in silicon. Unlike many prior atomistic simulations that determine the ground state from numerical results, this study defines the structure through symmetry considerations, i.e. grounded in molecular orbital approaches and group theory. This approach enhances the reliability of the model and is not limited by the numerical accuracy of DFT calculations. The fundamental physical properties of the defect, such as its energy landscape or electronic structure, are established by DFT calculations. Moreover, by including more refined approaches, based on perturbation theory and many-body corrections, EPR parameters and thermodynamic charge transition levels are calculated in order to provide direct comparison with spectroscopy experiments. The reliability and accuracy of this methodology is first validated on a well-known system, the phosphorus-vacancy complex, the so-called silicon E -center and very good agreement is obtained with experiments and previous theoretical methods for EPR parameters. This method is then applied to various nitrogen-related defects in silicon, which are not as well understood. The computed spectroscopic parameters thus allow obtaining an unequivocal correspondence between available experimental signals and defect structures, as well as providing reference values to guide experimenters in cases when data are not available.